BOSTON UNIVERSITY

GRADUATE SCHOOL OF ARTS AND SCIENCES

Dissertation

STATISTICAL APPROACHES TO UNDERSTANDING PHYSIOLOGICAL FLUCTUATIONS

by

KUN HU

B.S., Zhongshan University, 1995
M.A., University of Rhode Island, 1999

Submitted in partial fulfillment of the

requirements for the degree of

Doctor of Philosophy

2004

Approved by

First Reader

H. Eugene Stanley, Ph.D.
University Professor,
Professor of Physics

Second Reader

Claudio Rebbi, Ph.D.
Professor of Physics

Contents

List of Tables

List of Figures

Part I

Introduction

Part II

Effect of Nonstationary on Scaling Behavior

Chapter 1

Effect of Trends on Detrended Fluctuation Analysis

1.1 Overview

Detrended fluctuation analysis (DFA) is a scaling analysis method used to estimate long-range power-law correlation exponents in noisy signals. Many noisy signals in real systems display trends, so that the scaling results obtained from the DFA method become difficult to analyze. We systematically study the effects of three types of trends — linear, periodic, and power-law trends, and offer examples where these trends are likely to occur in real data. We compare the difference between the scaling results for artificially generated correlated noise and correlated noise with a trend, and study how trends lead to the appearance of crossovers in the scaling behavior. We find that crossovers result from the competition between the scaling of the noise and the "apparent" scaling of the trend. We study how the characteristics of these crossovers depend on (i) the slope of the linear trend; (ii) the amplitude and period of the periodic trend; (iii) the amplitude and power of the power-law trend and (iv) the length as well as the correlation properties of the noise. Surprisingly, we

find that the crossovers in the scaling of noisy signals with trends also follow scaling laws — i.e. long-range power-law dependence of the position of the crossover on the parameters of the trends. We show that the DFA result of noise with a trend can be exactly determined by the superposition of the separate results of the DFA on the noise and on the trend, assuming that the noise and the trend are not correlated. If this superposition rule is not followed, this is an indication that the noise and the superimposed trend are not independent, so that removing the trend could lead to changes in the correlation properties of the noise. In addition, we show how to use DFA appropriately to minimize the effects of trends, and how to recognize if a crossover indicates indeed a transition from one type to a different type of underlying correlation, or the crossover is due to a trend without any transition in the dynamical properties of the noise.

1.2 Introduction to this chapter

Many physical and biological systems exhibit complex behavior characterized by long-range power-law correlations. Traditional approaches such as the power-spectrum and correlation analysis are not suited to accurately quantify long-range correlations in non-stationary signals — e.g. signals exhibiting fluctuations along polynomial trends. Detrended fluctuation analysis (DFA)[4–7] is a scaling analysis method providing a simple quantitative parameter — the scaling exponent α — to represent the correlation properties of a signal. The advantages of DFA over many methods are that it permits the detection of long-range correlations embedded in seemingly non-stationary time series, and also avoids the spurious detection of apparent long-range correlations that are artifact of non-stationarity. In the past few years, more than 100 publications have utilized the DFA as method of correlation analysis, and have uncovered long-range power-law correlations in many research fields such as cardiac dynamics[8–12, **?**–12, 14–25, **?**–25], bioinformatics[4, 5, 27–37], economics[38–

50], meteorology[51–53], material science[54], ethology[55] etc. Furthermore, the DFA method may help identify different states of the same system according to its different scaling behaviors — e.g. the scaling exponent α for heart inter-beat intervals is different for healthy and sick individuals[17, 19, 20, 56].

The correct interpretation of the scaling results obtained by the DFA method is crucial for understanding the intrinsic dynamics of the systems under study. In fact, for all systems where the DFA method was applied, there are many issues that remain unexplained. One of the common challenges is that the correlation exponent is not always a constant (independent of scale) and crossovers often exist — i.e. change of the scaling exponent α for different range of scales[19, ?, ?]. A crossover usually can arise from a change in the correlation properties of the signal at different time or space scales, or can often arise from trends in the data. In this chapter, we systematically study how different types of trends affect the apparent scaling behavior of long-range correlated signals. The existence of trends in times series generated by physical or biological systems is so common that it is almost unavoidable. For example, the number of particles emitted by a radiation source in an unit time has a trend of decreasing because the source becomes weaker[57, 58]; the density of air due to gravity has a trend at different altitude [59]; the air temperature in different geographic locations and the water flow of rivers have a periodic trend due to seasonal changes[52, 53, 60–62]; the occurrence rate of earthquakes in certain area has trend in different time period[63]. An immediate problem facing researchers applying scaling analysis to time series is whether trends in data arise from external conditions, having little to do with the intrinsic dynamics of the system generating noisy fluctuating data. In this case, a possible approach is to first recognize and filter out the trends before we attempt to quantify correlations in the noise. Alternatively, trends may arise from the intrinsic dynamics of the system, rather than being an epiphenomenon of external conditions, and thus may be correlated with the noisy fluctuations generated by the system. In this case, careful considerations should be

given if trends should be filtered out when estimating correlations in the noise, since such "intrinsic" trends may be related to the local properties of the noisy fluctuations.

Here we study the origin and the properties of crossovers in the scaling behavior of noisy signals, by applying the DFA method first on correlated noise and then on noise with trends, and comparing the difference in the scaling results. To this end, we generate artificial time series — anticorrelated, white and correlated noise with standard deviation equal to one — using the modified Fourier filtering method introduced by Makse *et al.* [67]. We consider the case when the trend is independent of the local properties of the noise (external trend). We find that the scaling behavior of noise with a trend is a superposition of the scaling of the noise and the apparent scaling of the trend, and we derive analytical relations based on the DFA, which we call "superposition rule". We show how this "superposition rule" can be used to determine if the trends are independent of the noisy fluctuation in real data, and if filtering these trends out will no affect the scaling properties of the data.

The outline of this chapter is as follows. In Sec. 1.3, we consider the effect of a linear trend and we present an analytic derivation of the apparent scaling behavior of a linear trend in Appendix .4. In Sec. 1.4, we study a periodic trend, and in Sec. 1.5 the effect of power-law trend. We systematically study all resulting crossovers, their conditions of existence and their typical characteristics associated with the different types of trends. In addition, we also show how to use DFA appropriately to minimize or even eliminate the effects of those trends in cases that trends are not choices of the study, that is, trends do not reflect the dynamics of the system but are caused by some "irrelevant" background. Finally, Sec. 1.6 contains a summary.

1.3 Noise with linear trends

First we consider the simplest case: correlated noise with a linear trend. A linear trend

$$u(i) = A_{\rm L} i \tag{1.1}$$

is characterized by only one variable — the slope of the trend, $A_{\rm L}$. For convenience, we denote the rms fluctuation function for noise without trends by $F_\eta(n)$, linear trends by $F_{\rm L}(n)$, and noise with a linear trend by $F_{\eta{\rm L}}(n)$.

1.3.1 DFA-1 on noise with a linear trend

Using the algorithm of Makse [67], we generate correlated noise with standard deviation one, with a given correlation property characterized by a given scaling exponent α. We apply DFA-1 to quantify the correlation properties of the noise and find that only in certain good fit region the rms fluctuation function $F_\eta(n)$ can be approximated by a power-law function

$$F_\eta(n) = b_0 n^\alpha \tag{1.2}$$

where b_0 is a parameter independent of the scale n. We find that the good fit region depends on the correlation exponent α [see Appendix .2]. We also derive analytically the rms fluctuation function for linear trend only for DFA-1 and find that [see Appendix .4]

$$F_{\rm L}(n) = k_0 A_{\rm L} n^{\alpha_L} \tag{1.3}$$

where k_0 is a constant independent of the length of trend N_{max}, of the box size n and of the slope of the trend $A_{\rm L}$. We obtain $\alpha_L = 2$.

Next we apply the DFA-1 method to the superposition of a linear trend with correlated noise and we compare the rms fluctuation function $F_{\eta{\rm L}}(n)$ with $F_\eta(n)$ [see Fig.1.1]. We observe a crossover in $F_{\eta{\rm L}}(n)$ at scale $n = n_\times$. For $n < n_\times$, the behavior

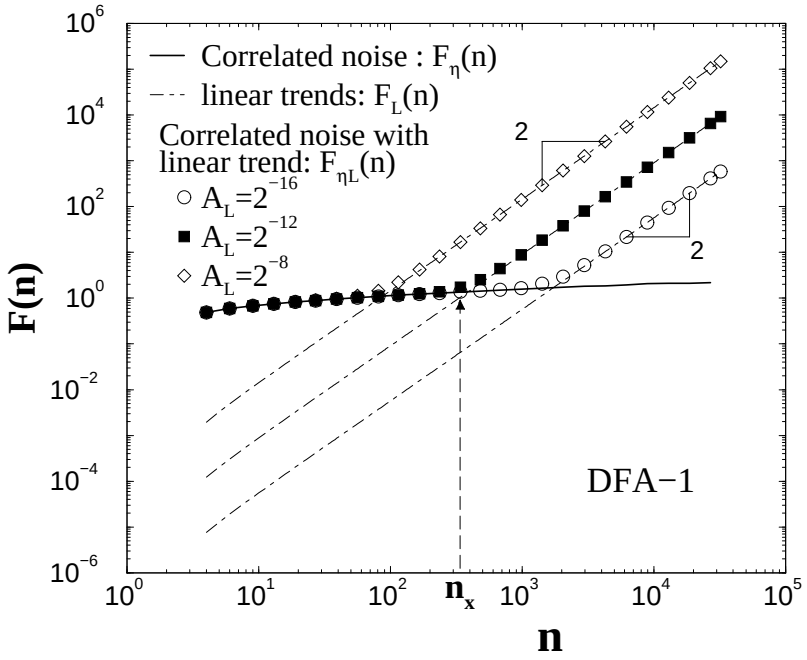

Fig. 1.1. We observe crossover behavior of the root mean square fluctuation function $F_{\eta \mathrm{L}}(n)$ for noise (of length $N_{max} = 2^{17}$ and correlation exponent $\alpha = 0.1$) with superposed linear trends of slope $A_{\mathrm{L}} = 2^{-16}, 2^{-12}, 2^{-8}$. For comparison, we show $F_{\eta}(n)$ for the noise (thick solid line) and $F_{\mathrm{L}}(n)$ for the linear trends (dot-dashed line) (Eq.(1.3)). The results show that a crossover at a scale $n_{\times}$ for $F_{\eta \mathrm{L}}(n)$. For $n < n_{\times}$, the noise dominates and $F_{\eta \mathrm{L}}(n) \approx F_{\eta}(n)$. For $n > n_{\times}$, the linear trend dominates and $F_{\eta \mathrm{L}}(n) \approx F_{\mathrm{L}}(n)$. Note that the crossover scale $n_{\times}$ increases when the slope A_{L} of the trend decreases.

of $F_{\eta \mathrm{L}}(n)$ is very close to the behavior of $F_{\eta}(n)$, while for $n > n_{\times}$, the behavior of $F_{\eta \mathrm{L}}(n)$ is very close to the behavior of $F_{\mathrm{L}}(n)$. A similar crossover behavior is also observed in the scaling of the well-studied biased random walk [65, 66]. It is known that the crossover in the biased random walk is due to the competition of the unbiased random walk and the bias [see Fig.5.3 of [66]]. We illustrate this observation in Fig. 1.2, where the detrended fluctuation functions (Eq. (5)) of the correlated noise, $Y_{\eta}(i)$, and of the noise with a linear trend, $Y_{\eta \mathrm{L}}(i)$ are shown. For the box size $n < n_{\times}$ as shown in Fig. 1.2(a) and (b), $Y_{\eta \mathrm{L}}(i) \approx Y_{\eta}(i)$. For $n > n_{\times}$ as shown in Fig. 1.2(c)

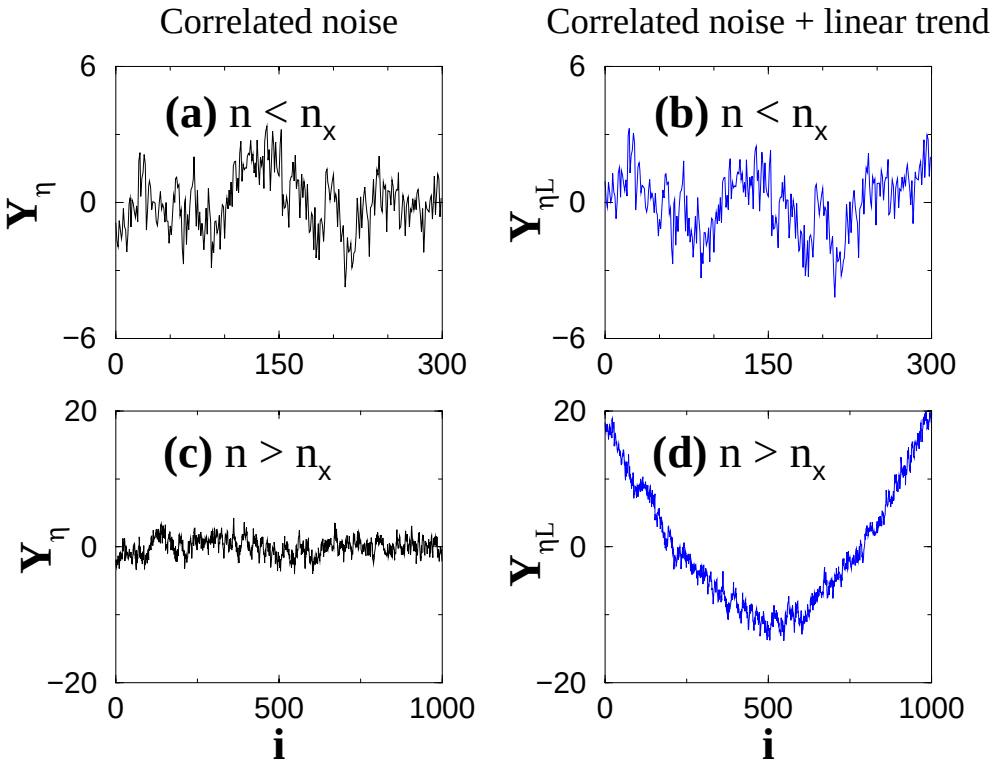

Fig. 1.2. (a) and (c) are Y_η for noise with $\alpha = 0.1$; (b) and (d) are $Y_{\eta\mathrm{L}}$ for the same noise with a linear trend with slope $A_\mathrm{L} = 2^{-12}$ (the crossover scale $n_\times = 320$ see Fig. 1.1). (a) (b) for scales $n < n_\times$ the effect of the trend is not pronounced and $Y_\eta \approx Y_{\eta\mathrm{L}}$ (i.e. $Y_\eta \gg Y_\mathrm{L}$); (c)(d) for scales $n > n_\times$, the linear trend is dominant and $Y_\eta \ll Y_{\eta\mathrm{L}}$.

and (d), $Y_{\eta\mathrm{L}}(i)$ has distinguishable quadratic background significantly different from $Y_\eta(i)$. This quadratic background is due to the integration of the linear trend within the DFA procedure and represents the detrended fluctuation function Y_L of the linear trend. These relations between the detrended fluctuation functions $Y(i)$ at different time scales n explain the crossover in the scaling behavior of $F_{\eta\mathrm{L}}(n)$: from very close to $F_\eta(n)$ to very close to $F_\mathrm{L}(n)$ (observed in Fig.1.1).

The experimental results presented in Figs.1.1 and 1.2 suggest that the rms fluctuation function for a signal which is a superposition of a correlated noise and a

linear trend can be expressed as:

$$[F_{\eta \mathrm{L}}(n)]^2 = [F_{\mathrm{L}}(n)]^2 + [F_{\eta}(n)]^2 \tag{1.4}$$

We provide an analytic derivation of this relation in Appendix .3, where we show that Eq.(1.4) holds for the superposition of any two independent signals — in this particular case noise and a linear trend. We call this relation the "superposition rule". This rule helps us understand how the competition between the contribution of the noise and the trend to the rms fluctuation function $F_{\eta \mathrm{L}}(n)$ at different scales n leads to appearance of crossovers [65].

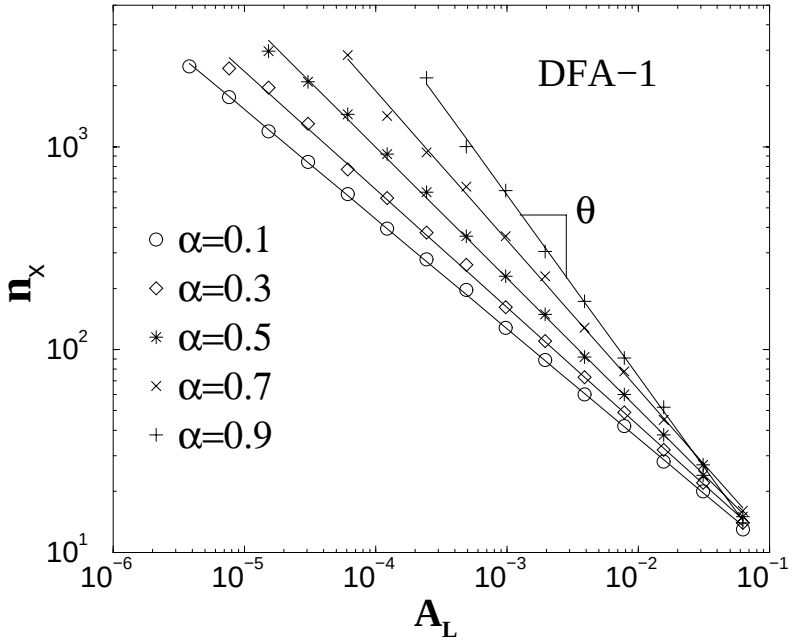

Fig. 1.3. The crossover $n_\times$ of $F_{\eta \mathrm{L}}(n)$ for noise with a linear trend. We determine the crossover scale $n_\times$ based on the difference Δ between $\log F_\eta$ (noise) and $\log F_{\eta \mathrm{L}}$ (noise with a linear trend). The scale for which $\Delta = 0.05$ is the estimated crossover scale $n_\times$. For any given correlation exponent α of the noise, the crossover scale $n_\times$ exhibits a long-range power-law behavior $n_\times \sim (A_{\mathrm{L}})^\theta$, where the crossover exponent θ is a function of α [see Eq.(1.5) and Table 1.1].

Next, we ask how the crossover scale $n_\times$ depends on: (i) the slope of the linear trend A_{L}, (ii) the scaling exponent α of the noise, and (iii) the length of the signal

N_{max}. Surprisingly, we find that for noise with any given correlation exponent α the crossover scale $n_\times$ itself follows a power-law scaling relation over several decades: $n_\times \sim (A_{\rm L})^\theta$ (see Fig. 1.3). We find that in this scaling relation, the crossover exponent θ is negative and its value depends on the correlation exponent α of the noise — the magnitude of θ decreases when α increases. We present the values of the "crossover exponent" θ for different correlation exponents α in Table 1.1.

Table 1.1. The values of θ obtained from our simulations [Fig. 1.3] are in good agreement with the analytical prediction $-1/(2-\alpha)$ [Eq. (1.5)]. Note that $-1/(2-\alpha)$ are not always exactly equal to θ because $F_\eta(n)$ in simulations is not a perfect simple power-law function and the way we determine numerically $n_\times$ is just approximated.

α	θ	$-1/(2-\alpha)$
0.1	-0.54	-0.53
0.3	-0.58	-0.59
0.5	-0.65	-0.67
0.7	-0.74	-0.77
0.9	-0.89	-0.91

To understand how the crossover scale depends on the correlation exponent α of the noise we employ the superposition rule [Eq.(1.4)] and estimate $n_\times$ as the intercept between $F_\eta(n)$ and $F_{\rm L}(n)$. From the Eqs. (1.2) and (1.3), we obtain the following dependence of $n_\times$ on α:

$$n_\times = \left(A_{\rm L}\frac{k_0}{b_0}\right)^{1/(\alpha-\alpha_L)} = \left(A_{\rm L}\frac{k_0}{b_0}\right)^{1/(\alpha-2)} \tag{1.5}$$

This analytical calculation for the crossover exponent $-1/(\alpha_L-\alpha)$ is in a good agreement with the observed values of θ obtained from our simulations [see Fig.1.3 and Table 1.1].

Finally, since the $F_{\rm L}(n)$ does not depend on N_{max} as we show in Eq.(1.3) and in Appendix .4, we find that $n_\times$ does not depend on N_{max}. This is a special case for linear trends and does not always hold for higher order polynomial trends [see Appendix .5].

1.3.2 DFA-2 on noise with a linear trend

Application of the DFA-2 method to noisy signals without any polynomial trends leads to scaling results identical to the scaling obtained from the DFA-1 method, with the exception of some vertical shift to lower values for the rms fluctuation function $F_\eta(n)$ [see Appendix .2]. However, for signals which are a superposition of correlated noise and a linear trend, in contrast to the DFA-1 results presented in Fig. 1.1, $F_{\eta{\rm L}}(n)$ obtained from DFA exhibits no crossovers, and is exactly equal to the rms fluctuation function $F_\eta(n)$ obtained from DFA-2 for correlated noise without trend (see Fig. 1.4). These results indicate that a linear trend has no effect on the scaling obtained from DFA-2. The reason for this is that by design the DFA-2 method filters out linear trends, i.e. $Y_{\rm L}(i) = 0$ (Eq.(5)) and thus $F_{\eta{\rm L}}(n) = F_\eta(n)$ due to the superposition rule (Eq. (1.4)). For the same reason, polynomial trends of order lower than ℓ superimposed on correlated noise will have no effect on the scaling properties of the noise when DFA-ℓ is applied. Therefore, our results confirm that the DFA method is a reliable tool to accurately quantify correlations in noisy signals embedded in polynomial trends. Moreover, the reported scaling and crossover features of $F(n)$ can be used to determine the order of polynomial trends present in the data.

1.4 Noise with sinusoidal trend

In this section, we study the effect of sinusoidal trends on the scaling properties of noisy signals. For a signal which is a superposition of correlated noise and sinusoidal trend, we find that based on the superposition rule (Appendix .3) the DFA rms

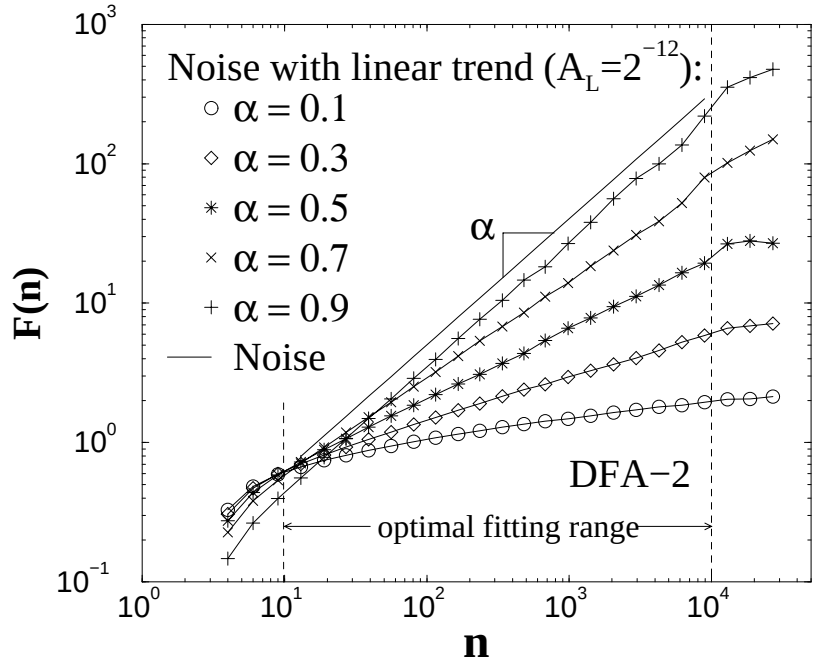

Fig. 1.4. The slope of the linear trend $A_{\rm L} = 2^{-12}$. Lines are for noise and symbols for the noise with the linear trend. $F_{\eta{\rm L}}(n) = F_\eta(n)$ because the integrated linear trend can be perfectly filtered out in DFA-2, thus $Y_{\rm L}(i) = 0$ from Eq.(5). We note, that to estimate accurately the correlation exponents one has to choose an optimal range of scales n, where $F(n)$ is fitted. For details see Appendix .2.

fluctuation function can be expressed as

$$[F_{\eta{\rm S}}(n)]^2 = [F_\eta(n)]^2 + [F_{\rm S}(n)]^2\,, \tag{1.6}$$

where $F_{\eta{\rm S}}(n)$ is the rms fluctuation function of noise with a sinusoidal trend, and $F_{\rm S}(n)$ is for the sinusoidal trend. First we consider the application of DFA-1 to a sinusoidal trend. Next we study the scaling behavior and the features of crossovers in $F_{\eta{\rm S}}(n)$ for the superposition of correlated noise and sinusoidal trend employing the superposition rule [Eq.(1.6)]. At the end of this section, we discuss the results obtained from higher order DFA.

1.4.1 DFA-1 on sinusoidal trend

Given a sinusoidal trend $u(i) = A_{\rm S} \sin(2\pi i/T)$ $(i = 1, ..., N_{max})$, where $A_{\rm S}$ is the amplitude of the signal and T is the period, we find that the rms fluctuation function $F_{\rm S}(n)$ does not depend on the length of the signal N_{max}, and has the same shape for different amplitudes and different periods [Fig. 1.5]. We find a crossover at scale corresponding to the period of the sinusoidal trend

$$n_{2\times} \approx T, \tag{1.7}$$

and does not depend on the amplitude $A_{\rm S}$. We call this crossover $n_{2\times}$ for convenience, as we will see later. For $n < n_{2\times}$, the rms fluctuation $F_{\rm S}(n)$ exhibits an apparent

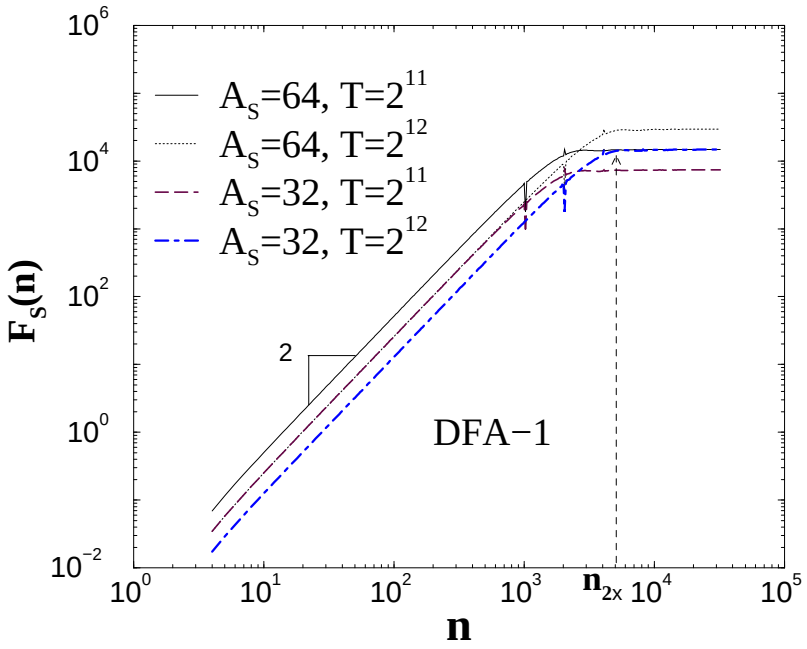

Fig. 1.5. We consider sinusoidal functions of length $N_{max} = 2^{17}$ with different amplitude $A_{\rm S}$ and period T. All curves exhibit a crossover at $n_{2\times} \approx T/2$, with a slope $\alpha_{\rm S} = 2$ for $n < n_{2\times}$, and a flat region for $n > n_{2\times}$. There are some spurious singularities at $n = j\frac{T}{2}$ (j is a positive integer) shown by the spikes.

scaling with the same exponent as $F_{\rm L}(n)$ for the linear trend [see Eq. (1.3)]:

$$F_{\rm S}(n) = k_1 \frac{A_{\rm S}}{T} n^{\alpha_{\rm S}} \tag{1.8}$$

where k_1 is a constant independent of the length N_{max}, of the period T and the amplitude $A_{\rm S}$ of the sinusoidal signal, and of the box size n. As for the linear trend [Eq.(1.3)], we obtain $\alpha_{\rm S} = 2$ because at small scales (box size n) the sinusoidal function is dominated by a linear term. For $n > n_{2\times}$, due to the periodic property of the sinusoidal trend, $F_{\rm S}(n)$ is a constant independent of the scale n:

$$F_{\rm S}(n) = \frac{1}{2\sqrt{2}\pi} A_{\rm S} \cdot T. \tag{1.9}$$

The period T and the amplitude $A_{\rm S}$ also affects the vertical shift of $F_{\rm S}(n)$ in both regions. We note that in Eqs.(1.8) and (1.9), $F_{\rm S}(n)$ is proportional to the amplitude $A_{\rm S}$, a behavior which is also observed for the linear trend [Eq. (1.3)].

1.4.2 DFA-1 on noise with sinusoidal trend

In this section, we study how the sinusoidal trend affects the scaling behavior of noise with different type of correlations. We apply the DFA-1 method to a signal which is a superposition of correlated noise with a sinusoidal trend. We observe that there are typically three crossovers in the rms fluctuation $F_{\eta{\rm S}}(n)$ at characteristic scales denoted by $n_{1\times}$, $n_{2\times}$ and $n_{3\times}$ [Fig. 1.6]. These three crossovers divide $F_{\eta{\rm S}}(n)$ into four regions, as shown in Fig. 1.6(a) (the third crossover cannot be seen in Fig. 1.6(b) because its scale $n_{3\times}$ is greater than the length of the signal). We find that the first and third crossovers at scales $n_{1\times}$ and $n_{3\times}$ respectively [see Fig. 1.6] result from the competition between the effects on $F_{\eta{\rm S}}(n)$ of the sinusoidal signal and the correlated noise. For $n < n_{1\times}$ (region I) and $n > n_{3\times}$ (region IV), we find that the noise has the dominating effect ($F_\eta(n) > F_{\rm S}(n)$), so the behavior of $F_{\eta{\rm S}}(n)$ is very close to the behavior of $F_\eta(n)$ [Eq. (1.6)]. For $n_{1\times} < n < n_{2\times}$ (region II) and $n_{2\times} < n < n_{3\times}$

(region III) the sinusoidal trend dominates ($F_{\rm S}(n) > F_\eta(n)$), thus the behavior of $F_{\eta{\rm S}}(n)$ is close to $F_{\rm S}(n)$ [see Fig. 1.6 and Fig. 1.7].

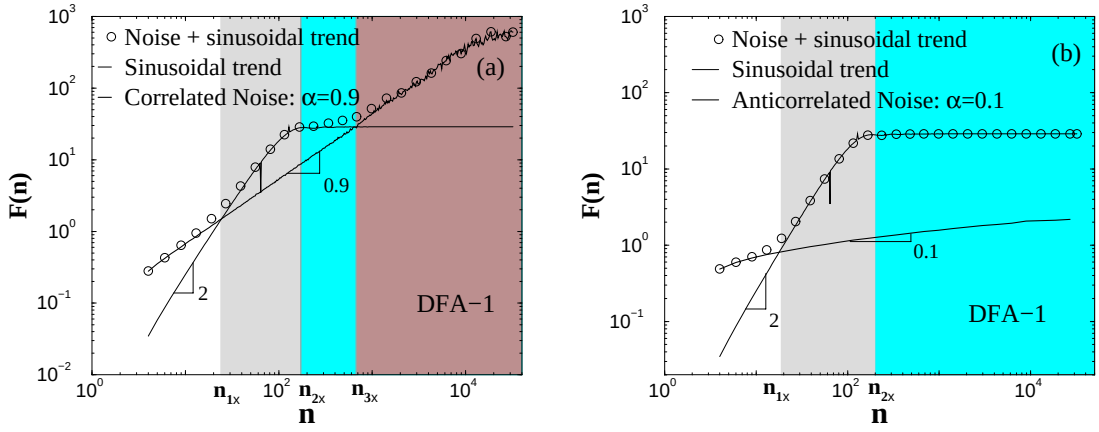

Fig. 1.6. We observe crossover behavior of the root mean square fluctuation function $F_{\eta{\rm S}}(n)$ (circles) for correlated noise with of length $N_{max} = 2^{17}$) with a superposed sinusoidal function characterized by period $T = 128$ and amplitude $A_{\rm S} = 2$. The rms fluctuation function $F_\eta(n)$ for noise (thick line) and $F_{\rm S}(n)$ for the sinusoidal trend (thin line) are shown for comparison. (a) $F_{\eta{\rm S}}(n)$ for correlated noise with $\alpha = 0.9$. (b) $F_{\eta{\rm S}}(n)$ for anticorrelated noise with $\alpha = 0.9$. There are three crossovers in $F_{\eta{\rm S}}(n)$, at scales $n_{1\times}$, $n_{2\times}$ and $n_{3\times}$ (the third crossover can not be seen in (b) because it occurs at scale larger than the length of the signal). For $n < n_{1\times}$ and $n > n_{3\times}$, the noise dominates and $F_{\eta{\rm S}}(n) \approx F_\eta(n)$ while for $n_{1\times} < n < n_{3\times}$, the sinusoidal trend dominates and $F_{\eta{\rm S}}(n) \approx F_{\rm S}(n)$. The crossovers at $n_{1\times}$ and $n_{3\times}$ are due to the competition between the correlated noise and the sinusoidal trend [see Fig. 1.7], while the crossover at $n_{2\times}$ relates only to the period T of the sinusoidal [Eq. (1.7)].

To better understand why there are different regions in the behavior of $F_{\eta{\rm S}}(n)$, we consider the detrended fluctuation function [Eq. (5) and Appendix .3] of the correlated noise $Y_\eta(i)$, and of the noise with sinusoidal trend $Y_{\eta{\rm S}}$. In Fig. 1.7 we compare $Y_\eta(i)$ and $Y_{\eta{\rm S}}(i)$ for anticorrelated and correlated noise in the four different regions. For very small scales $n < n_{1\times}$, the effect of the sinusoidal trend is not pronounced, $Y_{\eta{\rm S}}(i) \approx Y_\eta(i)$, indicating that in this scale region the signal can be considered as noise fluctuating around a constant trend which is filtered out by the DFA-1 procedure [Fig. 1.7(a)(b)]. Note, that the behavior of $Y_{\eta{\rm S}}$ [Fig. 1.7(b)] is

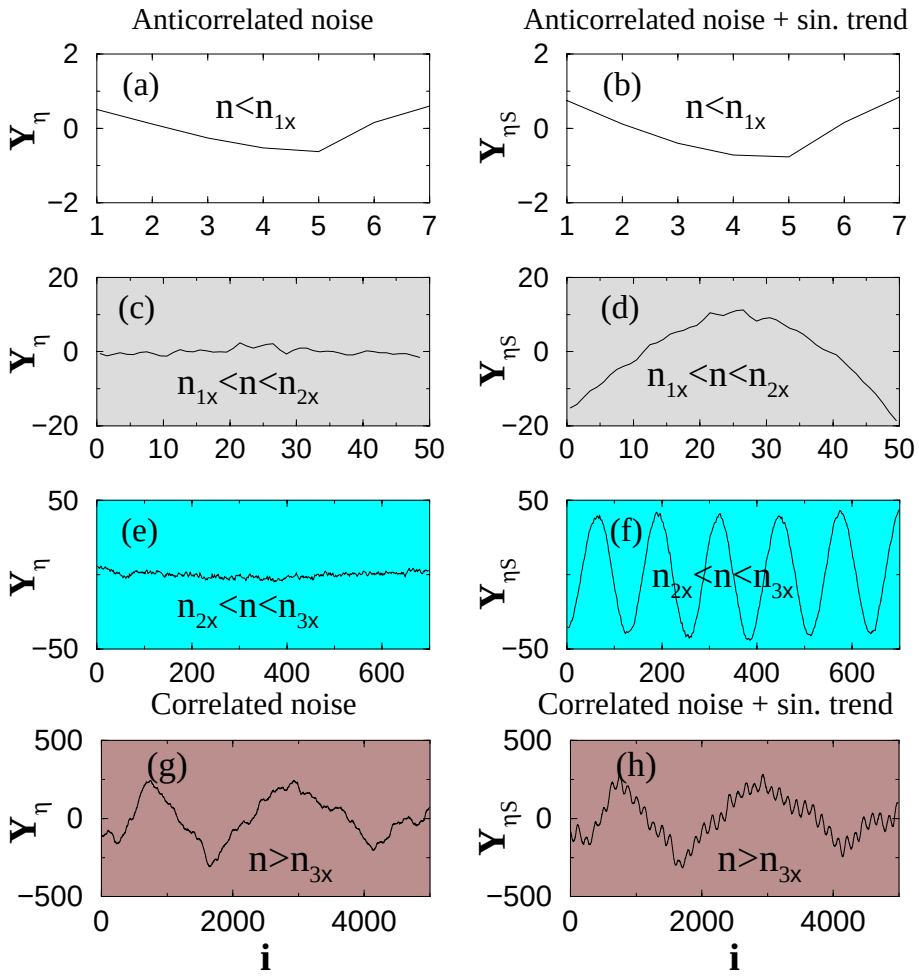

Fig. 1.7. Comparison of the detrended fluctuation function for noise, $Y_\eta(i)$ and noise with sinusoidal trend, $Y_{\eta\mathrm{S}}(i)$ in four regions as shown in Fig. 1.6. The same signals as in Fig. 1.6 are used. Panels (a)-(f) correspond to Fig. 1.6(b) for anticorrelated noise with exponent $\alpha = 0.1$, and panels (g)-(h) correspond to the Fig. 1.6(a) for correlated noise with exponent $\alpha = 0.9$. (a)-(b) For all scales $n < n_{1\times}$, the effect of the trend is not pronounced and $Y_{\eta\mathrm{S}}(i) \approx Y_\eta(i)$ leading to $F_{\eta\mathrm{S}}(n) \approx F_\eta(n)$ (Fig. 1.6(a)). (c)(d) For $n_{2\times} > n > n_{1\times}$, the trend is dominant, $Y_{\eta\mathrm{S}}(i) \gg Y_\eta(i)$ and $F_{\eta\mathrm{S}}(n) \approx F_{\mathrm{S}}(n)$. Since $n_{2\times} \approx T/2$ (Eq. (1.7)), the scale $n < T/2$ and the sinusoidal behavior can be approximated as a linear trend. This explains the quadratic background in $Y_{\eta\mathrm{S}}(i)$ (d) [see Fig. 1.2(c)(d)]. (e)(f) For $n_{2\times} < n < n_{3\times}$ (i.e. $n \gg T/2$), the sinusoidal trend again dominates — $Y_{\eta\mathrm{S}}(i)$ is periodic function with period T. (g)(h) for $n > n_{3\times}$, the effect of the noise is dominant and the scaling of $F_{\eta\mathrm{S}}$ follows the scaling of F_η (Fig. 1.6(a)).

identical to the behavior of $Y_{\eta \mathrm{L}}$ [Fig. 1.2(b)], since both a sinusoidal with a large period T and a linear trend with small slope A_{L} can be well approximated by a constant trend for $n < n_{1\times}$. For small scales $n_{1\times} < n < n_{2\times}$ (region II), we find that there is a dominant quadratic background for $Y_{\eta \mathrm{S}}(i)$ [Fig. 1.7(d)]. This quadratic background is due to the integration procedure in DFA-1, and is represented by the detrended fluctuation function of the sinusoidal trend $Y_{\mathrm{S}}(i)$. It is similar to the quadratic background observed for linear trend $Y_{\eta \mathrm{L}}(i)$ [Fig. 1.2(d)] — i.e. for $n_{1\times} < n < n_{2\times}$ the sinusoidal trend behaves as a linear trend and $Y_{\mathrm{S}}(i) \approx Y_{\mathrm{L}}(i)$. Thus in region II the "linear trend" effect of the sinusoidal is dominant, $Y_{\mathrm{S}} > Y_{\eta}$, which leads to $F_{\eta \mathrm{S}}(n) \approx F_{\mathrm{S}}(n)$. This explains also why $F_{\eta \mathrm{S}}(n)$ for $n < n_{2\times}$ (Fig. 1.6) exhibits crossover behavior similar to the one of $F_{\eta \mathrm{L}}(n)$ observed for noise with a linear trend. For $n_{2\times} < n < n_{3\times}$ (region III) the sinusoidal behavior is strongly pronounced [Fig. 1.7(f)], $Y_{\mathrm{S}}(i) \gg Y_{\eta}(i)$, and $Y_{\eta \mathrm{S}}(i) \approx Y_{\mathrm{S}}(i)$ changes periodically with period equal to the period of the sinusoidal trend T. Since $Y_{\eta \mathrm{S}}(i)$ is bounded between a minimum and a maximum value, $F_{\eta \mathrm{S}}(n)$ cannot increase and exhibits a flat region (Fig. 1.6). At very large scales, $n > n_{3\times}$, the noise effect is again dominant ($Y_{\mathrm{S}}(i)$ remains bounded, while Y_{η} grows when increasing the scale) which leads to $F_{\eta \mathrm{S}}(n) \approx F_{\eta}(n)$, and a scaling behavior corresponding to the scaling of the correlated noise.

First, we consider $n_{1\times}$. Surprisingly, we find that for noise with any given correlation exponent α the crossover scale $n_{1\times}$ exhibits long-range power-law dependence of the period T — $n_{1\times} \sim T^{\theta_{\mathrm{T1}}}$, and the amplitude A_{S} — $n_{1\times} \sim (A_{\mathrm{S}})^{\theta_{\mathrm{A1}}}$ of the sinusoidal trend [see Fig. 1.8(a) and (b)]. We find that the "crossover exponents" θ_{T1} and θ_{A1} have the same magnitude but different sign — θ_{T1} is positive while θ_{A1} is negative. We also find that the magnitude of θ_{T1} and θ_{A1} increases for the larger values of the correlation exponents α of the noise. We present the values of θ_{T1} and θ_{A1} for different correlation exponent α in Table 1.2. To understand these power-law relations between $n_{1\times}$ and T, and between $n_{1\times}$ and A_{S}, and also how the crossover

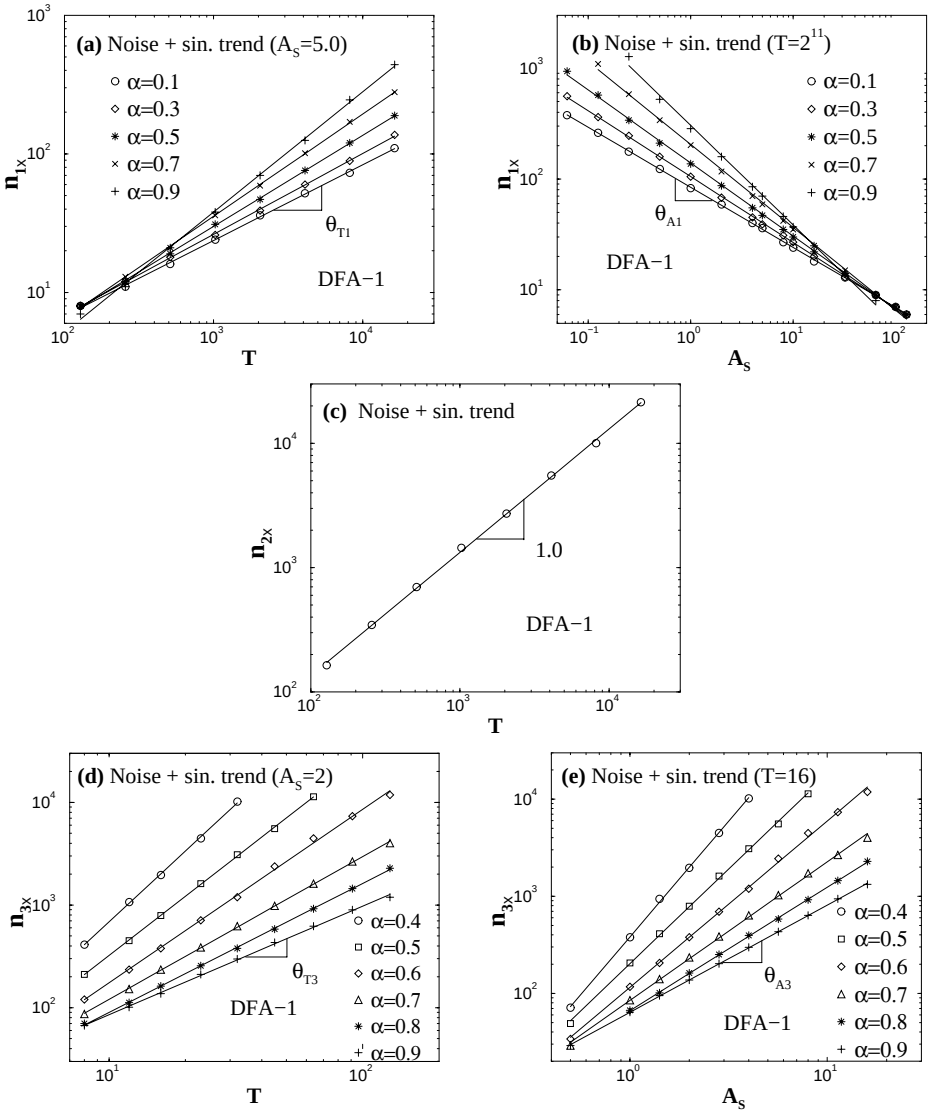

Fig. 1.8. (a) Power-law relation between the first crossover scale $n_{1\times}$ and the period T: $n_{1\times} \sim T^{\theta_{\rm T1}}$, where $\theta_{\rm T1}$ is a positive crossover exponent [see Table 1.2 and Eq. 1.10]. (b) Power-law relation between the first crossover $n_{1\times}$ and the amplitude of the sinusoidal trend $A_{\rm S}$: $n_{1\times} \sim A_{\rm S}^{\theta_{\rm A1}}$ where $\theta_{\rm A1}$ is a negative crossover exponent [Table 1.2 and Eq. (1.10)]. (c) The second crossover scale $n_{2\times}$ depends only on the period T: $n_{2\times} \sim T^{\theta_{\rm T2}}$, where $\theta_{\rm T2} \approx 1$. (d) Power-law relation between the third crossover $n_{3\times}$ and T: $n_{3\times} \sim T^{\theta_{\rm T3}}$. (e) Power-law relation between the third crossover $n_{3\times}$ and $A_{\rm S}$: $n_{3\times} \sim (A_{\rm S})^{\theta_{A3}}$. We find that $\theta_{\rm A3} = \theta_{\rm T3}$ [Table 1.3 and Eq. (1.11)].

scale $n_{1\times}$ depends on the correlation exponent α we employ the superposition rule [Eq. 1.6] and estimate $n_{1\times}$ analytically as the first intercept $n_{1\times}^{th}$ of $F_\eta(n)$ and $F_{\rm S}(n)$. From Eqs. (1.8) and (1.2), we obtain the following dependence of $n_{1\times}$ on T, $A_{\rm S}$ and α:

$$n_{1\times} = \left(\frac{b_0}{k_1}\frac{T}{A_{\rm S}}\right)^{1/(2-\alpha)} \tag{1.10}$$

From this analytical calculation we obtain the following relation between the two crossover exponents $\theta_{\rm T1}$ and $\theta_{\rm A1}$ and the correlation exponent α: $\theta_{\rm T1} = -\theta_{\rm A1} = 1/(2-\alpha)$, which is in a good agreement with the observed values of $\theta_{\rm T1}$, $\theta_{\rm A1}$ obtained from simulations [see Fig. 1.8(a) (b) and Table 1.2].

Table 1.2. $\theta_{\rm T1}$ and $\theta_{\rm A1}$ characterize the power-law dependence of crossover scale $n_{1\times}$ on the period T and amplitude $A_{\rm S}$ obtained from simulations: $n_{1\times} \sim T^{\theta_{\rm T1}}$ and $n_{1\times} \sim (A_{\rm S})^{\theta_{\rm A1}}$ [Fig. 1.8(a)(b)]. The values of $\theta_{\rm T1}$ and $\theta_{\rm A1}$ are in good agreement with the analytical predictions $\theta_{\rm T1} = -\theta_{\rm A1} = 1/(2-\alpha)$ [Eq. (1.10)].

α	$\theta_{\rm T1}$	-$\theta_{\rm A1}$	$1/(2-\alpha)$
0.1	0.55	0.54	0.53
0.3	0.58	0.59	0.59
0.5	0.66	0.66	0.67
0.7	0.74	0.75	0.77
0.9	0.87	0.90	0.91

Next, we consider $n_{2\times}$. Our analysis of the rms fluctuation function $F_{\rm S}(n)$ for the sinusoidal signal in Fig. 1.5 suggests that the crossover scale $F_{\rm S}(n)$ does not depend on the amplitude $A_{\rm S}$ of the sinusoidal. The behavior of the rms fluctuation function $F_{\eta{\rm S}}(n)$ for noise with superimposed sinusoidal trend in Fig. 1.6(a) and (b) indicates that $n_{2\times}$ does not depend on the correlation exponent α of the noise, since for both correlated ($\alpha = 0.9$) and anticorrelated ($\alpha = 0$) noise (T and $A_{\rm S}$ are fixed),

the crossover scale $n_{2\times}$ remains unchanged. We find that $n_{2\times}$ depends **only** on the period T of the sinusoidal trend and exhibits a long-range power-law behavior $n_{2\times} \sim T^{\theta_{\rm T2}}$ with a crossover exponent $\theta_{\rm T2} \approx 1$ (Fig. 1.8(c)) which is in agreement with the prediction of Eq.(1.7).

Table 1.3. These two exponents characterize the power-law relations: $n_{3\times} \sim T^{\theta_{\rm T3}}$ and $n_{3\times} \sim (A_{\rm S})^{\theta_{\rm A3}}$ [Fig. 1.8(c)(d)]. The values of θ_{p3} and θ_{a3} obtained from simulations are in good agreement with the analytical predictions $\theta_{\rm T3} = \theta_{\rm A3} = 1/\alpha$ [Eq. (1.11)].

α	$\theta_{\rm T3}$	$\theta_{\rm A3}$	$1/\alpha$
0.4	2.29	2.38	2.50
0.5	1.92	1.95	2.00
0.6	1.69	1.71	1.67
0.7	1.39	1.43	1.43
0.8	1.26	1.27	1.25
0.9	1.06	1.10	1.11

For the third crossover scale $n_{3\times}$, as for $n_{1\times}$ we find a power-law dependence on the period T, $n_{3\times} \sim T^{\theta_{T3}}$, and amplitude $A_{\rm S}$, $n_{3\times} \sim (A_{\rm S})^{\theta_{A3}}$,of the sinusoidal trend [see Fig. 1.8(d) and (e)]. However, in contrast to the $n_{1\times}$ case, we find that the crossover exponents $\theta_{\rm Tp3}$ and $\theta_{\rm A3}$ are equal and positive with decreasing values for increasing correlation exponents α. In Table 1.3, we present the values of these two exponents for different correlation exponent α. To understand how the scale $n_{3\times}$ depends on T, $A_{\rm S}$ and the correlation exponent α simultaneously, we again employ the superposition rule [Eq. (1.6)] and estimate $n_{3\times}$ as the second intercept $n_{3\times}^{th}$ of $F_\eta(n)$ and $F_{\rm S}(n)$. From Eqs. (1.9) and (1.2), we obtain the following dependence:

$$n_{3\times} = \left(\frac{1}{2\sqrt{2}\pi b_0} A_{\rm S} T \right)^{1/\alpha} . \tag{1.11}$$

From this analytical calculation we obtain $\theta_{\rm T3} = \theta_{\rm A3} = 1/\alpha$ which is in good agreement with the values of $\theta_{\rm T3}$ and $\theta_{\rm A3}$ observed from simulations [Table 1.3].

Finally, our simulations show that all three crossover scales $n_{1\times}$, $n_{2\times}$ and $n_{3\times}$ do not depend on the length of the signal N_{max}, since $F_\eta(n)$ and $F_{\rm S}(n)$ do not depend on N_{max} as shown in Eqs. (1.2), (1.6), (1.8), and (1.9).

1.4.3 Higher order DFA on pure sinusoidal trend

In the previous Sec. 1.4.2, we discussed how sinusoidal trends affect the scaling behavior of correlated noise when the DFA-1 method is applied. Since DFA-1 removes only constant trends in data, it is natural to ask how the observed scaling results will change when we apply DFA of order ℓ designed to remove polynomial trends of order lower than ℓ. In this section, we first consider the rms fluctuation $F_{\rm S}$ for a sinusoidal signal and then we study the scaling and crossover properties of $F_{\eta{\rm S}}$ for correlated noise with superimposed sinusoidal signal when higher order DFA is used.

We find that the rms fluctuation function $F_{\rm S}$ does not depend on the length of the signal N_{max}, and preserves a similar shape when different order-ℓ DFA method is used [Fig. 1.9]. In particular, $F_{\rm S}$ exhibits a crossover at a scale $n_{2\times}$ proportional to the period T of the sinusoidal: $n_{2\times} \sim T^{\theta_{\rm T2}}$ with $\theta_{\rm T2} \approx 1$. The crossover scale shifts to larger values for higher order ℓ [Fig. 1.5 and Fig. 1.9]. For the scale $n < n_{2\times}$, $F_{\rm S}$ exhibits an apparent scaling: $F_{\rm S} \sim n^{\alpha_{\rm S}}$ with an effective exponent $\alpha_{\rm S} = \ell + 1$. For DFA-1, we have $\ell = 1$ and recover $\alpha_{\rm S} = 2$ as shown in Eq. (1.8). For $n > n_{2\times}$, $F_{\rm S}(n)$ is a constant independent of the scale n, and of the order ℓ of the DFA method in agreement with Eq. (1.9).

Next, we consider $F_{\eta{\rm S}}(n)$ when DFA-ℓ with a higher order ℓ is used. We find that for all orders ℓ, $F_{\eta{\rm S}}(n)$ does not depend on the length of the signal N_{max} and exhibits three crossovers — at small, intermediate and large scales — similar behavior is reported for DFA-1 in Fig. 1.6. Since the crossover at small scales, $n_{1\times}$, and the

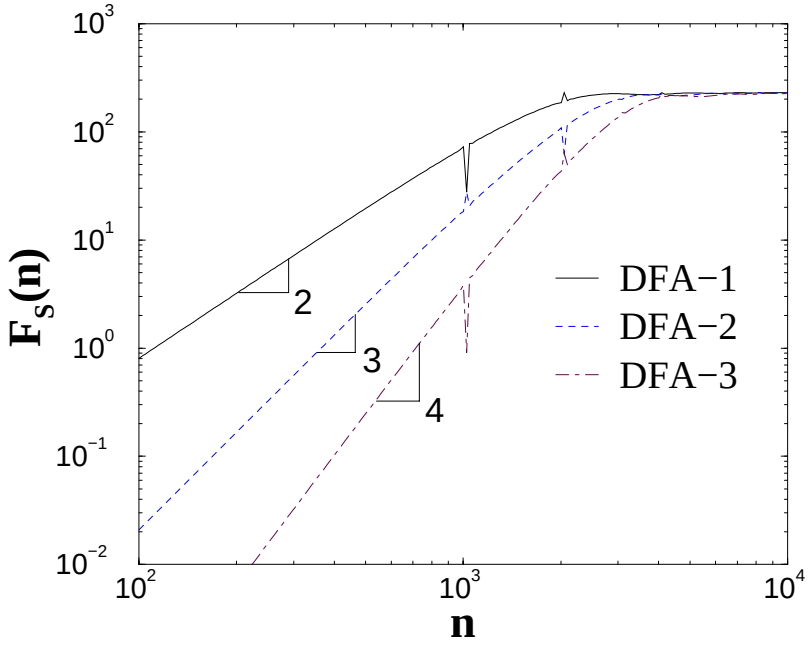

Fig. 1.9. The sinusoidal trend is given by the function $64\sin(2\pi i/2^{11})$ and the length of the signal is $N_{max} = 2^{17}$. The spurious singularities (spikes) arise from the discrete data we use for the sinusoidal function.

crossover at large scale, $n_{3\times}$, result from the "competition" between the scaling of the correlated noise and the effect of the sinusoidal trend (Figs. 1.6 and 1.7), using the superposition rule [Eq. (1.6)] we can estimate $n_{1\times}$ and $n_{3\times}$ as the intercepts of $F_\eta(n)$ and $F_{\rm S}(n)$ for the general case of DFA-ℓ.

For $n_{1\times}$ we find the following dependence on the period T, amplitude $A_{\rm S}$, the correlation exponent α of the noise, and the order ℓ of the DFA-ℓ method:

$$n_{1\times} \sim (T/A_{\rm S})^{1/(\ell+1-\alpha)} \tag{1.12}$$

For DFA-1, we have $\ell = 1$ and we recover Eq. (1.10). In addition, $n_{1\times}$ is shifted to larger scales when higher order DFA-ℓ is applied, due to the fact that the value of $F_{\rm S}(n)$ decreases when ℓ increases ($\alpha_{\rm S} = \ell + 1$, see Fig. 1.9).

For the third crossover observed in $F_{\eta{\rm S}}(n)$ at large scale $n_{3\times}$ we find for all orders

ℓ of the DFA-ℓ the following scaling relation:

$$n_{3\times} \sim (TA_{\rm S})^{1/\alpha}. \tag{1.13}$$

Since the scaling function $F_\eta(n)$ for correlated noise shifts vertically to lower values when higher order DFA-ℓ is used [see the discussion in Appendix .2 and Sec. 1.5.2], $n_{3\times}$ exhibits a slight shift to larger scales.

For the crossover $n_{2\times}$ in $F_{\eta{\rm S}}(n)$ at $F_{\eta{\rm S}}(n)$ at intermediate scales, we find: $n_{2\times} \sim T$. This relation is independent of the order ℓ of the DFA and is identical to the relation found for $F_{\rm S}(n)$ [Eq. (1.7)]. $n_{2\times}$ also exhibits a shift to larger scales when higher order DFA is used [see Fig. 1.9].

The reported here features of the crossovers in $F_{\eta{\rm S}}(n)$ can be used to identify low-frequency sinusoidal trends in noisy data, and to recognize their effects on the scaling properties of the data. This information may be useful when quantifying correlation properties in data by means of scaling analysis.

1.5 Noise with Power-law trends

In this section we study the effect of power-law trends on the scaling properties of noisy signals. We consider the case of correlated noise with superposed power-law trend $u(i) = A_{\rm P} i^\lambda$, when $A_{\rm P}$ is a positive constant, $i = 1, ..., N_{max}$, and N_{max} is the length of the signal. We find that when the DFA-1 method is used, the rms fluctuation function $F_{\eta{\rm P}}(n)$ exhibits a crossover between two scaling regions [Fig. 1.10]. This behavior results from the fact that at different scales n, either the correlated noise or the power-law trend is dominant, and can be predicted by employing the superposition rule:

$$[F_{\eta{\rm P}}(n)]^2 = [F_\eta(n)]^2 + [F_{\rm P}(n)]^2\,, \tag{1.14}$$

where $F_\eta(n)$ and $F_{\rm P}(n)$ are the rms fluctuation function of noise and the power-law trend respectively, and $F_{\eta{\rm P}}(n)$ is the rms fluctuation function for the superposition

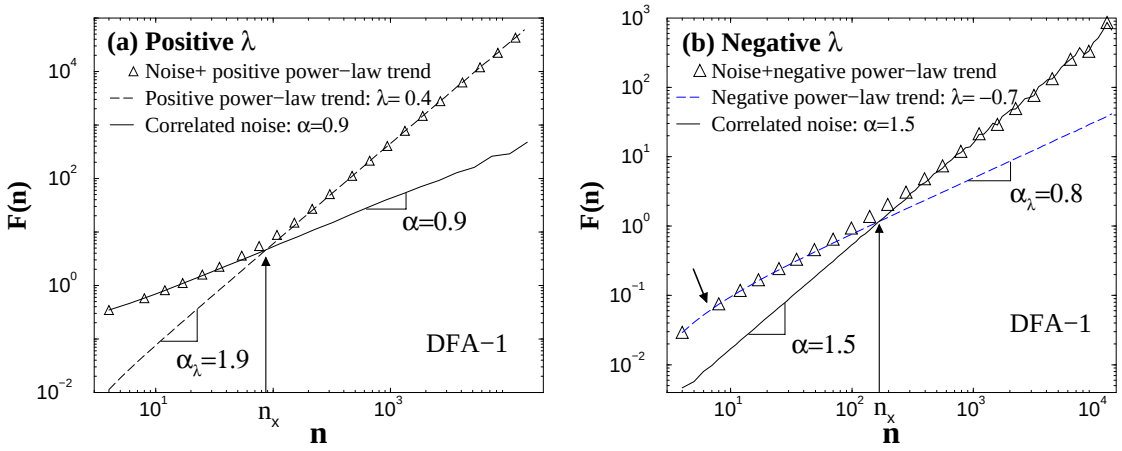

Fig. 1.10. Crossover behavior of the rms fluctuation function for correlated noise with a superimposed power-law trend. $F_{\eta \mathrm{P}}(n)$ (circles) is for correlated noise (of length $N_{max} = 2^{17}$) with a superimposed power-law trend $u(i) = A_{\mathrm{P}} i^{\lambda}$. The rms fluctuation function $F_{\eta}(n)$ for noise (solid line) and the rms fluctuation function $F_{\mathrm{P}}(n)$ (dash line) are also shown for comparison. DFA-1 method is used. (a) $F_{\eta \mathrm{P}}(n)$ for noise with correlation exponent $\alpha_{\lambda} = 0.9$, and power-law trend with amplitude $A_{\mathrm{P}} = 1000/(N_{max})^{0.4}$ and positive power $\lambda = 0.4$; (b) $F_{\eta \mathrm{P}}(n)$ for Brownian noise (integrated white noise, $\alpha_{\lambda} = 1.5$), and power-law trend with amplitude $A_{\mathrm{P}} = 0.01/\left(N_{max}\right)^{-0.7}$ and negative power $\lambda = -0.7$. Note, that although in both cases there is a "similar" crossover behavior for $F_{\eta \mathrm{P}}(n)$, the results in (a) and (b) represent completely opposite situations: while in (a) the power-law trend with positive power λ dominates the scaling of $F_{\eta \mathrm{P}}(n)$ at large scales, in (b) the power-law trend with negative power λ dominates the scaling at small scales, with arrow we indicate in (b) a weak crossover in $F_{\mathrm{P}}(n)$ (dashed lines) at small scales for negative power λ.

of the noise and the power-law trend. Since the behavior of $F_{\eta}(n)$ is known (Eq. (1.2) and Appendix .2), we can understand the features of $F_{\eta \mathrm{P}}(n)$, if we know how $F_{\mathrm{P}}(n)$ depends on the characteristics of the power-law trend. We note that the scaling behavior of $F_{\eta \mathrm{P}}(n)$ displayed in Fig. 1.10(a) is to some extent similar to the behavior of the rms fluctuation function $F_{\eta \mathrm{L}}(n)$ for correlated noise with a linear trend [Fig. 1.1] — e.g. the noise is dominant at small scales n, while the trend is dominant at large scales. However, the behavior $F_{\mathrm{P}}(n)$ is more complex than that of $F_{\mathrm{L}}(n)$ for the linear trend, since the effective exponent α_{λ} for $F_{\mathrm{P}}(n)$ can depend on the power λ

of the power-law trend. In particular, for negative values of λ, $F_{\rm P}(n)$ can become dominated at small scales (Fig. 1.10(b)) while $F_\eta(n)$ dominates at large scales — a situation completely opposite of noise with linear trend (Fig. 1.1) or with power-law trend with positive values for the power λ. Moreover, $F_{\rm P}(n)$ can exhibit crossover behavior at small scales [Fig. 1.10(b)] for negative λ which is not observed for positive λ. In addition $F_{\rm P}(n)$ depends on the order ℓ of the DFA method and the length N_{max} of the signal. We discuss the scaling features of the power-law trends in the following three subsections.

1.5.1 Dependence of $F_{\rm P}(n)$ on the power λ

First we study how the rms fluctuation function $F_{\rm P}(n)$ for a power-law trend $u(i) = A_{\rm P} i^\lambda$ depends on the power λ. We find that

$$F_{\rm P}(n) \sim A_{\rm P} n^{\alpha_\lambda}, \tag{1.15}$$

where α_λ is the effective exponent for the power-law trend. For positive λ we observe no crossovers in $F_{\rm P}(n)$ (Fig. 1.10(a)). However, for negative λ there is a crossover in $F_{\rm P}(n)$ at small scales n (Fig. 1.10(b)), and we find that this crossover becomes even more pronounced with decreasing λ or increasing the order ℓ of the DFA method, and is also shifted to larger scales [Fig. 1.11(a)].

Next, we study how the effective exponent α_λ for $F_{\rm P}(n)$ depends on the value of the power λ for the power-law trend. We examine the scaling of $F_{\rm P}(n)$ and estimate α_λ for $-4 < \lambda < 4$. In the cases when $F_{\rm P}(n)$ exhibits a crossover, in order to obtain α_λ we fit the range of larger scales to the right of the crossover. We find that for any order ℓ of the DFA-ℓ method there are three regions with different relations between α_λ and λ [Fig. 1.11(b)]:

(i) $\alpha_\lambda \approx \ell + 1$ for $\lambda > \ell - 0.5$ (region I);

(ii) $\alpha_\lambda \approx \lambda + 1.5$ for $-1.5 \leq \lambda \leq \ell - 0.5$ (region II);

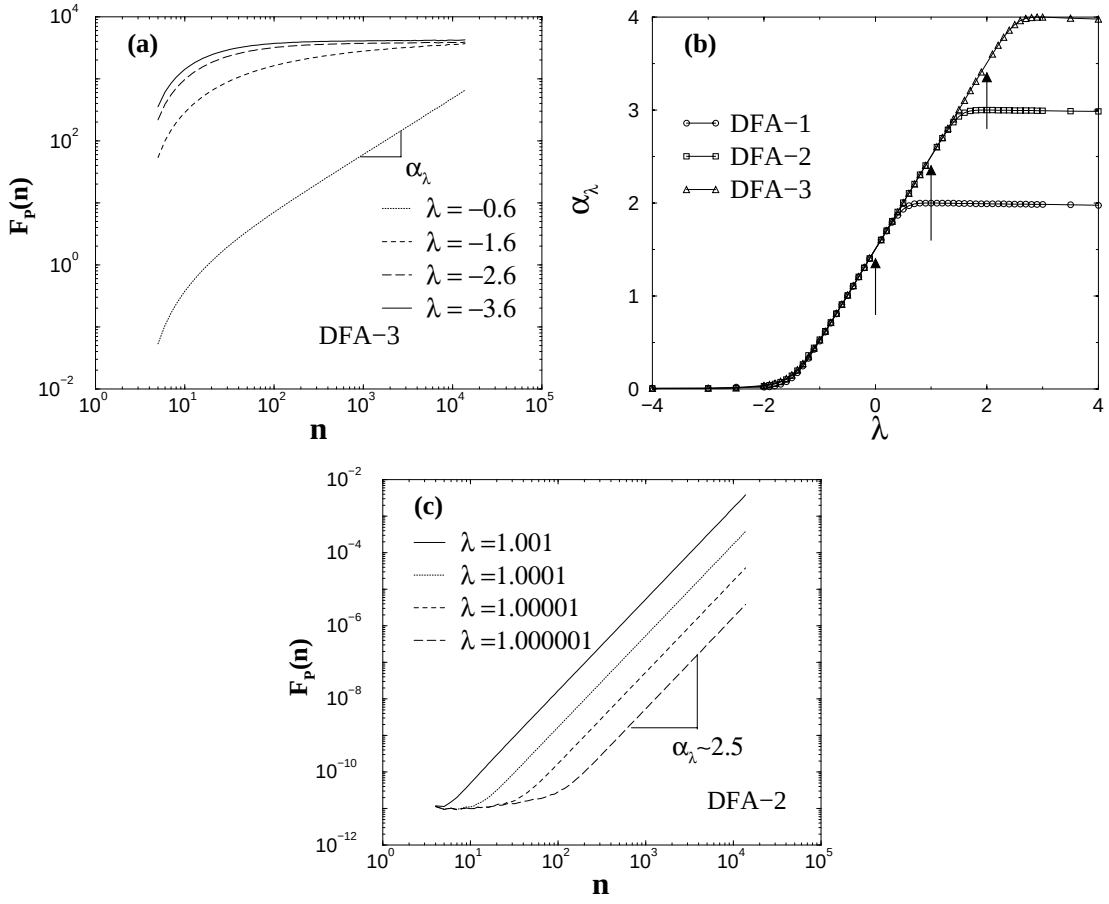

Fig. 1.11. Scaling behavior of rms fluctuation function $F_{\rm P}(n)$ for power-law trends.The trend is given by $u(i) \sim i^{\lambda}$, where $i = 1, ..., N_{max}$ and $N_{max} = 2^{17}$ is the length of the signal. (a) For $\lambda < 0$, $F_{\rm P}(n)$ exhibits crossover at small scales which is more pronounced with increasing the order ℓ of DFA-ℓ and decreasing the value of λ. Such crossover is not observed for $\lambda > 0$ when $F_{\rm P}(n) \sim n^{\alpha_\lambda}$ for all scales n [see Fig. 1.10(a)]. (b) Dependence of the effective exponent α_λ on the power λ for different order $\ell = 1, 2, 3$ of the DFA method. Three regions are observed depending on the order ℓ of the DFA: region I ($\lambda > \ell - 0.5$), where $\alpha_\lambda \approx \ell + 1$; region II ($-1.5 < \lambda < \ell - 0.5$), where $\alpha_\lambda = \lambda + 1.5$; region III ($\lambda < -1.5$), where $\alpha_\lambda \approx 0$. We note that for integer values of the power $\lambda = 0, 1, ..., \ell - 1$, where ℓ is the order of DFA we used, there is no scaling for $F_{\rm P}(n)$ and α_λ is not defined, as indicated by the arrows. (c) Asymptotic behavior near integer values of λ. $F_{\rm P}(n)$ is plotted for $\lambda \to 1$ when DFA-2 is used. Even for $\lambda - 1 = 10^{-6}$, we observe at large scales n a region with an effective exponent $\alpha_\lambda \approx 2.5$, This region is shifted to infinitely large scales when $\lambda = 1$.

(iii) $\alpha_\lambda \approx 0$ for $\lambda < -1.5$ (region III).

Note, that for integer values of the power λ ($\lambda = 0, 1, ..., m-1$), i.e. polynomial trends of order $m-1$, the DFA-ℓ method of order $\ell > m-1$ (ℓ is also an integer) leads to $F_{\rm P}(n) \approx 0$, since DFA-ℓ is designed to remove polynomial trends. Thus for a integer values of the power λ there is no scaling and the effective exponent α_λ is not defined if a DFA-ℓ method of order $\ell > \lambda$ is used [Fig. 1.11]. However, it is of interest to examine the asymptotic behavior of the scaling of $F_{\rm P}(n)$ when the value of the power λ is close to an integer. In particular , we consider how the scaling of $F_{\rm P}(n)$ obtained from DFA-2 method changes when $\lambda \to 1$ [Fig. 1.11(c)]. Surprisingly, we find that even though the values of $F_{\rm P}(n)$ are very small at large scales, there is a scaling for $F_{\rm P}(n)$ with a smooth convergence of the effective exponent $\alpha_\lambda \to 2.5$ when $\lambda \to 1$, according to the dependence $\alpha_\lambda \approx \lambda + 1.5$ established for region II [Fig. 1.11(b)]. At smaller scales there is a flat region which is due to the fact that the fluctuation function $Y(i)$ (Eq. (5)) is smaller than the precision of the numerical simulation.

1.5.2 Dependence of $F_{\rm P}(n)$ on the order ℓ of DFA

Another factor that affects the rms fluctuation function of the power-law trend $F_{\rm P}(n)$, is the order ℓ of the DFA method used. We first take into account the following.

(1) For integer values of the power λ, the power-law trend $u(i) = A_{\rm P} i^\lambda$ is a polynomial trend which can be perfectly filtered out by the DFA method of order $\ell > \lambda$, and as discussed in Sec. 1.3.2 and Sec. 1.5.1 [see Fig. 1.11(b) and (c)], there is no scaling for $F_{\rm P}(n)$. Therefore, in this section we consider only non-integer values of λ.

(2) For a given value of the power λ, the effective exponent α_λ can take different values depending on the order ℓ of the DFA method we use [see Fig. 1.11] —

e.g. for fixed $\lambda > \ell - 0.5$, $\alpha_\lambda \approx \ell + 1$. Therefore, in this section, we consider only the case when $\lambda < \ell - 0.5$ (Region II and III).

Since higher order DFA-ℓ provides a better fit for the data, the fluctuation function $Y(i)$ (Eq. (5)) decreases with increasing order ℓ. This leads to a vertical shift to smaller values of the rms fluctuation function $F(n)$ (Eq. (6)). Such a vertical shift is observed for the rms fluctuation function $F_\eta(n)$ for correlated noise (see Appendix .2), as well as for the rms fluctuation function of power-law trend $F_{\rm P}(n)$. Here we ask how this vertical shift in $F_\eta(n)$ and $F_{\rm P}(n)$ depends on the order ℓ of the DFA method, and if this shift has different properties for $F_\eta(n)$ compared to $F_{\rm P}(n)$. This information can help identify power-law trends in noisy data, and can be used to differentiate crossovers separating scaling regions with different types of correlations, and crossovers which are due to effects of power-law trends.

We consider correlated noise with a superposed power-law trend, where the crossover in $F_{\eta{\rm P}}(n)$ at large scales n results from the dominant effect of the power-law trend — $F_{\eta{\rm P}}(n) \approx F_{\rm P}(n)$ (Eq. (1.14) and Fig. 1.10(a)). We choose the power $\lambda < 0.5$, a range where for all orders ℓ of the DFA method the effective exponent α_λ of $F_{\rm P}(n)$ remains the same — i.e. $\alpha_\lambda = \lambda + 1.5$ (region II in Fig. 1.11(b)). For a superposition of an anticorrelated noise and power-law trend with $\lambda = 0.4$, we observe a crossover in the scaling behavior of $F_{\eta{\rm P}}(n)$, from a scaling region characterized by the correlation exponent $\alpha = 0.1$ of the noise, where $F_{\eta{\rm P}}(n) \approx F_\eta(n)$, to a region characterized by an effective exponent $\alpha_\lambda = 1.9$, where $F_{\eta{\rm P}}(n) \approx F_{\rm P}(n)$, for all orders $\ell = 1, 2, 3$ of the DFA-ℓ method [Fig. 1.12(a)]. We also find that the crossover of $F_{\eta{\rm P}}(n)$ shifts to larger scales when the order ℓ of DFA-ℓ increases, and that there is a vertical shift of $F_{\eta{\rm P}}(n)$ to lower values. This vertical shift in $F_{\eta{\rm P}}(n)$ at large scales, where $F_{\eta{\rm P}}(n) = F_{\rm P}(n)$, appears to be different in magnitude when different order ℓ of the DFA-ℓ method is used [Fig. 1.12(a)]. We also observe a less pronounced vertical shift at small scales where $F_{\eta{\rm P}}(n) \approx F_\eta(n)$.

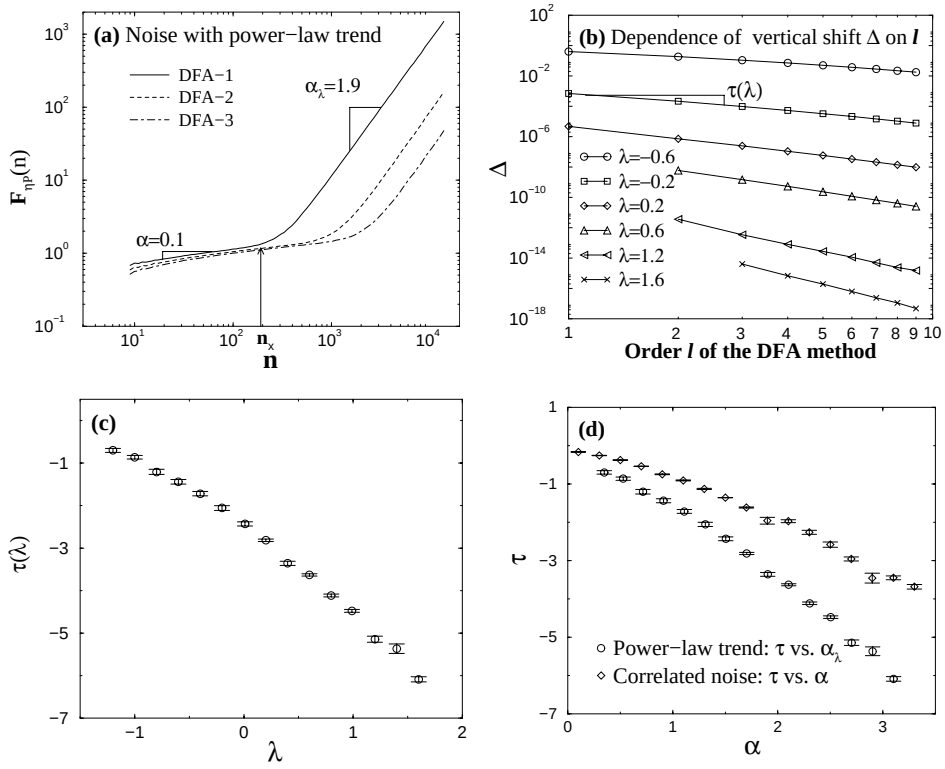

Fig. 1.12. Effect of higher order DFA-ℓ on the rms fluctuation function $F_{\eta \mathrm{P}}(n)$ for correlated noise with superimposed power-law trend. (a) $F_{\eta \mathrm{P}}(n)$ for anticorrelated noise with correlation exponent $\alpha = 0.1$ and a power-law $u(i) = A_{\mathrm{P}} i^{\lambda}$, where $A_{\mathrm{P}} = 25/\left(N_{max}\right)^{0.4}$, $N_{max} = 2^{17}$ and $\lambda = 0.4$. Results for different order $\ell = 1, 2, 3$ of the DFA method show (i) a clear crossover from a region at small scales where the noise dominates $F_{\eta \mathrm{P}}(n) \approx F_{\eta}(n)$, to a region at larger scales where the power-law trend dominates $F_{\eta \mathrm{P}}(n) \approx F_{\mathrm{P}}(n)$, and (ii) a vertical shift Δ in $F_{\eta \mathrm{P}}$ with increasing ℓ. (b) Dependence of the vertical shift Δ in the rms fluctuation function $F_{\mathrm{P}}(n)$ for power-law trend on the order ℓ of DFA-ℓ for different values of λ: $\Delta \sim \ell^{\tau(\lambda)}$. We define the vertical shift Δ as the y-intercept of $F_{\mathrm{P}}(n)$: $\Delta \equiv F_{\mathrm{P}}(n = 1)$. Note, that we consider only non-integer values for λ and that we consider the region $\lambda < \ell - 0.5$. Thus, for all values of λ the minimal order ℓ that can be used in the DFA method is $\ell > \lambda + 0.5$. e.g. for $\lambda = 1.6$ the minimal order of the DFA that can be used is $\ell = 3$ (for details see Fig. 1.11(b)). (c) Dependence of τ on the power λ (error bars indicate the regression error for the fits of $\Delta(l)$ in (b)). (d) Comparison of $\tau(\alpha_{\lambda})$ for $F_{\mathrm{P}}(n)$ and $\tau(\alpha)$ for $F_{\eta}(n)$. Faster decay of $\tau(\alpha_{\lambda})$ indicates larger vertical shifts for $F_{\mathrm{P}}(n)$ compared to $F_{\eta}(n)$ with increasing order ℓ of the DFA-ℓ.

Next, we ask how these vertical shifts depend on the order ℓ of DFA-ℓ. We define the vertical shift Δ as the y-intercept of $F_{\rm P}(n)$: $\Delta \equiv F_{\rm P}(n=1)$. We find that the vertical shift Δ in $F_{\rm P}(n)$ for power-law trend follows a power law: $\Delta \sim \ell^{\tau(\lambda)}$. We tested this relation for orders up to $\ell = 10$, and we find that it holds for different values of the power λ of the power-law trend [Fig. 1.12(b)]. Using Eq. (1.15) we can write: $F_{\rm P}(n)/F_{\rm P}(n=1) = n^{\alpha_\lambda}$, i.e. $F_{\rm P}(n) \sim F_{\rm P}(n=1)$. Since $F_{\rm P}(n=1) \equiv \Delta \sim \ell^{\tau(\lambda)}$ [Fig. 1.12(b)], we find that:

$$F_{\rm P}(n) \sim \ell^{\tau(\lambda)}. \tag{1.16}$$

We also find that the exponent τ is negative and is a decreasing function of the power λ [Fig. 1.12(c)]. Because the effective exponent α_λ which characterizes $F_{\rm P}(n)$ depends on the power λ [see Fig. 1.11(b)], we can express the exponent τ as a function of α_λ as we show in Fig. 1.12(d). This representation can help us compare the behavior of the vertical shift Δ in $F_{\rm P}(n)$ with the shift in $F_\eta(n)$. For correlated noise with different correlation exponent α, we observe a similar power-law relation between the vertical shift in $F_\eta(n)$ and the order ℓ of DFA-ℓ: $\Delta \sim \ell^{\tau(\alpha)}$, where τ is also a negative exponent which decreases with α. In Fig. 1.12(d) we compare $\tau(\alpha_\lambda)$ for $F_{\rm P}(n)$ with $\tau(\alpha)$ for $F_\eta(n)$, and find that for any $\alpha_\lambda = \alpha$, $\tau(\alpha_\lambda) < \tau(\alpha)$. This difference between the vertical shift for correlated noise and for a power-law trend can be utilized to recognize effects of power-law trends on the scaling properties of data.

1.5.3 Dependence of $F_{\rm P}(n)$ on the signal length N_{max}

Here, we study how the rms fluctuation function $F_{\rm P}(n)$ depends on the length N_{max} of the power-law signal $u(i) = A_{\rm P} i^\lambda$ ($i = 1, ..., N_{max}$). We find that there is a vertical shift in $F_{\rm P}(n)$ with increasing N_{max} [Fig. 1.13(a)]. We observe that when doubling the length N_{max} of the signal the vertical shift in $F_{\rm P}(n)$, which we define as $F_{\rm P}^{2N_{max}}/F_{\rm P}^{N_{max}}$, remains the same, independent of the value of N_{max}. This suggests

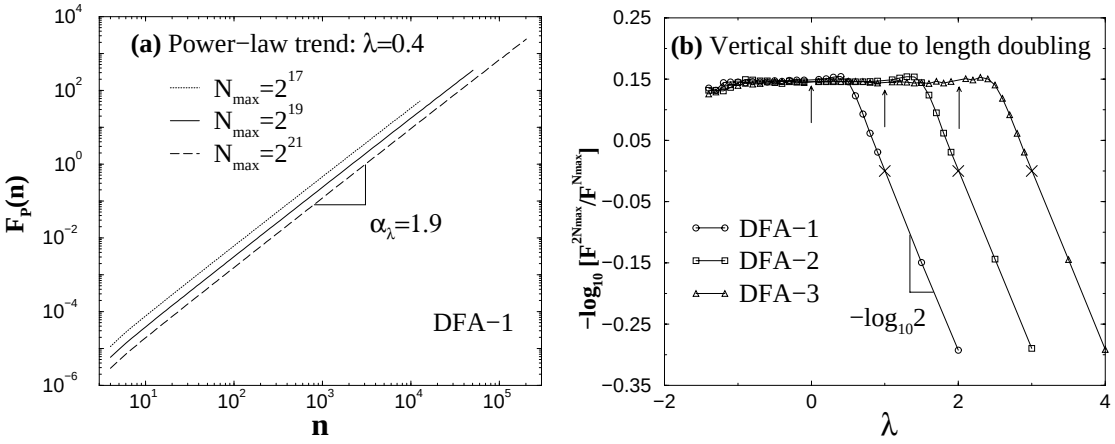

Fig. 1.13. Dependence of the rms fluctuation function $F_{\rm P}(n)$ for power-law trend on the length of the trend N_{max}. (a) A vertical shift is observed in $F_{\rm P}(n)$ for different values of N_{max} — N_{1max} and N_{2max}. The figure shows that the vertical shift , defined as $F_{\rm P}^{N_{1max}}(n)/F_{\rm P}^{N_{2max}}(n)$, does not depend on N_{max} but only on the ratio N_{1max}/N_{2max}, suggesting that $F_{\rm P}(n) \sim (N_{max})^{\gamma}$. (b) Dependence of the vertical shift on the power λ. For $\lambda < \ell - 0.5$ (ℓ is the order of DFA), we find a flat (constant) region characterized with effective exponent $\gamma = -0.5$ and negative vertical shift. For $\lambda > \ell - 0.5$, we find an exponential dependence of the vertical shift on λ. In this region, $\gamma = \lambda - \ell$, and the vertical shift can be negative (if $\lambda < \ell$) or positive (if $\lambda > \ell$). the slope of $-\log_{10}\left(F_{\rm P}^{2N_{max}}(n)/F_{\rm P}^{N_{max}}(n)\right)$ vs. λ is $-\log_{10} 2$ due to doubling the length of the signal N_{max}. This slope changes to $-\log_{10} m$ when N_{max} is increased m times while γ remains independent of N_{max}. For $\lambda = \ell$ there is no vertical shift, as marked with $\times$. Arrows indicate integer values of $\lambda < \ell$, for which values the DFA-ℓ method filters out completely the power-law trend and $F_{\rm P} = 0$.

a power-law dependence of $F_{\rm P}(n)$ on the length of the signal:

$$F_{\rm P}(n) \sim (N_{max})^{\gamma}\,, \tag{1.17}$$

where γ is an effective scaling exponent.

Next, we ask if the vertical shift depends on the power λ of the power-law trend. When doubling the length N_{max} of the signal, we find that for $\lambda < \ell - 0.5$, where ℓ is the order of the DFA method, the vertical shift is a constant independent of λ [Fig. 1.13(b)]. Since the value of the vertical shift when doubling the length N_{max}

is 2^{γ} (from Eq. (1.17)), the results in Fig. 1.13(b) show that γ is independent of λ when $\lambda < \ell - 0.5$, and that $-\log 2^{\gamma} \approx -0.15$, i.e. the effective exponent $\gamma \approx -0.5$.

For $\lambda > \ell - 0.5$, when doubling the length N_{max} of the signal, we find that the vertical shift 2^{γ} exhibits the following dependence on λ: $-\log_{10} 2^{\gamma} = \log_{10} 2^{\lambda-\ell}$, and thus the effective exponent γ depends on λ — $\gamma = \lambda - \ell$. For positive integer values of λ ($\lambda = \ell$), we find that $\gamma = 0$, and there is no shift in $F_{\rm P}(n)$, suggesting that $F_{\rm P}(n)$ does not depend on the length N_{max} of the signal, when DFA of order ℓ is used [Fig. 1.13]. Finally, we note that depending on the effective exponent γ, i.e. on the order ℓ of the DFA method and the value of the power λ, the vertical shift in the rms fluctuation function $F_{\rm P}(n)$ for power-law trend can be positive ($\lambda > \ell$), negative ($\lambda < \ell$), or zero ($\lambda = \ell$).

1.5.4 Combined effect on $F_{\rm P}(n)$ of λ, ℓ and N_{max}

We have seen that, taking into account the effects of the power λ (Eq. (1.15)), the order ℓ of DFA-ℓ (Eq. (1.16)) and the effect of the length of the signal N_{max} (Eq. (1.17)), we reach the following expression for the rms fluctuation function $F_{\rm P}(n)$ for a power-law trend $u(i) = A_{\rm P} i^{\lambda}$:

$$F_{\rm P}(n) \sim A_{\rm P} \cdot n^{\alpha_\lambda} \cdot \ell^{\tau(\lambda)} \cdot (N_{max})^{\gamma(\lambda)}\,, \tag{1.18}$$

For correlated noise, the rms fluctuation function $F_{\eta}(n)$ depends on the box size n (Eq. (1.2)) and on the order ℓ of DFA-ℓ (Sec. 1.5.2 and Fig. 1.12(a), (d)), and does not depend on the length of the signal N_{max}. Thus we have the following expression for $F_{\eta}(n)$

$$F_{\eta}(n) \sim n^{\alpha} \ell^{\tau(\alpha)}, \tag{1.19}$$

To estimate the crossover scale $n_{\times}$ observed in the apparent scaling of $F_{\eta{\rm P}}(n)$ for a correlated noise superposed with a power-law trend [Fig. 1.10(a), (b) and

Fig. 1.12(a)], we employ the superposition rule (Eq. (1.14)). From Eq. (1.18) and Eq. (1.19), we obtain $n_\times$ as the intercept between $F_{\rm P}(n)$ and $F_\eta(n)$:

$$n_\times \sim \left[A l^{\tau(\lambda)-\tau(\alpha)} \left(N_{max}\right)^\gamma \right]^{1/(\alpha-\alpha_\lambda)} . \tag{1.20}$$

To test the validity of this result, we consider the case of correlated noise with a linear trend. For the case of a linear trend ($\lambda = 1$) when DFA-1 ($\ell = 1$) is applied, we have $\alpha_\lambda = 2$ (see Appendix .4 and Sec. 1.5.1, Fig. 1.11(b)). Since in this case $\lambda = \ell = 1 > \ell - 0.5$ we have $\gamma = \lambda - \ell = 0$ (see Sec.1.5.3 Fig. 1.13(b)), and from Eq. (1.20) we recover Eq. (1.5).

1.6 Conclusion and Summary

In this chapter we show that the DFA method performs better than the standard R/S analysis to quantify the scaling behavior of noisy signals for a wide range of correlations, and we estimate the range of scales where the performance of the DFA method is optimal. We consider different types of trends superposed on correlated noise, and study how these trends affect the scaling behavior of the noise. We demonstrate that there is a competition between a trend and a noise, and that this competition can lead to crossovers in the scaling. We investigate the features of these crossovers, their dependence on the properties of the noise and the superposed trend. Surprisingly, we find that crossovers which are a result of trends can exhibit power-law dependences on the parameters of the trends. We show that these crossover phenomena can be explained by the superposition of the separate results of the DFA method on the noise and on the trend, assuming that the noise and the trend are not correlated, and that the scaling properties of the noise and the apparent scaling behavior of the trend are known. Our work may provide some help to differentiate between different types of crossovers — e.g. crossovers which separate scaling regions with different correlation properties may differ from crossovers which are an artifact

of trends. The results we present here could be useful for identifying the presence of trends and to accurately interpret correlation properties of noisy data.

Chapter 2

Effect of nonstationarities on detrended fluctuation analysis

2.1 Overview

Detrended fluctuation analysis (DFA) is a scaling analysis method used to quantify long-range power-law correlations in signals. Many physical and biological signals are "noisy", heterogeneous and exhibit different types of nonstationarities, which can affect the correlation properties of these signals. We systematically study the effects of three types of nonstationarities often encountered in real data. Specifically, we consider nonstationary sequences formed in three ways: (i) adding to a signal with known correlations a tunable concentration of random outliers or spikes with different amplitude, (ii) stitching together segments of data obtained from discontinuous experimental recordings, or removing some noisy and unreliable parts from continuous recordings and stitching together the remaining parts — a "cutting" procedure commonly used in preparing data prior to signal analysis, and (iii)generating a signal comprised of segments with different properties — e.g. different standard deviations or different correlation exponents. We compare the difference between the scaling re-

sults obtained for stationary correlated signals and correlated signals with these three types of nonstationarities. We find that introducing nonstationarities to stationary correlated signals leads to the appearance of crossovers in the scaling behavior and we study how the characteristics of these crossovers depend on: (a) the fraction and size of the parts cut out from the signal; (b) the concentration of spikes and their amplitudes; (c) the proportion between segments with different standard deviations or different correlations; and (d) the correlation properties of the stationary signal. We show how to develop strategies for pre-processing "raw" data prior to analysis, which will minimize the effects of nonstationarities on the scaling properties of the data and how to interpret the results of DFA for complex signals with different local characteristics.

2.2 Introduction to this chapter

In recent years, there has been growing evidence indicating that many physical and biological systems have no characteristic length scale and exhibit long-range power-law correlations. Traditional approaches such as the power-spectrum and correlation analysis are suited to quantify correlations in stationary signals [73, 74]. However, many signals which are outputs of complex physical and biological systems are non-stationary — the mean, standard deviation and higher moments, or the correlation functions are not invariant under time translation [73, 74]. Nonstationarity, an important aspect of complex variability, can often be associated with different trends in the signal or heterogeneous segments (patches) with different local statistical properties. To address this problem, detrended fluctuation analysis (DFA) was developed to accurately quantify long-range power-law correlations embedded in a nonstationary time series [4, 7]. This method provides a single quantitative parameter — the scaling exponent α — to quantify the correlation properties of a signal. One advantage of the DFA method is that it allows the detection of long-range power-law correlations in

noisy signals with embedded polynomial trends that can mask the true correlations in the fluctuations of a signal. The DFA method has been successfully applied to research fields such as DNA[4–6, 20, 27–33, 75, 76], cardiac dynamics [8–19, 21–26, 81–83], human gait [84], meteorology [51], climate temperature fluctuations [59, 60, 62], river flow and discharge [52, 53], neural receptors in biological systems [77], and economics [38–50]. The DFA method may also help identify different states of the same system with different scaling behavior — e.g., the scaling exponent α for heart-beat intervals is different for healthy and sick individuals [17, 19] as well as for waking and sleeping states [13, 24].

To understand the intrinsic dynamics of a given system, it is important to analyze and correctly interpret its output signals. One of the common challenges is that the scaling exponent is not always constant (independent of scale) and crossovers often exist — i.e., the value of the scaling exponent α differs for different ranges of scales [8, 13, 19, 78, 79]. A crossover is usually due to a change in the correlation properties of the signal at different time or space scales, though it can also be a result of nonstationarities in the signal. A recent work considered different types of nonstationarities associated with different trends (e.g., polynomial, sinusoidal and power-law trends) and systematically studied their effect on the scaling behavior of long-range correlated signals [71]. Here we consider the effects of three other types of nonstationarities which are often encountered in real data or result from "standard" data pre-processing approaches.

(i) *Signals with random spikes*

A second type of nonstationarity is due to the existence of spikes in data, which is very common in real life signals [8–19, 21–26, 81–84]. Spikes may arise from external conditions which have little to do with the intrinsic dynamics of the system. In this case, we must distinguish the spikes from normal intrinsic fluctuations in the system's output and filter them out when we attempt to quantify correlations. Alternatively, spikes may arise from the intrinsic dynamics of the system, rather

than being an epiphenomenon of external conditions. In this second case, careful considerations should be given as to whether the spikes should be filtered out when estimating correlations in the signal, since such "intrinsic" spikes may be related to the properties of the noisy fluctuations. Here, we consider only the simpler case – namely, when the spikes are independent of the fluctuations in the signal. The problem is how spikes affect the scaling behavior of correlated signals, e.g., what kind of crossovers they may possibly cause. We also demonstrate to what extent features of the crossovers depend on the statistical properties of the spikes. Furthermore, we show how to recognize if a crossover indeed indicates a transition from one type of underlying correlations to a different type, or if the crossover is due to spikes without any transition in the dynamical properties of the fluctuations.

(*ii*) *Signals with segments removed*

First we consider a type of nonstationarity caused by discontinuities in signals. Discontinuities may arise from the nature of experimental recordings – e.g., stock exchange data are not recorded during the nights, weekends and holidays [38–45]. Alternatively, discontinuities may be caused by the fact that some noisy and unreliable portions of continuous recordings must be discarded, as often occurs when analyzing physiological signals [8–19, 21–26, 81–83]. In this case, a common pre–processing procedure is to cut out the noisy, unreliable parts of the recording and stitch together the remaining informative segments before any statistical analysis is performed. One immediate problem is how such cutting procedure will affect the scaling properties of long-range correlated signals. A careful consideration should be given when interpreting results obtained from scaling analysis, so that an accurate estimate of the true correlation properties of the original signal may be obtained.

(*iii*) *Signals with different local behavior*

A third type of nonstationarity is associated with the presence of segments in a signal which exhibit different local statistical properties, e.g., different local standard deviations or different local correlations. Some examples include: (a) 24 hour

records of heart rate fluctuations are characterized by segments with larger standard deviation during stress and physical activity and segments with smaller standard deviation during rest [9]; (b) studies of DNA show that coding and non-coding regions are characterized by different types of correlations [6, 75]; (c) brain wave analysis of different sleep stages (rapid eye movement [REM] sleep, light sleep and deep sleep) indicates that the signal during each stage may have different correlation properties [80]; (d) heartbeat signals during different sleep stages exhibit different scaling properties[24]. For such complex signals, results from scaling analysis often reveal a very complicated structure. It is a challenge to quantify the correlation properties of these signals. Here, we take a first step toward understanding the scaling behavior of such signals.

We study these three types of nonstationarities embedded in correlated signals. We apply the DFA method to stationary correlated signals and identical signals with artificially imposed nonstationarities, and compare the difference in the scaling results. (*i*) We find that cutting segments from a signal and stitching together the remaining parts does not affect the scaling for positively correlated signals. However, this cutting procedure strongly affects anti-correlated signals, leading to a crossover from an anti-correlated regime (at small scales) to an uncorrelated regime (at large scales). (*ii*) For the correlated signals with superposed random spikes, we find that the scaling behavior is a superposition of the scaling of the signal and the apparent scaling of the spikes. We analytically prove this superposition relation by introducing a *superposition rule*. (*iii*) For the case of complex signals comprised of segments with different local properties, we find that their scaling behavior is a superposition of the scaling of the different components — each component containing only the segments exhibiting identical statistical properties. Thus, to obtain the scaling properties of the signal, we need only to examine the properties of each component — a much simpler task than analyzing the original signal.

The layout of the chapter is as follows: In Sec. 2.3, we consider the effect of

random spikes on correlated signals. We show that the superposition of spikes and signals can be explained by a superposition rule derived in Appendix .3. In Sec. 2.4, we compare the scaling properties of correlated signals before and after removing some segments from the signals. In Sec. 2.5, we study signals comprised of segments with different local behavior. We systematically examine all resulting crossovers, their conditions of existence, and their typical characteristics associated with the different types of nonstationarity. We summarize our findings in Sec. 2.6.

2.3 Signals with random spikes

Another type of nonstationarity is due to the existence of spikes in data, which is very common in real life signals [8–19, 21–26, 81–84]. Spikes may arise from external conditions which have little to do with the intrinsic dynamics of the system. In this case, we must distinguish the spikes from normal intrinsic fluctuations in the system's output and filter them out when we attempt to quantify correlations. Alternatively, spikes may arise from the intrinsic dynamics of the system, rather than being an epiphenomenon of external conditions. In this second case, careful considerations should be given as to whether the spikes should be filtered out when estimating correlations in the signal, since such "intrinsic" spikes may be related to the properties of the noisy fluctuations. Here, we consider only the simpler case – namely, when the spikes are independent of the fluctuations in the signal. We study how spikes affect the scaling behavior of correlated signals, e.g., what kind of crossovers they may possibly cause.

First, we generate surrogate nonstationary signals by adding random spikes to a stationary correlated signal $u(i)$ [see Sec. .2 and Fig. 2.1(a-c)].

We find that the correlation properties of the nonstationary signal with spikes depend on the scaling exponent α of the stationary signal and the scaling exponent α_{sp} of the spikes. When uncorrelated spikes ($\alpha_{sp} = 0.5$) are added to a correlated

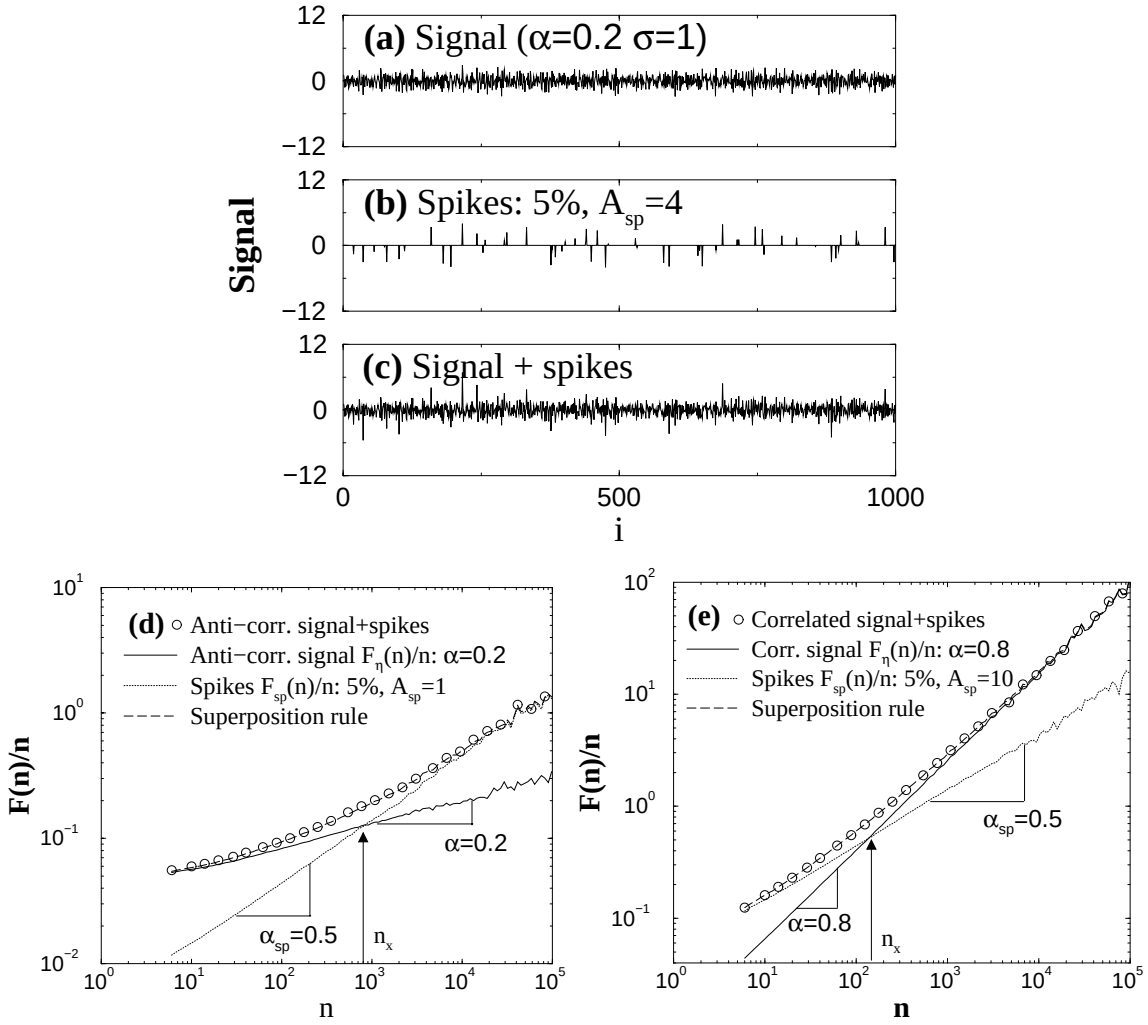

Fig. 2.1. (a) An example of an anti-correlated signal $u(i)$ with scaling exponent $\alpha = 0.2$, $N_{max} = 2^{20}$ and standard deviation $\sigma = 1$. (b) A series of uncorrelated spikes ($\alpha_{sp} = 0.5$) at 5% randomly chosen positions (concentration $p = 0.05$) and with uniformly distributed amplitudes A_{sp} in the interval $[-4, 4]$. (c) The superposition of the signals in (a) and (b). (d) Scaling behavior of an anti-correlated signal $u(i)$ ($\alpha = 0.2$) with spikes ($A_{sp} = 1$, $p = 0.05$, $\alpha_{sp} = 0.5$). For $n < n_\times$, $F(n)/n \approx F_\eta(n)/n \sim n^\alpha$, where $F_\eta(n)/n$ is the scaling function of the signal $u(i)$. For $n > n_\times$, $F(n)/n \approx F_{sp}(n)/n \sim n^{\alpha_{sp}}$. (e) Scaling behavior of a correlated signal $u(i)$ ($\alpha = 0.8$) with spikes ($A_{sp} = 10$, $p = 0.05$, $\alpha_{sp} = 0.5$). For $n < n_\times$, $F(n)/n \approx F_{sp}(n)/n \sim n^{\alpha_{sp}}$. For $n > n_\times$, $F(n)/n \approx F_\eta(n)/n \sim n^\alpha$. Note that when $\alpha = \alpha_{sp} = 0.5$, there is no crossover.

or anti-correlated stationary signal [Fig 2.1(d) and (e)], we observe a change in the scaling behavior with a crossover at a characteristic scale $n_\times$. For anti-correlated signals ($\alpha < 0.5$) with random spikes, we find that at scales smaller than $n_\times$, the scaling behavior is close to the one observed for the stationary anti-correlated signal without spikes, while for scales larger than $n_\times$, there is a crossover to random behavior. In the case of correlated signals ($\alpha > 0.5$) with random spikes, we find a different crossover from uncorrelated behavior at small scales, to correlated behavior at large scales with an exponent close to the exponent of the original stationary correlated signal. Moreover, we find that spikes with a very small amplitude can cause strong crossovers in the case of anti-correlated signals, while for correlated signals, identical concentrations of spikes with a much larger amplitude do not affect the scaling. Based on these findings, we conclude that uncorrelated spikes with a sufficiently large amplitude can affect the DFA results at large scales for signals with $\alpha < 0.5$ and at small scales for signals with $\alpha > 0.5$.

To better understand the origin of this crossover behavior, we first study the scaling of the spikes only [see Fig. 2.1(b)]. By varying the concentration p ($0 \leq p \leq 1$) and the amplitude A_{sp} of the spikes in the signal, we find that for the general case when the spikes may be correlated, the r.m.s. fluctuation function behaves as

$$F_{sp}(n)/n = k_0 \sqrt{p} A_{sp} n^{\alpha_{sp}}, \tag{2.1}$$

where k_0 is a constant and α_{sp} is the scaling exponent of the spikes.

Next, we investigate the analytical relation between the DFA results obtained from the original correlated signal, the spikes and the superposition of signal and spikes. Since the original signal and the spikes are not correlated, we can use a *superposition rule* (see [71] and Appendix .3) to derive the r.m.s. fluctuation function $F(n)/n$ for the correlated signal with spikes:

$$[F(n)/n]^2 = [F_\eta(n)/n]^2 + [F_{sp}(n)/n]^2, \tag{2.2}$$

where $F_\eta(n)/n$ and $F_{sp}(n)/n$ are the r.m.s. fluctuation function for the signal and the spikes, respectively. To confirm this theoretical result, we calculate $\sqrt{[F_\eta(n)/n]^2 + [F_{sp}(n)/n]^2}$ [see Figs. 2.1(d), (e)] and find this Eq. (2.2) is remarkably consistent with our experimental observations.

Using the superposition rule, we can also theoretically predict the crossover scale $n_\times$ as the intercept between $F_\eta(n)/n$ and $F_{sp}(n)/n$, i.e., where $F_\eta(n_\times) = F_{sp}(n_\times)$. We find that

$$n_\times = \left(\sqrt{p} A_{sp} \frac{k_0}{b_0}\right)^{1/(\alpha - \alpha_{sp})}, \tag{2.3}$$

since the r.m.s. fluctuation function for the signal and the spikes are $F_\eta(n)/n = b_0 n^\alpha$ [71] and $F_{sp}(n)/n = k_0 \sqrt{p} A_{sp} n^{\alpha_{sp}}$ [Eq. (2.1)], respectively. This result predicts the position of the crossover depending on the parameters defining the signal and the spikes.

Our result derived from the superposition rule can be useful to distinguish two cases: (*i*) the correlated stationary signal and the spikes are independent (e.g., the case when a correlated signal results from the intrinsic dynamics of the system while the spikes are due to external perturbations); and (*ii*) the correlated stationary signal and the spikes are dependent (e.g., both the signal and the spikes arise from the intrinsic dynamics of the system). In the latter case, the identity in the superposition rule is not correct (see Appendix .3).

2.4 Signals with segments removed

In this section, we study the effect of nonstationarity caused by removing segments of a given length from a signal and stitching together the remaining parts — a "cutting" procedure often used in pre-processing data prior to analysis. To address this question, we first generate a stationary correlated signal $u(i)$ (see Sec. .2) of length N_{max} and a scaling exponent α, using the modified Fourier filtering method[67]. Next, we divide this signal into N_{max}/W non-overlapping segments of size W and randomly

remove some of these segments. Finally, we stitch together the remaining segments in the signal $u(i)$ [Fig. 2.2(a)], thus obtaining a surrogate nonstationary signal which is characterized by three parameters: the scaling exponent α, the segment size W and the fraction of the signal $u(i)$, which is removed.

We find that the scaling behavior of such a nonstationary signal strongly depends on the scaling exponent α of the original stationary correlated signal $u(i)$. As illustrated in Fig. 2.2(b), for a stationary *anti-correlated* signal with $\alpha = 0.1$, the cutting procedure causes a crossover in the scaling behavior of the resultant nonstationary signal. This crossover appears even when only 1% of the segments are cut out. At the scales larger than the crossover scale $n_\times$ the r.m.s. fluctuation function behaves as $F(n) \sim n^{0.5}$, which means an uncorrelated randomness, i.e., the anti-correlation has been completely destroyed in this regime. For all anti-correlated signals with exponent $\alpha < 0.5$, we observe a similar crossover behavior. This result is surprising, since researchers often take for granted that a cutting procedure before analysis does not change the scaling properties of the original signal. Our simulation shows that this assumption is not true, at least for anti-correlated signals.

Next, we investigate how the two parameters — the segment size W and the fraction of points cut out from the signal — control the effect of the cutting procedure on the scaling behavior of anti-correlated signals. For the fixed size of the segments ($W = 20$), we find that the crossover scale $n_\times$ *decreases* with *increasing* the fraction of the cutout segments [Fig. 2.2(c)]. Furthermore, for anti-correlated signals with small values of the scaling exponent α, e.g., $\alpha = 0.1$ and $\alpha = 0.2$, we find that $n_\times$ and the fraction of the cutout segments display an approximate power-law relationship. For a fixed fraction of the removed segments, we find that the crossover scale $n_\times$ *increases* with *increasing* the segment size W [Fig. 2.2(d)]. To minimize the effect of the cutting procedure on the correlation properties, it is advantageous to cut smaller number of segments of larger size W. Moreover, if the segments which need to be removed are too close (e.g., at a distance shorter than the size of the segments), it may

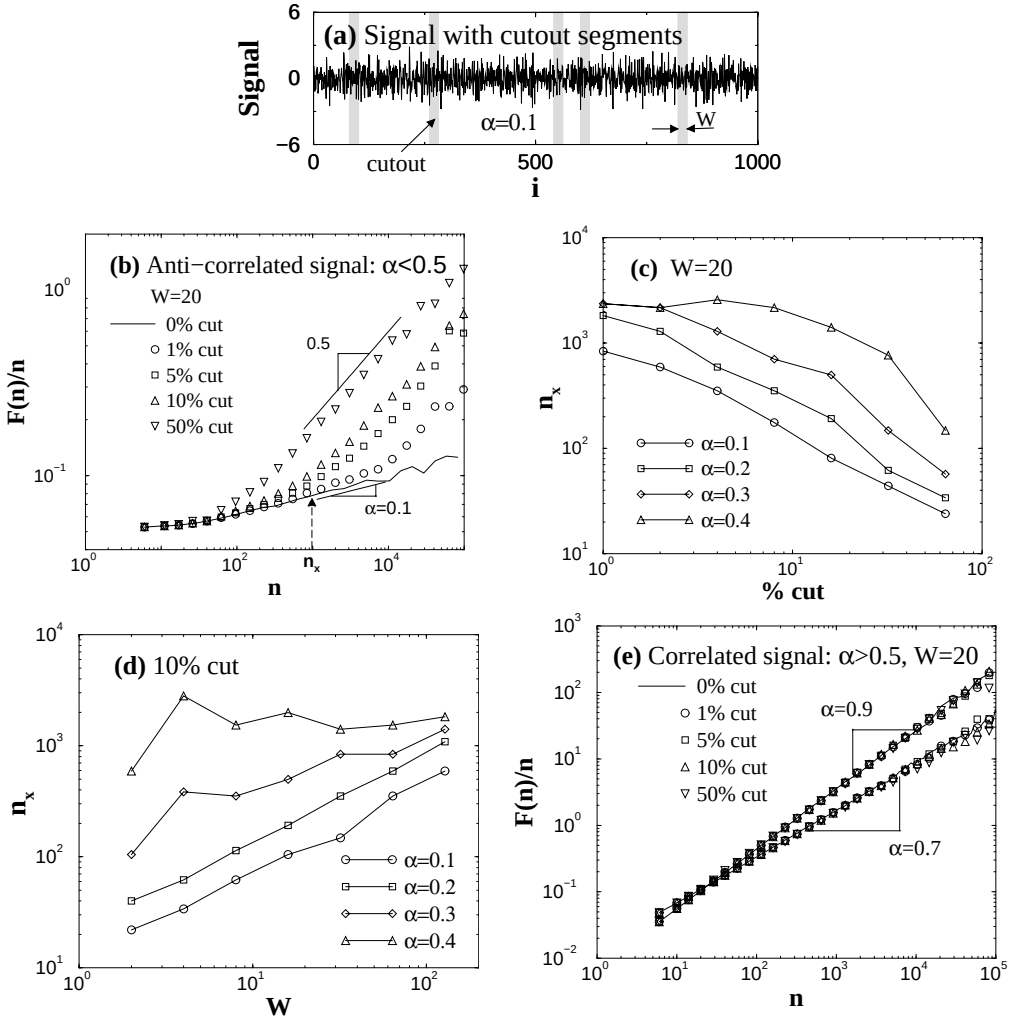

Fig. 2.2. Effects of the "cutting" procedure on the scaling behavior of stationary signals. $N_{max} = 2^{20}$ is the number of points in the signals (standard deviation $\sigma = 1$) and W is the size of the cutout segments. (a) A stationary signal with 10% of the points removed. The removed parts are presented by shaded segments of size $W = 20$ and the remaining parts are stitched together. (b) Scaling behavior of signals obtained from an anti-correlated stationary signal after the cutting procedure. A crossover appears at scale $n_\times$ that decreases with increasing the fraction of points removed from the signal. Dependence of the crossover scale $n_\times$ on the fraction (c) and on the size W (d) of the cutout segments for anti-correlated signals with different scaling exponent α. (e) Cutting procedure applied to correlated signals ($\alpha > 0.5$). In contrast to (b), no discernible effect on the scaling behavior is observed even when up to 50% of the points in the signals are removed.

be advantageous to cut out both the segments and a part of the signal between them. This will effectively increase the size of the segment W without substantially changing the fraction of the signal which is cut out, leading to an increase in the crossover scale $n_\times$. Such strategy would minimize the effect of this type of nonstationarity on the scaling properties of data. For small values of the scaling exponent α ($\alpha < 0.25$), we find that $n_\times$ and W follow power-law relationships [Fig. 2.2(d)]. The reason we do not observe a power-law relationship between $n_\times$ and W and between $n_\times$ and the fraction of cutout segments for the values of the scaling exponent α close to 0.5 may be due to the fact that the crossover regime becomes broader when it separates scaling regions with similar exponents, thus leading to uncertainty in defining $n_\times$. For a fixed W and a fixed fraction of the removed segments [see Figs. 2.2(c) and (d)], we observe that $n_\times$ increases with the increasing value of the scaling exponent α, i.e., the effect of the cutting procedure on the scaling behavior decreases when the anti-correlations in the signal are weaker (α closer to 0.5).

Finally, we consider the case of correlated signals $u(i)$ with $1.5 > \alpha > 0.5$. Surprisingly, we find that the scaling of correlated signals is not affected by the cutting procedure. This observation remains true independently of the segment size W — from very small $W = 5$ up to very large $W = 5000$ segments — even when up to 50% of the segments are removed from a signal with $N_{max} \sim 10^6$ points [Fig. 2.2(e)].

2.5 Signals with different local standard deviations

Here we consider nonstationary signals comprised of segments with the same local scaling exponent, but different local standard deviations. We first generate a stationary correlated signal $u(i)$ (see Sec. .2) with fixed standard deviation $\sigma_1 = 1$. Next, we divide the signal $u(i)$ into non-overlapping segments of size W. We then

randomly choose a fraction p of the segments and amplify the standard deviation of

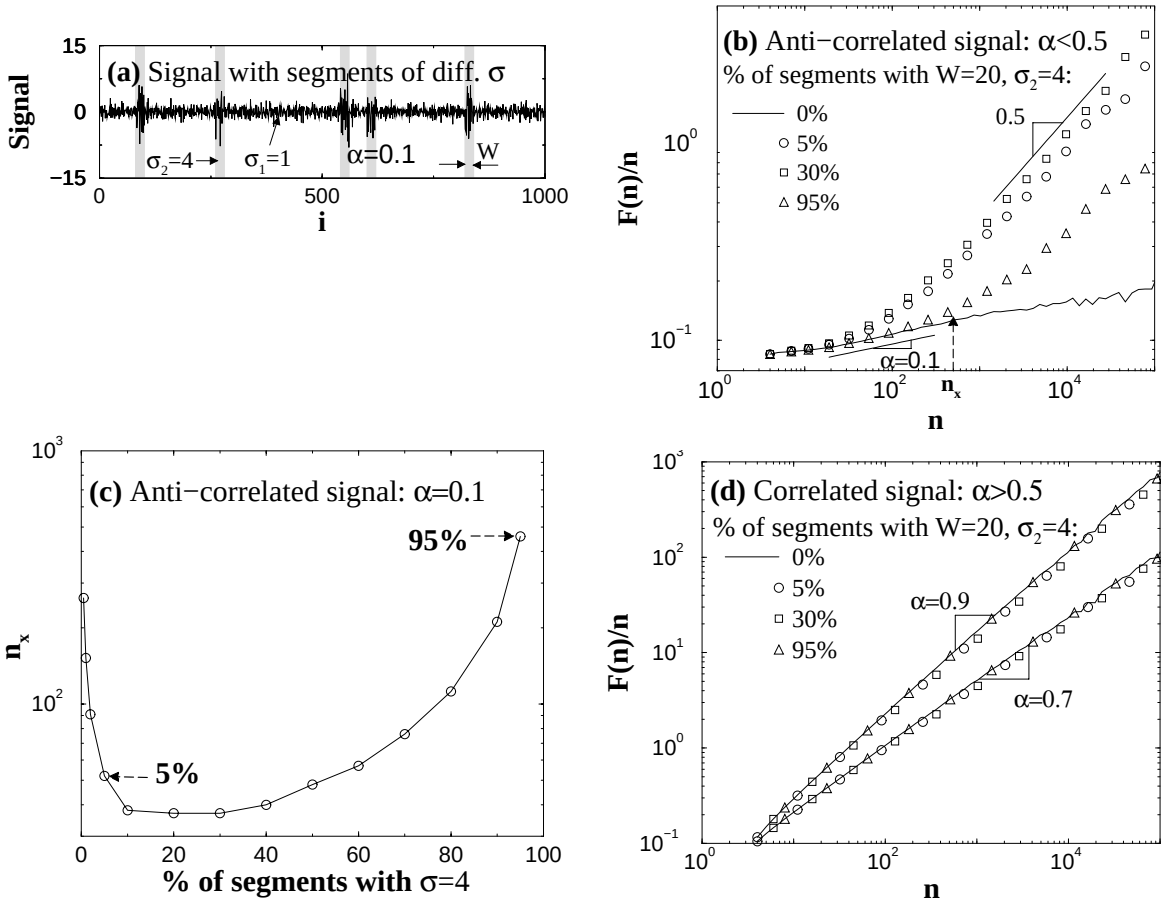

Fig. 2.3. (a) Anti-correlated signal ($\alpha = 0.1$) with standard deviation $\sigma_1 = 1$ and amplified segments with standard deviation $\sigma_2 = 4$. The size of each segment is $W = 20$ and the fraction of the amplified segments is $p = 0.1$ from the total length of the signal ($N_{max} = 2^{20}$). (b) Scaling behavior of the signal in (a) for a different fraction p of the amplified segments (after normalization of the globe standard deviation to unity). A crossover from anti-correlated behavior ($\alpha = 0.1$) at small scales to random behavior ($\alpha = 0.5$) at large scales is observed. (c) Dependence of the crossover scale $n_\times$ on the fraction p of amplified segments for the signal in (a). Here we choose $\Delta = 0.04$. (d) Scaling behavior of nonstationary signals obtained from correlated stationary signals ($1 > \alpha > 0.5$) with standard deviation $\sigma_1 = 1$, for a different fraction of the amplified segments with $\sigma_2 = 4$. No difference in the scaling is observed, compared to the original stationary signal.

the signal in these segments, $\sigma_2 = 4$ [Fig.2.3(a)]. Finally, we normalize the entire signal to global standard deviation $\sigma = 1$ by dividing the value of each point of the signal by $\sqrt{(1-p)\sigma_1^2 + p\sigma_2^2}$.

For nonstationary *anti-correlated* signals ($\alpha < 0.5$) with segments characterized by two different values of the standard deviation, we observe a crossover at scale $n_\times$ [Fig.2.3(b)]. For small scales $n < n_\times$, the behavior is anti-correlated with an exponent equal to the scaling exponent α of the original stationary anti-correlated signal $u(i)$. For large scales $n > n_\times$, we find a transition to random behavior with exponent 0.5, indicating that the anti-correlations have been destroyed. The dependence of crossover scale $n_\times$ on the fraction p of segments with larger standard deviation is shown in Fig. 2.3(c) ($n_\times$ is determined from the difference Δ of $\log_{10}[F(n)/n]$ between the nonstationary signal with amplified segments and the original stationary signal). The dependence is not monotonic because for $p = 0$ and $p = 1$, the local standard deviation is constant throughout the signal, i.e., the signal becomes stationary and thus there is no crossover. Note the asymmetry in the value of $n_\times$ — a much smaller value of $n_\times$ for $p = 0.05$ compared to $p = 0.95$ [see Fig. 2.3(b-c)]. This result indicates that very few segments with a large standard deviation (compared to the rest of the signal) can have a strong effect on the anti-correlations in the signal. Surprisingly, the same fraction of segments with a small standard deviation (compared to the rest of the signal) does not affect the anti-correlations up to relatively large scales.

For nonstationary *correlated* signals ($\alpha > 0.5$) with segments characterized by two different values of the standard deviation, we surprisingly find no difference in the scaling of $F(n)/n$, compared to the stationary correlated signals with constant standard deviation [Fig. 2.3(d)]. Moreover, this observation remains valid for different sizes of the segments W and for different values of the fraction p of segments with larger standard deviation. We note that in the limiting case of very large values of σ_2/σ_1, when the values of the signal in the segments with standard deviation σ_1 could be considered close to "zero", the results in Fig. 2.3(d) do not hold.

2.6 Conclusions

In this chapter we studied the effects of three different types of nonstationarities using the DFA correlation analysis method. Specifically, we consider sequences formed in three ways: (*i*) stitching together segments of signals obtained from discontinuous experimental recordings, or removing some noisy and unreliable segments from continuous recordings and stitching together the remaining parts; (*ii*) adding random outliers or spikes to a signal with known correlations, and (*iii*) generating a signal composed of segments with different properties — e.g. different standard deviations or different correlations. We compare the difference between the scaling results obtained for stationary correlated signals and for correlated signals with artificially imposed nonstationarities.

(*ii*) Signals with superposed random spikes. We find that for an anti-correlated signal with superposed spikes at small scales, the scaling behavior is close to that of the stationary anti-correlated signal without spikes. At large scales, there is a crossover to random behavior. For a correlated signal with spikes, we find a different crossover from uncorrelated behavior at small scales to correlated behavior at large scales with an exponent close to the exponent of the original stationary signal. We also find that the spikes with identical density and amplitude may cause strong effect on the scaling of an anti-correlated signal while they have a much smaller or no effect on the scaling of a correlated signal — when the two signals have the same standard deviations. We investigate the characteristics of the scaling of the spikes only and find that the scaling behavior of the signal with random spikes is a superposition of the scaling of the signal and the scaling of the spikes. We analytically prove this superposition relation by introducing a *superposition rule*.

(*ii*) We find that removing segments from a signal and stitching together the remaining parts does not affect the scaling behavior of positively correlated signals ($1.5 \geq \alpha > 0.5$), even when up to 50% of the points in these signals are removed.

However, such a cutting procedure strongly affects anti-correlated signals, leading to a crossover from an anti-correlated regime (at small scales) to an uncorrelated regime (at large scales). The crossover scale $n_\times$ increases with increasing value of the scaling exponent α for the original stationary anti-correlated signal. It also depends both on the segment size and the fraction of the points cut out from the signal: (1) $n_\times$ decreases with increasing fraction of cutout segments, and (2) $n_\times$ increases with increasing segment size. Based on our findings, we propose an approach to minimize the effect of cutting procedure on the correlation properties of a signal: When two segments which need to be removed are on distances shorter than the size of the segment, it is advantageous to cut out both the segments and the part of the signal between them.

(*iii*) Signals composed of segments with different local properties. We find that For nonstationary correlated signals comprised of segments which are characterized by two different values of the standard deviation, there is no difference in the scaling behavior compared to stationary correlated signals with constant standard deviation. For nonstationary anti-correlated signals, we find a crossover at scale $n_\times$. For small scales $n < n_\times$, the scaling behavior is similar to that of the stationary anti-correlated signals with constant standard deviation. For large scales $n > n_\times$, there is a transition to random behavior. We also find that very few segments with large standard deviation can strongly affect the anti-correlations in the signal. In contrast, the same fraction of segments with standard deviation smaller than the standard deviation of the rest of the anti-correlated signal has much weaker effect on the scaling behavior — $n_\times$ is shifted to larger scales.

Part III

Human Motor Activity

Chapter 3

Non-Random Fluctuations and Multi-scale Dynamics of Human Activity

3.1 Overview

We investigate if known extrinsic and intrinsic factors fully account for the complex features observed in recordings of human activity as measured from forearm motion in subjects undergoing their regular daily routine [85, 86]. We demonstrate that the apparently random forearm motion possesses dynamic patterns characterized by robust scale-invariant and nonlinear features. These patterns remain stable from one subject to another and are unaffected by changes in the average activity level that occur within individual subjects throughout the day and on different days of the week, since they persist during daily routine and when the same subjects undergo time-isolation laboratory experiments designed to account for the circadian phase and to control the known extrinsic factors. Further, by modeling the scheduled events imposed throughout the laboratory protocols, we demonstrate that they can-

not account for the observed scaling patterns in activity fluctuations. We attribute these patterns to a previously unrecognized intrinsic nonlinear multi-scale control mechanism of human activity that is independent of known extrinsic factors such as random and scheduled events, as well as the known intrinsic factors which possess a single characteristic time scale such as circadian and ultradian rhythms.

3.2 Introduction to this Chapter

Activity is one of the defining features of life. Control of human activity is complex, being influenced by many factors both extrinsic (work, recreation, reactions to unforeseen random events) and intrinsic (the circadian pacemaker that influences our sleep/wake cycle [87, 88] and ultradian oscillators with shorter time scales [89, 90]). The extrinsic factors may account for the apparently random fluctuations in human motion observed over short time scales while the intrinsic rhythms may account for the underlying regularity in average activity level over longer periods of up to 24 h. Further, human activity correlates with important physiological functions including whole body oxygen consumption and heart rate [13, 91–93].

To investigate the effect of extrinsic factors related to physical activity on the daily pattern of cardiac dynamics, we studied long records of data from wrist actigraphy. It is often assumed that an increase in cardiac risk in the period of 9-11AM is simply related to the increase of the activity level. An important question is if the level of activity is simply a result of extrinsic stimuli (in which case there would be no self-similar structure to the activity fluctuations) or it is regulated by an intrinsic mechanism, which relates through neural pathways to the endogenous circadian pacemaker and the neuroautonomic cardiac control.

Traditionally activity fluctuations are considered as random noise and have been ignored. We hypothesize that there are systematic patterns in the activity fluctuations that may be independent of known extrinsic and intrinsic factors. To test our

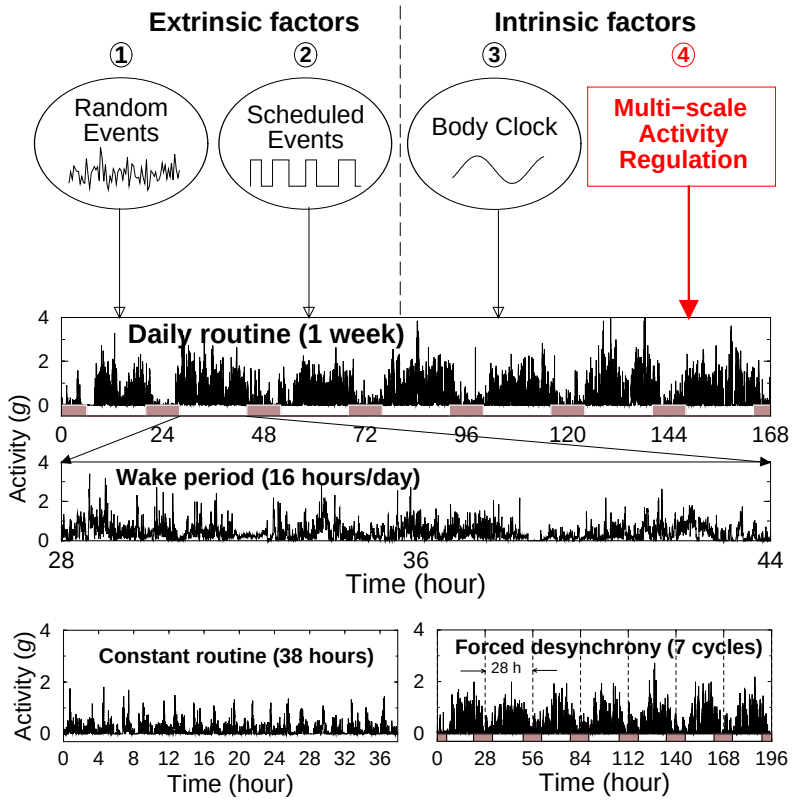

Fig. 3.1. Independent contributors to the complex dynamics of human activity, depicted at the top of the figure, include: ① reaction to extrinsic random events, ② scheduled activities and, ③ intrinsic factors, notably the endogenous circadian pacemaker which influences the sleep/wake cycle. Our findings of scale-invariant activity patterns (Figs. 3.2–3.7) indicate a heretofore-unidentified intrinsic multi-scale control of human activity ④, which is independent of other extrinsic and intrinsic factors such as ①, ②, and ③. The second panel illustrates an actual one-week recording of human activity [94] during the daily routine protocol. Data structure highlights a 24-h sleep/wake periodic change in the mean activity — lowest during sleep (filled bars). The third panel, expanding a 16-h section of wakefulness, also shows patches of high and low average activity levels with apparent erratic fluctuations at various time scales. The bottom left panel is an activity recording from the same subject during the constant routine protocol with much lower average activity values compared to daily routine. The clear 2-h cycle is a result of scheduled laboratory events. The bottom right panel shows activity levels in the same subject during the forced desynchrony protocol, characterized by a 28-h sleep/wake cycle (as opposed to the 24-h rhythm in activity data during the daily routine).

hypotheses, we evaluate the structure of human activity during wakefulness, using: (i) probability distribution analysis; (ii) power spectrum analysis, and (iii) fractal scaling and nonlinear analysis. To elucidate the presence of an intrinsic activity control center independent of known circadian, ultradian, scheduled and random factors, we apply 3 complementary protocols (See Appendix .6).

• *Daily routine protocol*: We record activity data throughout two consecutive weeks in 16 healthy ambulatory domiciliary subjects (8 males, 8 females, 19-44 years, mean 27 years) performing their routine daily activities. The only imposed constraints are that subjects go to bed and arise at the same time each day (8 h sleep opportunity) and that they are not permitted to have daytime naps (Fig. 3.1).

• *Constant routine protocol*: To assess intrinsic activity controllers (i.e. circadian or other neural centers) independent of scheduled and random external influences, activity recordings are made in the laboratory throughout 38 h of constant posture (semi-recumbent), wakefulness, environment (21^oC, dim light [$<$ 8 lux]), dietary intake and scheduled events (Appendix .6.2) [95, 96]. This protocol is performed in a subset of subjects (7 males, 4 females) that participated in the daily routine protocol. These highly controlled and constant experimental conditions result in reduced average and variance of activity levels.

• *Forced desynchrony protocol*: To test for the presence of heretofore unidentified intrinsic activity control centers, independent of known activity regulators (circadian pacemaker), while accounting for scheduled and random external influences, we employ the validated Forced desynchrony (FD) protocol (Appendix .6.2) [88]. Six (4 male, 2 female) of the 16 subjects that participated in the daily routine protocol completed the FD limb of the study. For eight days subjects remain in constant dim light (to avoid "resetting" the body clock). Sleep periods are delayed by 4 h every day, such that subjects live on recurring 28 h "days", while all scheduled activities become desynchronized from the endogenous circadian pacemaker. Thus, as measurements occur across all phases of the circadian clock, the effect of intrinsic

circadian influences can be removed [88]. Average activity level and activity variance are also significantly reduced due to laboratory-imposed restrictions on the subject's activity (Fig. 3.1).

3.3 Intrinsic patterns in activity

3.3.1 Common distribution form

When the same subject is studied in different protocols, we find large differences in the probability distributions (Fig. 3.2). For example, during wakefulness greater values of activity occur most frequently during the daily routine, intermediate activity values occur during the forced desynchrony, and the highest frequency of low activity values is seen during the constant routine (Fig. 3.2a). Indeed, the largest activity values encountered during the constant routine protocol are approximately two orders of magnitude less frequent than similar activity values encountered in the daily routine protocol. We find major differences between individuals in the distribution of activity values during the daily routine protocol (Fig. 3.2b). Such differences are expected given the different daily schedules, environments, and reactions to random events.

To test if the individual probability density curves follow a common functional form, we appropriately rescale the distributions of activity values on both axes to account for differences in average activity level and standard deviation while preserving the normalization to unit area. We divide the activity values by a constant, A_0, and multiply the probability density function by the same constant, where A_0 is the activity value before rescaling of each individual curve for which the cumulative probability (i.e., the area under the density function curve) is 60%. We find a remarkable similarity in the shapes of the probability distributions for each subject in all three protocols (Figs. 3.2 a, e), and for all individuals when in the same protocol

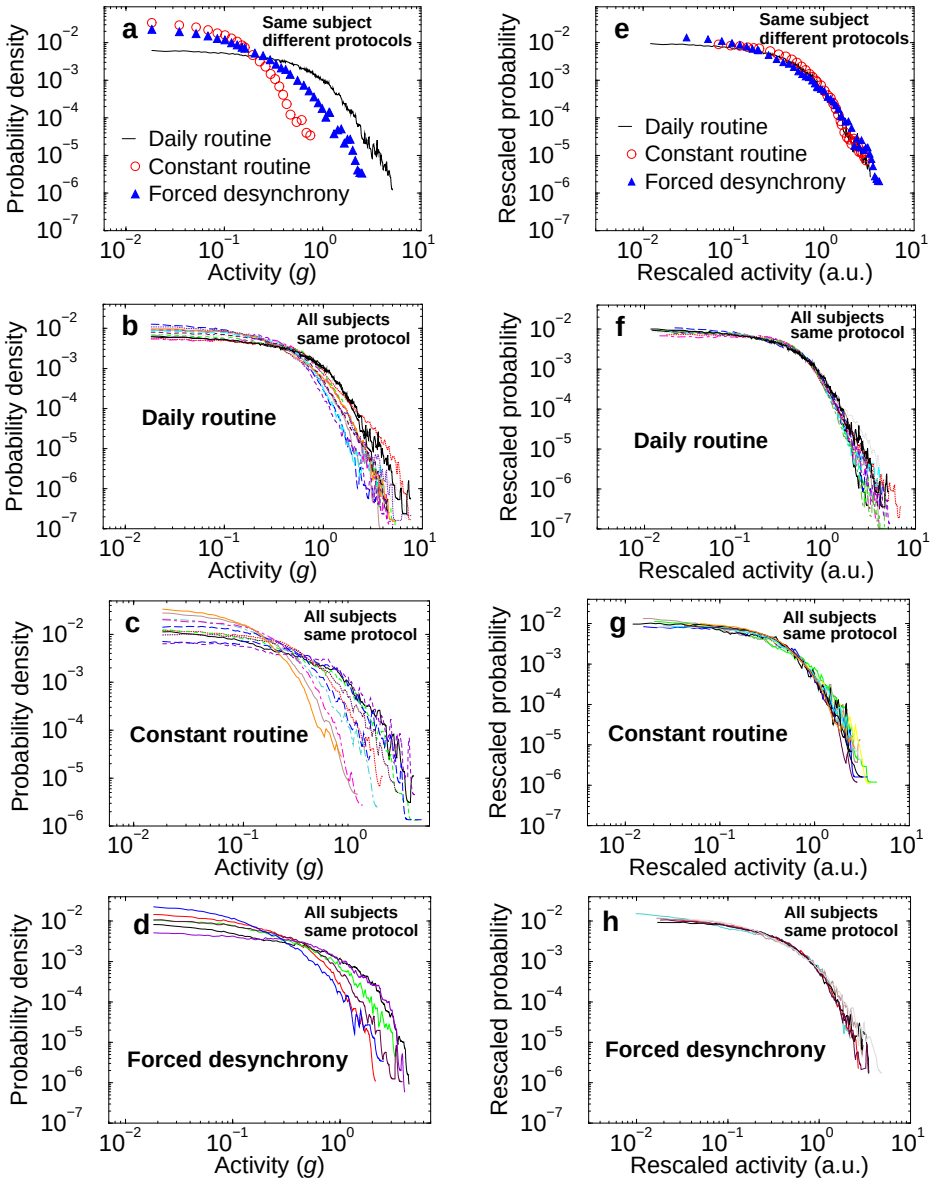

Fig. 3.2. **(a)** Probability distributions of activity values during wakefulness for an individual subject during 14 consecutive days of daily routine, 38 h of constant routine and 8 days of the forced desynchrony protocol. Probability distributions for all subjects during **(b)** the daily routine protocol, **(c)** the constant routine, and **(d)** the forced desynchrony protocol, indicate large difference between individuals. **(e)** – **(h)** Same probability distributions as in (a) – (d), after appropriately rescaling both axes. Data points for all subjects and for all three protocols collapse onto a single curve.

(Fig. 3.2f, g, h). The existence of a *universal* form of the probability distribution, independent of activity level in all individuals and in all protocols (Fig. 3.3a), suggests that a *common* underlying mechanism may account for the overall distribution of activity.

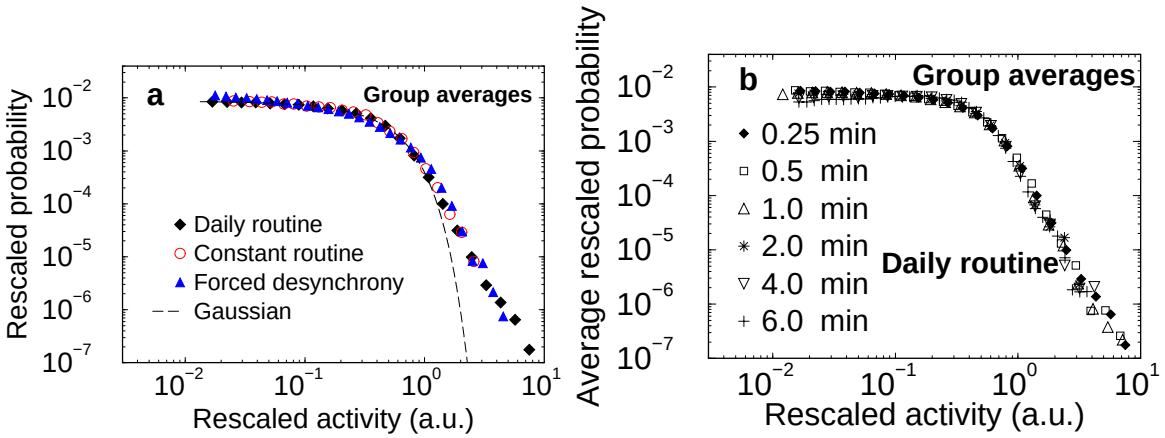

Fig. 3.3. **(a)** Group average of the rescaled distributions during all three protocols. All distributions collapse onto a single curve, suggesting a common underlying mechanism of activity regulation. The same rescaling procedure as in Fig. 3.2 is used. **(b)** Group average of all individual distributions rescaled as in (a) obtained for varied time windows during the daily routine.

This probability distribution when plotted on a log-log scale reveals different characteristics above and below a distinct crossover point (Fig. 3.3a). At scales above the crossover activity level there is pronounced non-Gaussian tail (Fig. 3.3a). This tail on the log-log plot represents a power-law form, indicating an intrinsic self-similar structure for a range of activity values. Moreover, we find that the observed shape of the rescaled probability distribution remains unchanged when the data series are reanalyzed using a variety of observation windows ranging from 15 s to 6 min (Fig. 3.3b). This stability of the probability distribution over a range of time scales indicates that the underlying dynamic mechanisms controlling the activity have similar statistical properties on different time scales. Statistical self-similarity is a defining characteristic of fractal objects and is reminiscent of a wide

class of physical systems with universal scaling properties. Our finding of a universal form of the probability distribution raises the possibility of an intrinsic mechanism that influences activity values in a self-similar "fractal" manner, that is unrelated to the individual's daily and weekly schedules, reactions to the environment, the average level of activity, the phase of the circadian pacemaker, and the time scale of observation.

3.3.2 Search for ultradian rhythms

We next perform power spectral analyses for all three protocols to determine whether there exist any systematic intrinsic ultradian rhythms of activity with periods of less than 24 h duration [89, 97]. The data for each individual exhibit occasional peaks

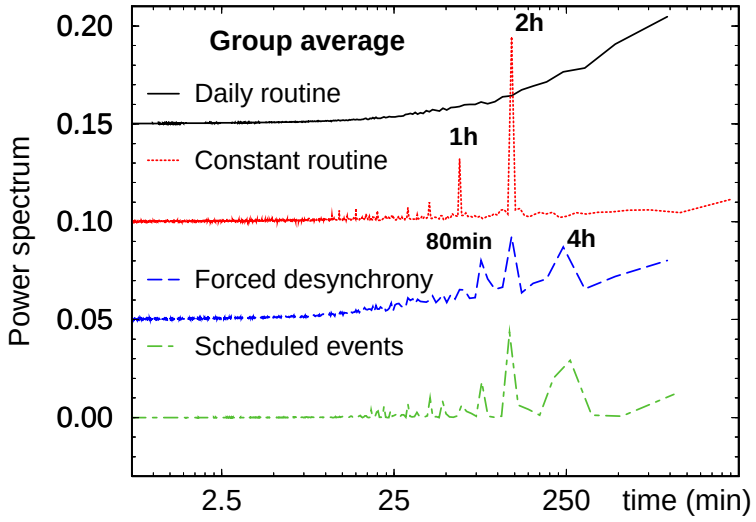

Fig. 3.4. Curves are vertically offset. Power spectra are shown with decreasing frequency from left to right. Smooth behavior of the daily routine curve suggests absence of periodic rhythms in the ultradian range. The spectral density peaks for the simulated scheduled activity data representing controlled scheduled events during the protocol (bottom curve) match the peaks observed in the original human activity data recorded during the forced desynchrony protocol. Our analysis and simulation suggest that the observed peaks in the power spectrum are due to scheduled laboratory events and cannot be attributed to endogenous ultradian rhythms.

in the daily routine protocol for periods ranging from 30 min to 4 h. However, we find no systematic ultradian rhythms within individuals from week to week, and no systematic ultradian rhythms in the group average for the daily routine protocol (Fig. 3.4). The only systematic rhythms that are ostensibly in the ultradian range which emerge in the group data are at 4 h during the forced desynchrony protocol (with harmonics at 2 h and 80 min) and at 2 h during the constant routine protocol (with harmonics at 1 h and 30 min) (Fig. 3.1 and Fig. 3.4). These peaks are caused by the controlled scheduled activities in the laboratory and are extrinsic to the body as they also occur in simulated scheduled activity data that assumes specific activity values for each scheduled behavior imposed throughout the laboratory protocols (Fig. 3.4). Thus, we find no evidence of systematic intrinsic ultradian rhythms in our data.

3.3.3 Long-range power-law correlations

To provide further insight into the dynamic control of activity, we next examine the temporal organization in the fluctuations in activity values. We perform detrended fluctuation analysis (DFA) which quantifies correlations in the activity fluctuations after accounting for nonstationarity in the data by subtracting underlying polynomial trends [4, 5, 71, 72]. The DFA method quantifies the root mean square fluctuations, $F(n)$, of a signal at different time scales n. Power-law functional form, $F(n) \sim n^{\alpha}$, indicates self-similarity (fractal scaling). The parameter α, called the scaling exponent, quantifies the correlation properties in the signal: if α=0.5, there is no correlation (random noise); if $\alpha < 0.5$, the signal is anticorrelated, where large activity values are more likely to be followed by small activity values; if $\alpha > 0.5$, there are positive correlations, where large activity values are more likely to be followed by large activity values (and vice versa for small activity values).

Figure 3.5a shows that $F(n)$ for a typical subject during wakefulness exhibits a

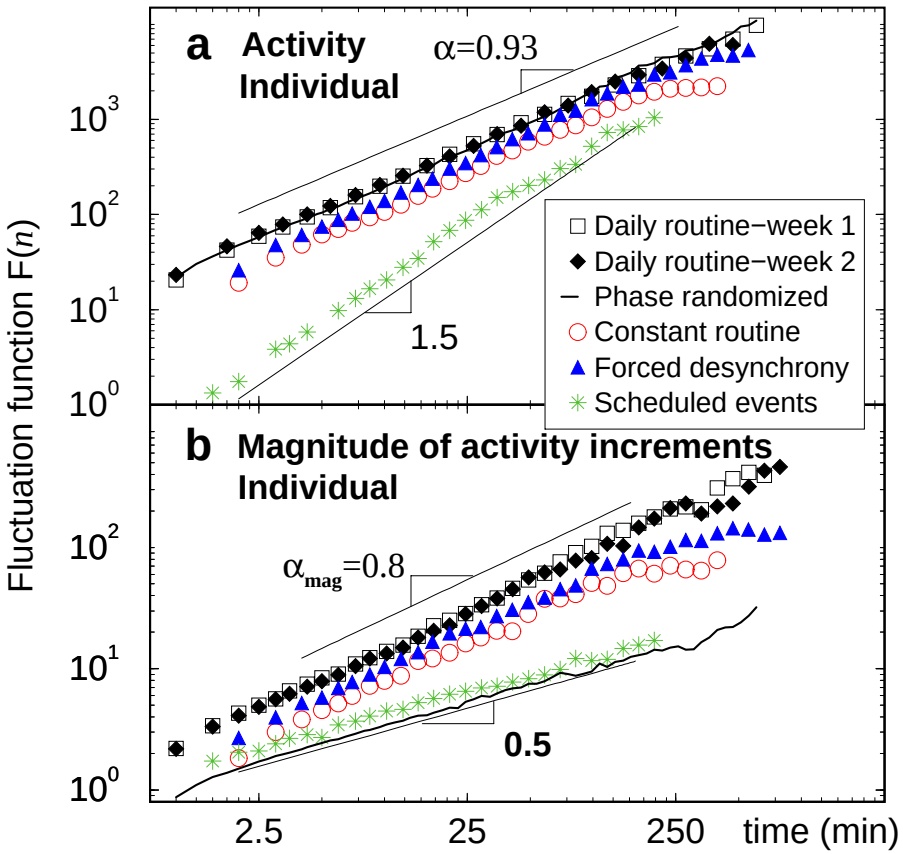

Fig. 3.5. **(a)** DFA scaling of activity fluctuation for a subject during wakefulness, demonstrating strong positive correlations on time scales from seconds to hours. **(b)** DFA scaling of the magnitude series of activity increments for the same signals as in (a). A scaling exponent $\alpha_{\rm mag} \approx 0.8$ of similar value is observed for all three protocols, consistent with robust nonlinear dynamics.

power-law form over time scales from $\approx$ 1 min to $\approx$ 4 h. We find that the scaling exponent α is virtually identical for records obtained during the first week of daily routine ($\alpha = 0.92 \pm 0.04$, mean $\pm$ standard deviation among subjects), the second week ($\alpha = 0.92 \pm 0.06$) of the daily routine, the constant routine protocol ($\alpha = 0.88 \pm 0.05$), and the forced desynchrony protocol ($\alpha = 0.92 \pm 0.03$). The value of $\alpha \approx 0.9$ for all protocols and all individuals indicates that activity fluctuations are characterized by strong long-range positive correlations, and thus are not

dominated by random factors. Furthermore, we find that this scaling behavior is not caused by the scheduled activities because simulated scheduled activity data that are generated by assigning a specific activity value for each scheduled event throughout the laboratory protocols yields an exponent of $\alpha = 1.5$ (Fig. 3.5a), which represents random-walk type behavior. These results suggest that the activity fluctuations are not a consequence of random events (in which case α would be 0.5) or scheduled events, but rather relate to an underlying mechanism of activity control with stable fractal-like features over a wide range of time scales from minutes to hours. Since mean activity levels and the amplitude of the fluctuations are greatly reduced in the laboratory during the constant routine and forced desynchrony protocols (Fig. 3.1), we obtain smaller values of $F(n)$ (downward shift of the lines in Fig. 3.5a). However there is no change in the scaling exponent α. Similarly, the scaling exponents for the daily routine protocol are independent of the average activity levels of the different subjects (Fig. 3.6a), the mean activity level on different days of the week (Fig. 3.6b), and of the circadian phase, suggesting that this scaling pattern of activity fluctuations appears to be an intrinsic feature.

3.3.4 Nonlinear Fourier phase information

To test for the presence of nonlinear properties of the data, we analyze the "magnitude series" formed by taking the absolute values of the increments between consecutive activity values [26]. Again, from detrended fluctuation analysis of this series, we find practically identical scaling exponents, α_{mag}, for all three protocols, despite large differences in mean activity levels between protocols (Fig. 3.5b). Moreover, all individuals have very similar values of the scaling exponent α_{mag} (Fig. 3.6a), which are not systematically changed by the protocol. For the group, during the first week of daily routine, we find $\alpha_{\mathrm{mag}} = 0.78 \pm 0.06$ (mean $\pm$ standard deviation among subjects), during the second week $\alpha_{\mathrm{mag}} = 0.76 \pm 0.05$, during the constant

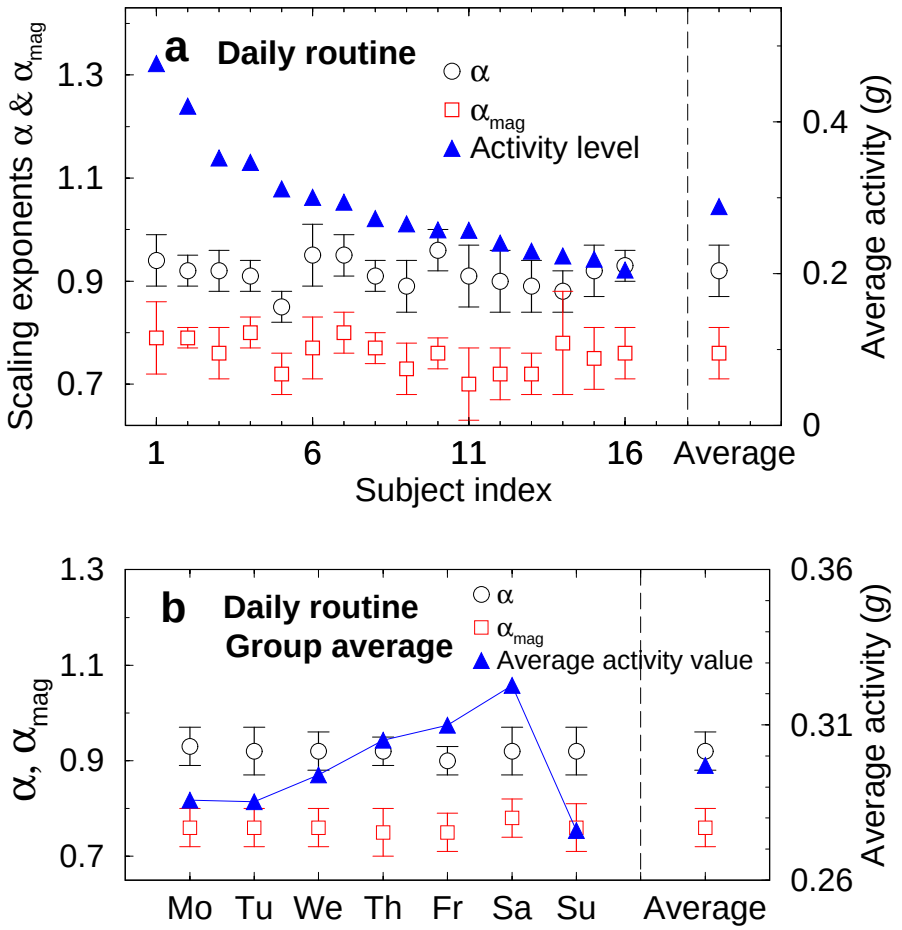

Fig. 3.6. **(a)** Scaling exponents α and $\alpha_{\rm mag}$ (left scale), and average activity levels (right scale) for all 16 subjects obtained from a 14-day daily routine protocol. Although the average activity level between subjects changes considerably (from 0.2 to 0.5), both scaling exponents are consistent for all subjects, exhibiting a group average of $\alpha = 0.92 \pm 0.05$ and $\alpha_{\rm mag} = 0.77 \pm 0.05$. **(b)** Group average scaling exponents α and $\alpha_{\rm mag}$ calculated for different days of the week. While the average activity level progressively increases throughout the week (with a peak on Saturday and a minimum on Sunday), the group average scaling exponents α and $\alpha_{\rm mag}$ remain practically constant, consistent with a robust underlying mechanism of control characterized by fractal and nonlinear features which do not change with activity level.

routine protocol $\alpha_{\rm mag} = 0.82 \pm 0.05$, and during the forced desynchrony protocol $\alpha_{\rm mag} = 0.80 \pm 0.04$. Since $\alpha_{\rm mag} \approx 0.8 (> 0.5)$, there are positive long-range correlations in the magnitude series of activity increments, indicating the existence of

nonlinear properties related to Fourier phase interactions (Fig. 3.5b) [26, 81]. To confirm that the observed positive correlations in the magnitude series indeed represent nonlinear features in the activity data, we do the following test: we generate a surrogate time series by performing a Fourier transform on the activity recording from the same subject during daily routine as in Fig. 3.5a, preserving the Fourier amplitudes but randomizing the phases, and then performing an inverse Fourier transform. This procedure eliminates nonlinearities, preserving only the linear features of the original activity recording such as the power spectrum and correlations. Thus, the new surrogate signal has the same scaling behavior with $\alpha = 0.93$ (Fig. 3.5a) as the original activity recording; however, it exhibits uncorrelated behavior for the magnitude series ($\alpha_{\mathrm{mag}} = 0.5$) (Fig. 3.5b). Our results show that the activity data contains important phase correlations which are canceled in the surrogate signal by the randomization of the Fourier phases, and that these correlations do not exist in the simulated scheduled activity. Further, our tests indicate that these nonlinear features are encoded in Fourier phase, suggesting an intrinsic *nonlinear* mechanism [81]. The similar value of α_{mag} for all three protocols and all individuals, which is different from $\alpha_{mag} = 0.5$ obtained for the simulated scheduled activity and for the phase randomized data, confirms that the intrinsic dynamics possess nonlinear features that are independent of the daily and weekly schedules, reaction to the environment, the average level of activity, and the phase of the circadian pacemaker.

To determine whether or not there is any alteration of the intrinsic patterns for dominant and non-dominant (left and right) hands [98], we record one week of activity data of the left and right hands simultaneously for five additional subjects in the daily protocol. For all subjects, we find that the form of activity distribution (Fig. 3.7a) and the power-law correlations (Fig. 3.7b) are the same for dominant (more active) and non-dominant hands, confirming that the observed intrinsic patterns are independent of activity level.

Finally, to ensure that the power-law correlations are not an artifact produced

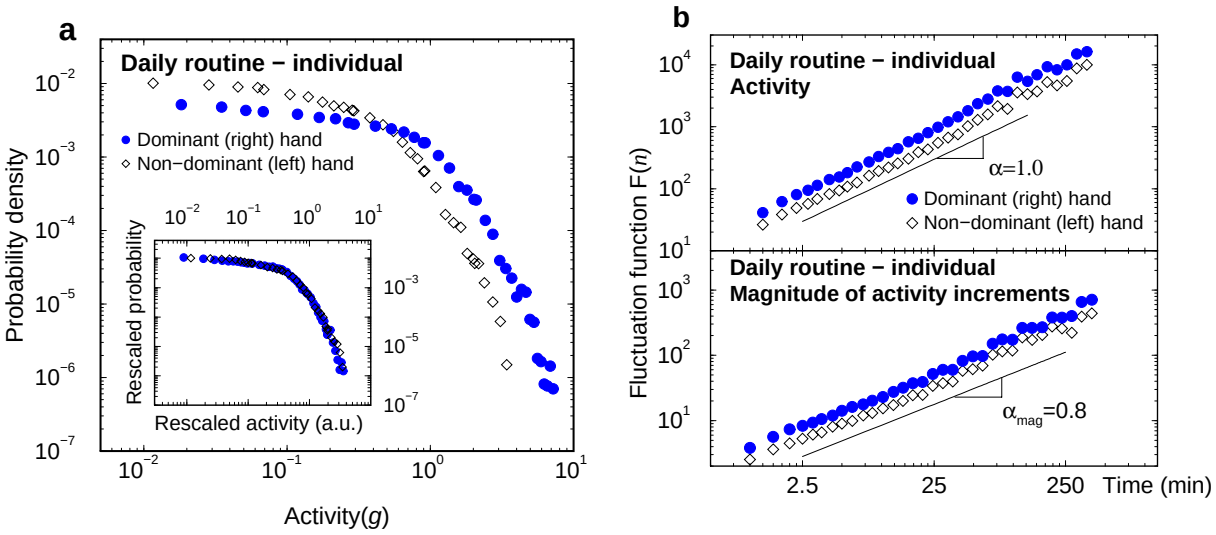

Fig. 3.7. In five additional subjects, we continuously measure both left and right wrist activity levels simultaneously for one week. **(a)** Distributions of left and right wrist activity for a typical subject. The subject is right-handed, and the activity level and variance of the right wrist is larger than that of the left wrist. As a result, compared to the left wrist, the right wrist has a smaller probability at small activity level, and a larger probability at large activity level. After the same rescaling as in Fig. 3.2 (e)-(h), the distributions of the left wrist activity and the right wrist activity collapse onto the same curve. The functional form of this curve is the same as obtained in Fig. 3.2(e)-(h) and Fig. 3.3. **(b)** DFA results of left and right wrist activity fluctuations reveal practically identical power-law correlations — the same value of α. The smaller values of $F(n)$ (vertical shift) for the left wrist are due to the smaller average activity level and variance of the left hand.

by the instrument, we obtain "test" activity data by attaching an *Actiwatch* to a 15 cm radius disk, turning at constant angular velocity of 45 rpm (Fig. 3.8a). The activity values of the *Actiwatch* fluctuate only slightly, and analysis of these random fluctuations reveals scaling exponents $\alpha \approx 0.5$ and $\alpha_{\rm mag} \approx 0.5$ (Fig. 3.8b), which indicate random linear behavior. Thus, the stable values of α and α_{mag} observed in our subjects throughout the varied protocols do not depend on the recording device, but instead these exponents are inherent characteristics of the subjects, and that both hands have the same underlying dynamics of activity regulation.

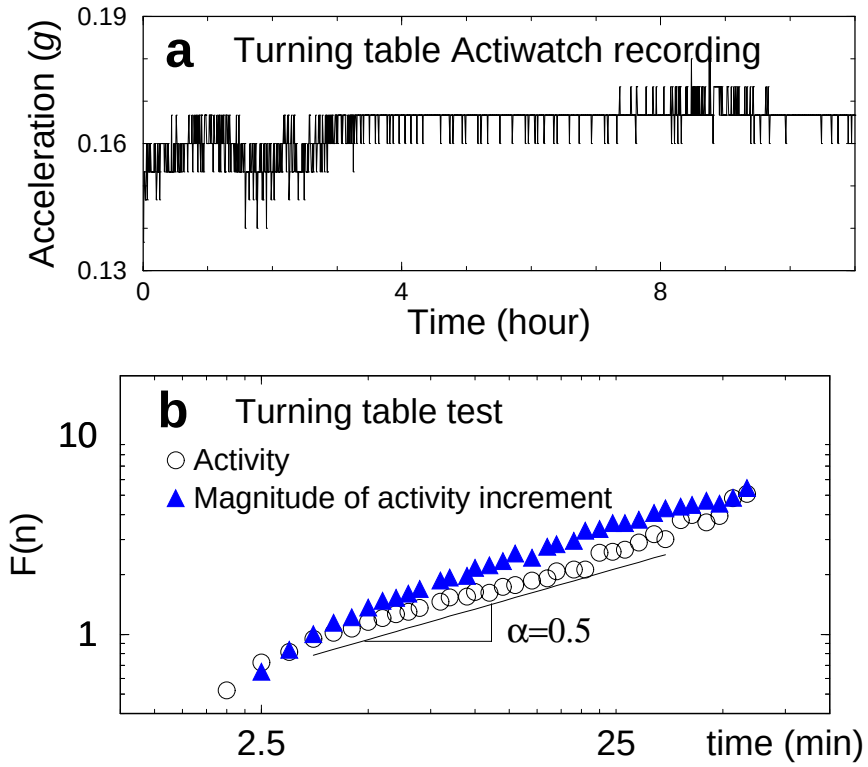

Fig. 3.8. Results suggest the observed scaling features in activity fluctuations are not an artifact of the device. **(a)** Data recorded from an *Actiwatch* placed on a disk rotating with constant angular velocity. **(b)** DFA correlation analysis of the fluctuations in (a) shows random noise behavior, in contrast to the strong positive correlations in activity fluctuations (Figs. 3.5, 3.7).

3.4 Discussion

In summary, the findings reported here offer insights into the mechanisms of human wrist activity control. Prior to our work, it has been a general belief, though never tested, that fluctuations in activity during wakefulness are somewhat random, influenced mainly by extrinsic factors such as reactions to unforeseen random events. Our findings of a stable form for the probability distribution, long-range power-law correlations and nonlinear Fourier-phase features on time scales from seconds to hours, and the consistency of our results among individuals and for different protocols, suggest that there exist previously unrecognized complex dynamic patterns of human

activity that are unrelated to extrinsic factors or to the average level of activity. We also show these scale-invariant patterns to be independent of known intrinsic factors related to the circadian and to any ultradian rhythms. Notably, (i) these patterns are unchanged when obtained at different phases of the circadian pacemaker; (ii) we do not observe systematic intrinsic ultradian rhythms in activity among subjects in the daily routine experiment; (iii) imposing strong extrinsic ultradian rhythms at 4 h and 2 h in the laboratory protocols did not change the fractal scaling exponents α or α_{mag} or the form of the probability distribution; and (iv) we find consistent results over a wide range of time scales. Together, these findings strongly suggest that our results are not a reflection of the basic rest activity cycles or ultradian rhythms. We attribute these novel scale-invariant patterns to a robust *intrinsic multi-scale* mechanism of regulation (Fig. 3.1). Further, our findings suggest that activity control may be based on a multiple-component nonlinear feedback mechanism encompassing coupled neuronal nodes located both in the central and peripheral nervous systems, each acting in a specific range of time scales [99]. This insight provides key elements and guidance for future studies focused on modeling locomotor regulation [100, 101] .

Part IV

Circadian Rhythms

Chapter 4

Circadian Rhythms

4.1 Introduction to this chapter

4.1.1 Effect of circadian factors and day/night changes in behaviors on the pattern of cardiovascular risk

Cardiovascular events are the leading cause of mortality in the United States [103]. These events do not occur randomly across the day. Epidemiological studies demonstrate that myocardial infarction [102, 104–108], stroke [109, 110], angina [108], ven-

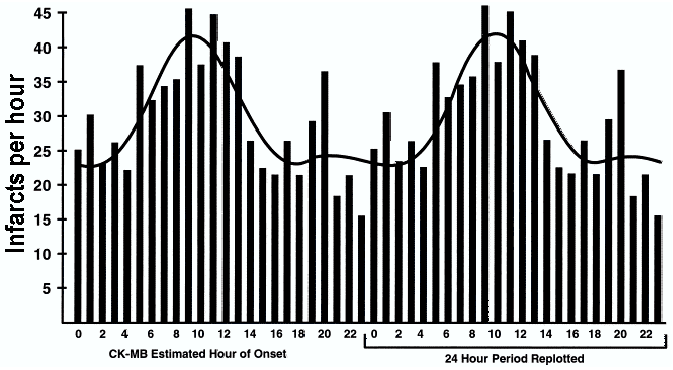

Fig. 4.1. Frequency of myocardial infarctions with a fitted 2-harmonic-regression shows a peak at $\approx 9 - 11$AM [102].

tricular arrhythmias [111] and sudden cardiac death [112–114] have a 24-hour day/night pattern with a primary peak of occurrence around 9:00AM. Such a window of cardiac vulnerability has been hypothesized to be attributable to external factors, e.g., sleep-wake cycles and physical activity, but this hypothesis has not been tested. A potential criticism of the initial epidemiology [102, 115] is that there may have been a degree of reporting bias (i.e. symptoms not reported until morning). A subsequent study assessed the frequency of ventricular tachyarrhythmias in patients with implanted defibrillators [111]. This non-biased measure demonstrated increased tachyarrhythmias at 9AM. A further study objectively ensured that a myocardial infarction occurred in patients presenting with symptoms by measurement of creatinine kinase [116], and confirmed that myocardial infarctions occur 2 to 3 times more frequently in the morning than in the late evening (Figure 4.1.1).

Data from these studies also indicate that sleep or some component associated with sleep (e.g., posture and/or inactivity) has a cardioprotective effect even after correcting for time weighted averages. On the other hand, many researchers have studied the possible behavioral stressors that may be involved in this pattern as they occur at specific times of day, such as arousal from sleep [13, 117], postural changes [118, 119], or exertion [119–123].

In recent years neurophysiologists have begun to determine some of the principal elements involved in orchestrating the sleep-wake and circadian cycles. For instance, the basal forebrain [124, 125], the ventero-lateral [126] preoptic area of hypothalamus, orexin neurones (lateral hypothalamus perifornical area) [127] and the tubero-mamillary nuclei [128] are required for normal sleep-wake regulation and the suprachiasmatic nuclei of the hypothalamus for circadian regulation [129, 130]. To complement these neurophysiological studies, numerous physiological systems have been found to be affected by sleep and/or circadian rhythms [131–136]. Previous studies have established a link between the circadian cycle and basic response functions of the autonomic nervous system [137–141], and recently the intrinsic neural

pathways through which the endogenous circadian pacemaker influences both sympathetic and parasympathetic autonomic output have been discovered [142]. However, the specific mechanisms of interaction between the circadian pacemaker and cardiac neuroautonomic control remain unknown.

4.1.2 Experimental Methods of Assessment of Intrinsic Circadian Factors Versus Behavioral Factors

Surprisingly, the contribution from the internal body clock (circadian pacemaker) to this day/night pattern of cardiovascular events has never been studied with appropriate techniques. We and others, have demonstrated that the human circadian pacemaker (suprachiasmatic nuclei of the hypothalamus) functions to entrain many neurocognitive [132, 143–145], behavioral [146, 147] and physiological [138, 148] systems to the 24-h solar day. To assess circadian rhythmicity two complementary protocols have been developed in Dr. Czeisler's laboratory.

First, a constant routine protocol involves measurements during >24 hours of constant behavioral and environmental conditions [88, 148]. In brief, after 2 adaptation days and nights in the Intensive Physiological Monitoring Suite at Brigham and Women's hospital, subjects awaken and remain in temporal isolation, semi-recumbent (35^o head up), are not allowed out of bed, have restricted movement and have controlled dietary intake for a 40-h period (identical snacks every 2 hours). Room temperature is held at 23 ± 1^oC, light is very low and constant at 3-lux angle of gaze. Thus, changes in physiologic parameters are assessed independent of sleep/wake rhythms, posture changes or exercise. Data are aligned to the endogenous circadian core body temperature (CBT) rhythm such that each measurement is assigned a circadian phase (with the minimum CBT assigned a phase of 0-degrees, usually occurring around 5AM). Using this protocol, our preliminary results are the first to demonstrate intrinsic circadian patterns in cardiac sympathetic and parasym-

pathetic tone independent of changes in posture, activity or sleep/wake state (see Preliminary studies). There was a peak in endogenous circadian sympathetic discharge and a decrease in vagal tone at a biological clock time around 9AM - the period of greatest cardiovascular vulnerability.

The second protocol is the "forced desynchrony" protocol. Over the last 18 years Dr. Czeisler has developed this protocol as a tool to detect distinctions between circadian and sleep/wake cycle related effects on many physiological functions that exhibit a diurnal rhythm including CBT, plasma cortisol, melatonin, alertness and sleep patterns [87, 132]. As one example of the use of this forced desynchrony protocol, Dr. Czeisler's group recently demonstrated that the period of the circadian pacemaker in adult humans is $\approx$ 24.18 hour. This result is substantially different from the 25 hour value that was previously believed to be the circadian period, based on experiments that were confounded by light exposure, which can reset the circadian clock. Such information is necessary to be able to assign a circadian phase to data collected in the proposed study.

Using these protocols, Drs. Czeisler and Shea have shown different circadian, sleep-wake cycle and activity-level related influences on physiological functions such as body temperature, pulmonary mechanics and plasma cortisol [138–141, 148, 149]. The focus of the proposed research is to determine and quantify the degree to which these factors may impact indices of cardiovascular risk in young and older healthy subjects.

4.1.3 Concepts and Approaches from Statistical Physics

We use multivariate data sets collected during these two protocols and under free-running conditions to determine circadian, sleep-wake and activity effects on the mechanisms of cardiac regulation and to extract *static* and *dynamical* markers of cardiac instability. To probe how complex mechanisms of cardiac regulation change

with circadian phase or with sleep-wake transitions and behavioral factors such as variations in activity level, we propose an innovative approach based on concepts and methods derived from statistical physics, fractal theory and non-linear dynamics. The traditional approach considers physiological systems to be governed by the classical principle of homeostasis which postulates that physiological systems return to equilibrium after perturbation and that linear causality controls the pathways of physiological interaction [150–153]. Such classical systems are often characterized by a *single* dominant time scale.

Empirical observations, however, show that even under healthy basal conditions, physiologic systems exhibit noisy fluctuations [154–157] resembling those found in physical dynamical systems away from equilibrium.However, they are traditionally ignored in physiological and clinical studies, which are usually based on averaged data. Do such "nonequilibrium" fluctuations simply reflect the fact that physiologic systems are being constantly perturbed by external and intrinsic noise? Or, do they contain useful, "hidden" information about the underlying nonequilibrium control mechanisms?

4.2 Circadian effect on heart dynamics

4.2.1 Static properties

As a first step we have investigated how static characteristics such as the average interbeat interval and the standard deviation change with circadian phase. We have analyzed continuous heartbeat recording from 5 healthy subjects during six 28-hour cycles of forced desynchrony routine (See Appendix .6). Data were divided in segments of one hour, and the average interbeat interval and standard deviation were calculated for each segment. One plausible hypothesis is that the average heart rate and standard deviation will only change with sleep or wake phase, being lower during

sleep. Surprisingly, we find that the average interbeat interval and the standard deviation exhibit strong circadian rhythm independent of sleep or wake phase (Fig. 4.2). Further, we find that static characteristics are significantly higher in the interval 260 - 360 degrees circadian phase (which corresponds to 2-4AM the traditional sleep phase) with a maximum at ≈ 0 circadian degree when the body temperature is lowest. Our findings suggest the existence of an endogenous circadian rhythm which alters the heartbeat according to inherent "memory" of the traditional sleep opportunity when heart rate is lower and the probability for large interbeat fluctuations is higher.

Such circadian mediated decrease of the average heart rate coupled with increase

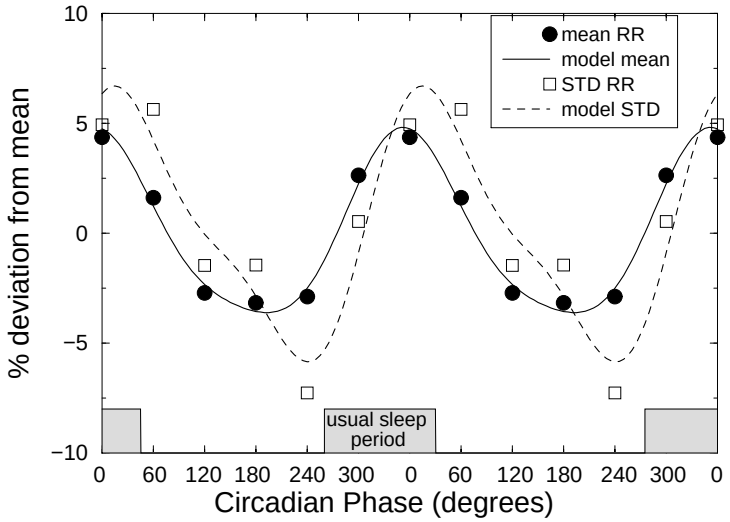

Fig. 4.2. Endogenous circadian variations in the average and the standard deviation of RR intervals. Group average of 5 subjects' data collected throughout a 10 day forced desynchrony protocol in dim light, in which subjects' sleep/wake cycles were adjusted to 6 consecutive 28 hour periods. Dark bars represent the usual sleep period. Data are double plotted to enhance visualizations of rhythms. Cosinor analysis fits are shown as lines with regression coefficient of $R^2 = 0.8$ for the RR interval data points and $R^2 = 0.6$ for the standard deviation. Note, there exist significant circadian variations in the average in RR interval (Student t-test $p = 3.62 \times 10^{-10}$) and standard deviation (Student t-test $p = 6.25 \times 10^{-5}$) with the peak occurring during the usual sleep periods.

of the standard deviation (larger amplitude of interbeat fluctuations) between 2-4AM suggests reduced sympatho-vagal balance which may be cardio-protective.

4.2.2 Dynamic properties

4.2.2.1 Long-range correlations

Previous studies have found the presence of scale-invariant behavior characterized by *long-range power-law correlations* in the fluctuations of heartbeat intervals over multiple time scales [13, 19, 56]. Such a scaling behavior indicates the presence of a self-similar (fractal) hierarchical organization in the seemingly "erratic" heartbeat fluctuations, even when data was recorded under free-running conditions. Further studies have also observed significant *alterations* of the long-range correlation properties with disease and with sleep-wake transitions (as quantified by different values of the scaling exponent α, Sec. 1). These findings raise the intriguing possibility that changes in the mechanism of control associated with behavioral sleep-wake transition may be responsible for the increased cardiac instability observed in particular circadian phases [13, 83].

An additional hypothesis is that there is a circadian clock, independent of the sleep-wake cycle, which affects the cardiac dynamics. Previous studies of the B&W group show different levels of sympathetic and parasympathetic tone during *short-term* response to extrinsic stimulation at different circadian phases [141]. We test whether the *long-term* mechanism of cardiac control changes with circadian phase, and how such change may account for the 9-11am window of cardiac instability. To this end, we investigated whether the scaling behavior of the heartbeat fluctuations, which probes the dynamics over a broad range of time scales, changes when healthy subjects sleep at different circadian phases. Since the scaling exponent we found for healthy subjects during sleep is lower than for subjects with congestive heart failure [13], an increase in the value of the scaling exponent during sleep would indicate

cardiac instability mediated by the circadian rhythm. On the other hand, if the scaling exponent remains the same throughout different circadian phases, this would indicate no circadian influence during sleep on the long-term multiscale mechanisms of cardiac regulation.

As a first step, we analysed continuous recordings from 5 healthy subjects during 7 cycles of forced desynchrony routine wherein subjects' sleep-wake cycles are adjusted to 28 hours so that their behaviors occur across all circadian phases. Heartbeat data were divided into one-hour segments. For each segment, we estimated the scaling exponent using the DFA method, thus probing the correlation properties in the heartbeat fluctuations at different circadian phase. Since the sleep and wake contributions are equally weighted, a change of the values of the scaling exponent α with circadian phase would suggest a circadian rhythm. Our results show a

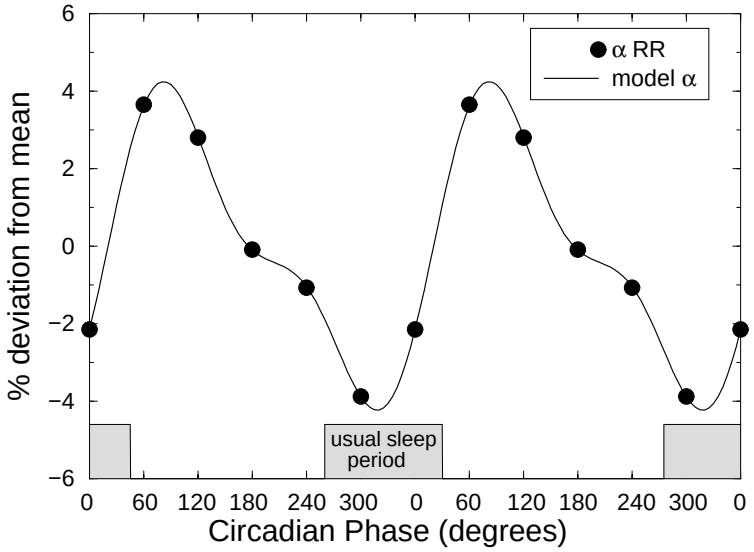

Fig. 4.3. Significant change of the correlation exponent as function of circadian phase with a pronounced peak at 60 circadian degrees ($\approx 9-10$ AM) indicates relative loss of control (closer to "random-walk" type fluctuations) and increased cardiac risk. We note that an increased value of α is observed for subjects with congestive heart failure. The data are shown as symbols, and cosinor analysis fits are shown as a line.

strong circadian-mediated alteration in the correlations characterized by a significant change (Student test p-value 6.25×10^{-5}) in the value of the exponent α (Fig. 4.3). Remarkably, the peak of this circadian variation is centered at 60 degrees, coinciding with the 9-11am window of cardiac risk [102, 115, 158, 159].

We note that an increase in the value of the correlation exponent α has been also observed under specific perturbations and pathologic conditions such as heart failure, suggesting alteration and loss of cardiac control. Thus our preliminary findings indicate that circadian influences could be responsible for cardiac risk. This risk appears to be mediated through changes in the endogenuous mechanism of cardiac neuroautonomic regulation since it is accompanied with loss of scale-invariant temporal structure in heart rate variability. Recent reports [142] of separate neuronal links between the intrinsic circadian pacemaker (suprachiasmatic nucleus) and the pre-sympathetic and pre-parasympathetic neurons corroborate our hypothesis of mechanistic action between the circadian clock and the neuroautonomic regulation of the heart. Further, risk for cardiac instability may be even higher for subjects with pathologic conditions, where circadian effects may contribute to already existing perturbations in cardiac neuroautonomic control.

4.2.2.2 Nonlinear features

Studies show that the magnitude of the heartbeat interval increments $|\Delta RR|$ exhibits power-law scaling behavior and is *positively* correlated ($\alpha_{mag} \approx 0.75 > 0.5$, [26], unlike the original heartbeat increment time series ΔRR that is anticorrelated ($\alpha \approx 0$) [13, 19]. Positive correlations in the magnitude series indicate that an increment with a large magnitude is more likely to be followed by an increment with a large magnitude. Recent studies also established that the magnitude series relates to the *nonlinear* properties of the original time series, and that the value of the scaling exponent characterizing the correlations in the magnitude series is related to the width of the multifractal spectrum [81, 82, 164]. For patients with congestive heart

failure, we observed a significant decrease in the short-range scaling exponent, which may be related to perturbed vagal control affecting relatively high frequency fluctuations. The simultaneous decrease observed for the long-range scaling exponent α_{mag} with heart failure indicates weaker correlations and loss of nonlinearity that may be related to impaired feedback mechanisms of neurohormonal cardiac regulation [26].

Since loss of nonlinearity is related to impaired mechanism of cardiac regulation [26, 165], oscillations of nonlinear markers with circadian phase would suggest time windows of cardiac instability. Next we employ detrended fluctuation analysis (See Chapter .1) to quantify the correlations in magnitude of heartbeat increment at different circadian phases during sleep state. Our analysis shows that indeed a circadian rhythm exists in cardiac dynamics during sleep. While previous studies

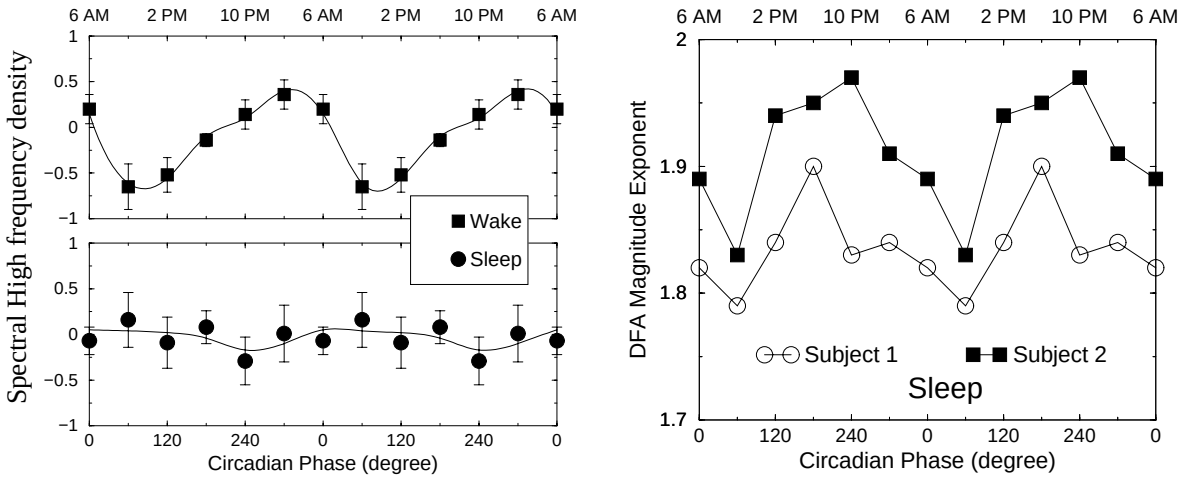

Fig. 4.4. (**Left**) Previous work shows that there is a circadian rhythm in the high frequency component (very short time scale) of the power spectrum of heart rate variability while wake, yet there is no detectable circadian rhythm during sleep. (**Right**) In contrast, the magnitude and sign approach is sensitive enough to detect circadian rhythms in the dynamics of cardiac system during sleep. Figure shows the magnitude scaling exponent α_{mag} across circadian phase for 2 young and healthy individuals measured during sleep. This graph illustrates that both of these individuals have a minimum value of the scaling exponent characterizing the magnitude of heart rate fluctuations at 60-degree, which is 9-11AM.

based on standard linear measures such as the power-spectrum analysis were not able to detect circadian rhythms, our nonlinear magnitude and sign method reveals a clear circadian pattern (Fig. 4.2.2.2). In particular, we find that the magnitude of heartbeat fluctuations during sleep is characterized by a lower value of the scaling exponent at a 60-degree circadian phase (9-11AM), and by a higher exponent at 180 - 240 degrees (6-10PM). A decrease in the magnitude exponent (obtained from the magnitude of the heart rate fluctuation) in the time window around 9-11AM indicates a period of cardiac vulnerability.

4.3 Circadian effect on human motor activity

It is a general belief that the circadian pacemaker influences human activity. However, it is not clear that the circadian pacemaker affect through its interaction with sleep/wake cycle or has direct and independent influences on human activity. The answer to this question will further help to demonstrate that circadian pacemaker has independent influences on cardiac dynamics, rather than affect through mediating the activity level. To this end,we analyze the activity data recorded in the forced desynchrony protocol (Appendix .6) to investigate statistical properties at different circadian phases. We use body temperature as a circadian phase marker (see Appendix .6) [96, 160].

4.3.1 Static properties

When examining static characteristics such as the mean activity level and standard deviation, we uncovered a significant circadian rhythm (Fig. 4.3.1a). This rhythm is characterized by broad peaks for the average activity level and the standard deviation of activity fluctuations at 160-240 circadian degrees corresponding to afternoon hours. The very gradual increase of these two static characteristics in the morning

hours does not support the hypothesis of circadian mediated influence of activity on cardiac vulnerability in the time window 9-11am.

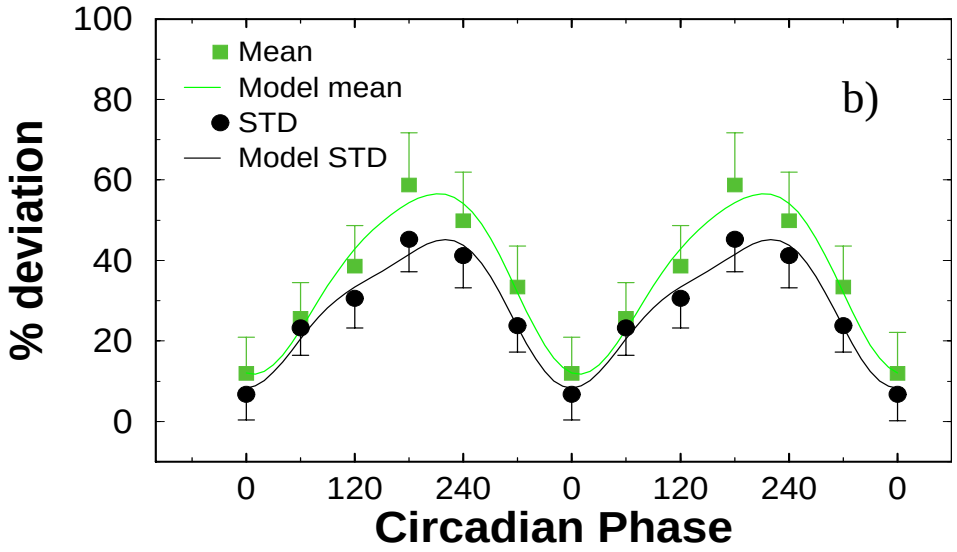

Fig. 4.5. Zero degrees are equivalent to the core body temperature minima. Group average 6 subjects' data collected throughout a 8 day forced desynchrony protocol in which the sleep-wake cycles were adjusted to 28-hour periods. Mean level and standard deviation during wakefulness at different circadian phase. P-test gives $p = 0.0006$ for mean level and $p = 0.00009$ for standard deviation, indicating highly significant circadian influences on mean and standard deviation of activity during wakefulness with peaks in the afternoon hours.

4.3.2 Dynamic properties

To provide further insight into cardiac influences on the dynamic control, we next examined the temporal organization in the fluctuations of activity values at different circadian phases. We performed DFA analysis (i) on activity signals to quantify the long-range power-law correlations (See Chapter 3.3.3), and (ii) on the magnitude series of activity increments to probe the nonlinear features related to Fourier phase interactions (See Chapter 3.3.4). Our results show that the scaling and nonlinear features in the temporal organization of activity fluctuations (Chapter 3.3.3) does

not change with circadian phase (Fig 4.3.2a, b).

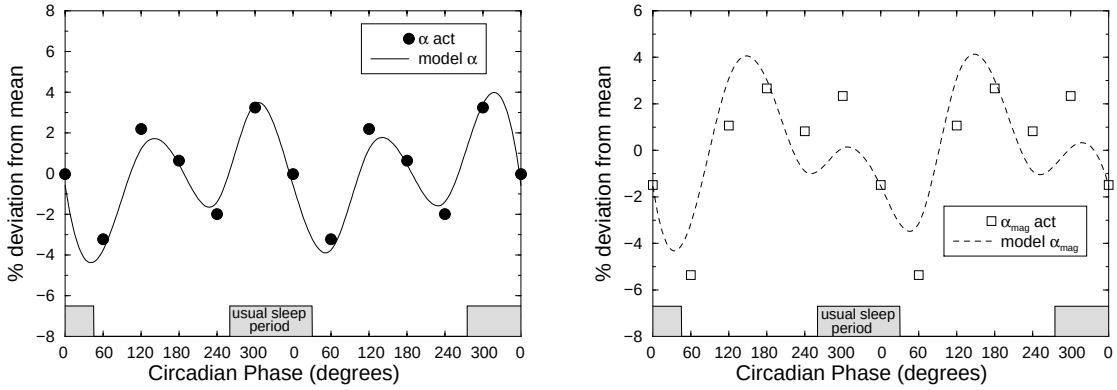

Fig. 4.6. **(a)** Group averaged deviation of α from its mean value, basing on the DFA analysis. **(b)** Group average deviation of α_{mag} from its mean value basing on the magnitude analysis. P-test gives $p > 0.01$ for α, and $p = 0.04$ for α_{mag} obtained from the magnitude analysis, indicating no significant circadian influence on the scaling and nonlinear features of wrist activity (Figs. 3.5).

4.4 Discussion

Our analyses show that there is a complex robust structure embedded in physiologic fluctuations which remain invariant when data are probed over a broad range of time scales. In heartbeat dynamics, such scale-invariant behavior relates to the underlying neuroautonomic control mechanism, since key fractal and nonlinear features appear to be independent of activity level (daily or constant routine) but change with sympathetic or parasympathetic blockade and under pathologic conditions. Further, our preliminary observations show that these scaling features change with sleep-wake transitions, and are influenced by an endogenous circadian rhythm when decoupled from the sleep-wake cycle. Remarkably, we found that the circadian influence at 9-11AM, corresponding to the epidemiologically demonstrated time window of cardiac vulnerability, is associated with loss of long-range correlation and loss of nonlinearity

in cardiac dynamics — features observed also under certain pathologies (e.g., congestive heart failure). Thus, our preliminary results suggest that the endogenous circadian pacemaker may be related to cardiac risk.

Part V

Cerebral Control Mechanism

Chapter 5

Synchronization Patterns in Cerebral Blood Flow and Peripheral Blood Pressure under Minor Stroke

5.1 Overview

Stroke is a leading cause of death and disability in the United States. The autoregulation of cerebral blood flow that adapts to changes in systemic blood pressure is impaired after stroke. We investigate blood flow velocities (BFV) from right and left middle cerebral arteries (MCA) and beat-to-beat blood pressure (BP) simultaneously measured from the finger, in 13 stroke and 11 healthy subjects using the mean value statistics and phase synchronization method. We find an increase in the vascular resistance and a much stronger cross-correlation with a time lag up to 20 seconds with the instantaneous phase increment of the BFV and BP signals for the subjects with stroke compared to healthy subjects [166].

5.2 Introduction to this chapter

Stroke is a leading cause of death and disability in people above certain age[167], yet many factors that set the stage for stroke and determine the outcome after stroke are not well understood.

Cerebral autoregulation involves several complex mechanisms maintaining steady blood flow to the brain in the presence of systemic blood pressure fluctuations. These mechanisms are impaired after an acute stroke and cerebral blood flow becomes dependent on blood pressure[168, 169]. Therefore, cerebral blood flow declines with falling blood pressure (which may lead to ischemia) and increases with rising blood pressure (which poses a risk of hemorrhage). Activities of daily living, such as rest and exercise, sitting and standing-up, even taking meals are associated with blood pressure fluctuations on a range of time scales. For example, standing-up may induce transient hypotension, which requires rapid cerebral vasodilatation to compensate for blood pressure decline and to maintain cerebral perfusion in the upright position[170]. This complex mechanisms of cerebral regulation is still not well understood. It is also not clear if cerebral autoregulation recovers after stroke[171]. Previous studies suggest that cerebral blood flow declines on the stroke side during orthostatic stress, posing a risk of reduced perfusion to the affected side of the brain[172].

Here we study the effects of stroke on cerebral autoregulation controlling the flow-pressure relationship. Our goal is to determine the effects of orthostatic stress on the dynamic relationship between blood flow velocities (BFV) in the middle cerebral arteries and the peripheral blood pressure (BP) from healthy subjects and patients with stroke. We find that the dynamics of flow-pressure regulation is impaired after a stroke and we determine indices allowing us to characterize and quantitate healthy cerebral autoregulation and its impairment after stroke.

5.3 Experimental design and data acquisition

5.3.1 Study groups

In our study we have:

- 13 patients (six male, seven female) with documented chronic ischemic minor stroke on MRI or CT (age 52.5 ± 7.3 years);
- 11 healthy subjects (age 47.2 ± 8.5 years).

5.3.2 Experimental protocol

All subjects participated in the following experimental protocol:

- Supine: subject rests in supine position for five minutes on the tilt table;
- Tilt: the table is moved upright to an 80 degree angle and the subject is in an upright position for five minutes;
- (Tilt) Hyperventilation: subject is asked to breathe quickly at approximately 1 Hz frequency for three minutes in an upright position. Hyperventilation induces hypocapnia (reduced carbon dioxide), which is associated with vasoconstriction;
- (Tilt) CO2-rebreathing: The subject is asked to inhale deeply and hold the breath for one minute, then breathe a mixture of air and 5% CO_2 from rebreathing circuit at a comfortable frequency for three minutes in an upright position. CO_2 rebreathing increases carbon dioxide above normal levels and induces hypercapnia, which is associated with vasodilatation.

5.3.3 Data acquisition

Blood flow velocity (BFV):

*Transcranial Doppler*ultrasonography system (MultiDop X4, Neuroscan, Inc.) is used for monitoring BFV in both MCAs. The right and left MCA is insonated from the temporal windows by placing the 2-MHz probe in the temporal area above the zygomatic arch. Each probe is positioned to record the maximal BFV and fixed at a desired angle using a three-dimensional positioning system attached to the light-metal probe holder. Special attention is given to stabilize the probes, since their steady position is crucial for continuous BFV recordings. Data are visually inspected and occasional extrasystoles and outlying values are removed using linear interpolation. A Fourier transform of the Doppler shift [a difference between the frequency of the emitted signal and its echo (frequency of reflected signal)] is used to calculate BFV. Systolic, diastolic, and mean BFV are detected from the envelope of MCA waveforms. A recent MRI study suggests that MCA diameter does not change during hyperventilation and breath-holding[173].

Blood pressure (BP):

Beat-to-beat BP is recorded from the finger with a Finapres device (Ohmeda Monitoring Systems, Englewood CO). With the finger positioned at the heart level and the temperature kept constant, this device can reliably track BP changes over a prolonged period of time[174].

BFV and BP signals are recorded simultaneously and the signal sampling frequency is 50 Hz.

5.4 Data

We first investigate the shape of BFV and BP signals for both healthy and stroke group during four experimental stages. The BFV waveform changes during vaso-

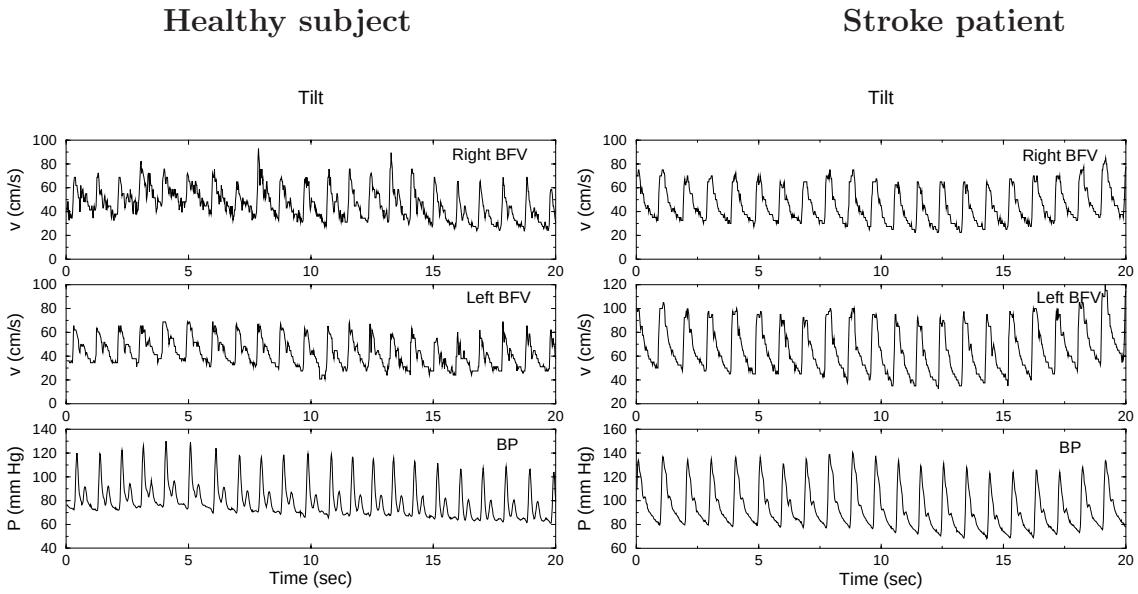

Fig. 5.1. Right BFV, left BFV, and BP signals during tilt stage: (Left) One healthy subject; (Right) One subject with stroke located in the right brain hemisphere. BFV and BP signals have a similar shape and both are periodic signals with a period of around one second, which reflects flow and pressure waveform during each heart beat. Data from the stroke patient exhibit larger amplitude for the BFV signals and less pronounced second notch in the BP waveform.

constriction and vasodilation and therefore, we presume to be able to identify the subjects with impaired autoregulation.

In Fig. 5.1, we show examples of BFV signals from right and left MCA as well as BP signals from the finger during the tilt stage for one healthy subject and one stroke subject. For both subjects, right and left BFV signals and BP signals display a periodic behavior with a period of around one second, corresponding to heart frequency. Furthermore, for each subject, the shape of two BFV signals and one BP signal all look similar (especially for two BFV signals): a rapid increment of signals at the beginning of each circle and then a slow recovery in the rest of each circle. We also find some differences in the shape of three signals between the two subjects shown in Fig. 5.1, however, we fail to find any group differences in the shape of signals

for the group of 13 stroke subjects and the group of 11 healthy subjects. Therefore, such differences seem to be reflecting only trivial individual variability for different subjects. In summary, the shape of signals is not a good marker for distinguishing stroke patients from healthy people.

In the next section, time domain analysis and synchronization techniques will be applied to each subject to characterize two BFV signals and one BP signal.

5.5 Results

5.5.1 Time domain

Several quantities have been used to quantify the properties of BFV and BP signals and the possible relations between them. For example, we have measured the magnitude of fluctuation (i.e., standard deviation) of BFV and BP signals for all subjects. From Fig. 5.1, one may infer that the signals for stroke patients have a larger standard deviation, and the BFV signals on the stroke side (e.g., right or left side in the brain) have a slightly smaller standard deviation compared to the normal side. However, in any of the four stages, we did not find any group differences for the standard deviation between these two groups. The different standard deviation between subjects seems to be more an indication of the individual variabilities in each subject than the indication of disease.

Instead, we find that the mean of signals in the tilt stage is a good quantity for determining the differences between healthy and stroke groups. As shown in Fig. 5.2, we find that in the tilt stage, most stroke patients have relatively lower BFV in MCA. More interesting, the exceptions, e.g., the 1st, 2nd, 4th, and the last stroke patients in Fig. 5.2, are all female patients. Therefore, the mean of signals during tilt is a good marker for male stroke patients, but only a fair marker for female stroke patients. However, the relationship between the stroke type, size and location and

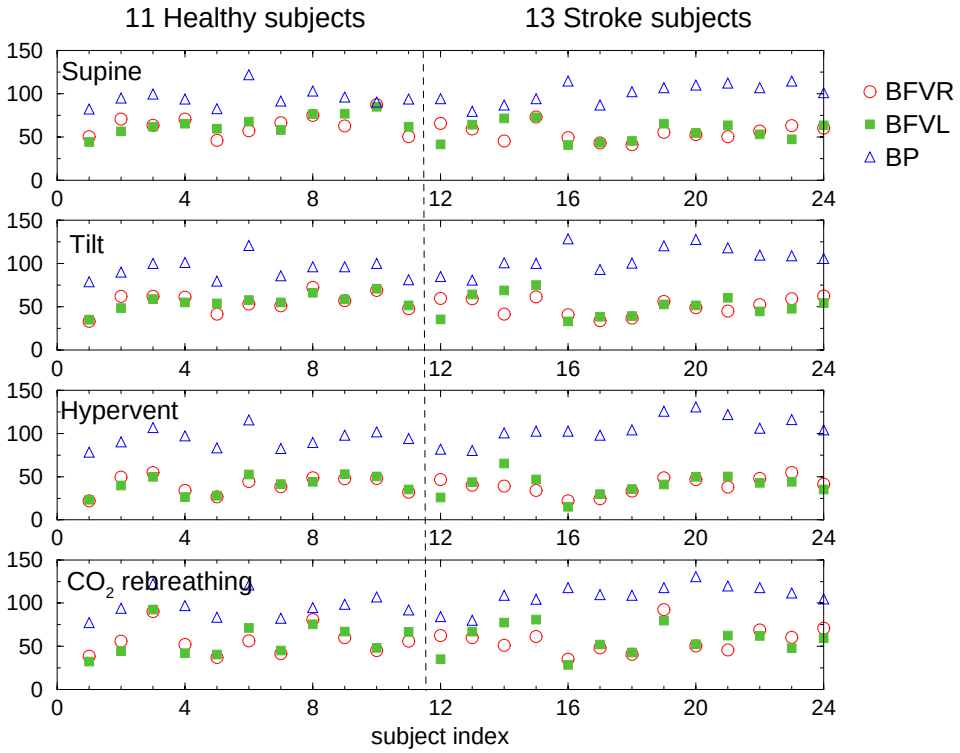

Fig. 5.2. Mean values of BFV and BP signals during four experimental stages for all 24 subjects in our database. The x axis indicates the subject index, healthy subjects are to the left of vertical dash line and stroke patients are to the right. We find that in the tilt stage most stroke patients have relatively lower BFV. Note that increased relative difference between the BFV and BP mean values for the stroke patients compared to healthy subjects.

co-morbidities (e.g., hypertension) needs to be examined before conclusions can be made about this gender effect.

Based on the results shown in Fig. 5.2, we further calculated the BP/BFV ratio of the mean of signals for all subjects (see Fig. 5.3). In medical science, this ratio is often called the vascular resistance — a parameter quantifying the elasticity of the arteries. Our results suggest that the vascular resistance is increased after stroke. Vascular resistance seems to provide a better quantitative distinction between healthy subjects and stroke subjects than that from the mean of signals. As shown in Fig. 5.3, we find

that during tilt, the ratios of most healthy subjects are below the ratio = 2 line, while most the stroke patients ratios are above the ratio = 2 line. These results suggest that stroke is associated with increased cerebrovascular resistance. Similar findings are also observed in supine position, but the variability of inter-subjects observations is also greater compared to the tilt. Vascular resistance during hyperventilation and CO_2 rebreathing is similar between groups.

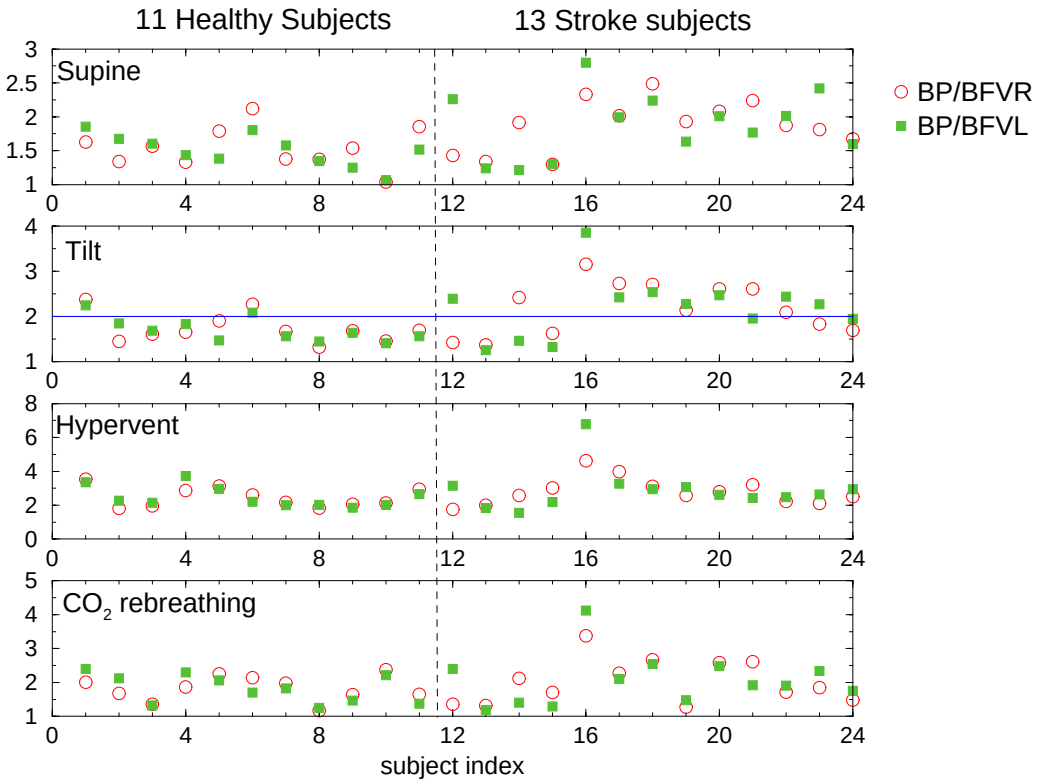

Fig. 5.3. The ratio of the BFV and BP mean values (i.e., vascular resistance) during four stages for all 24 subjects in our database. Note that during tilt, this ratio for most healthy subjects is below two (solid horizontal line), while most stroke patients exhibit a ratio above two. Similar increase in the vascular resistance is also observed in supine position.

Our results, in some sense, suggest that cerebral autoregulation has been impaired for chronic stroke patients. In healthy subjects, peripheral vascular resistance is

increased with an upright position, but cerebral vascular resistance is not changed, due to autoregulation. With impaired autoregulation after stroke, cerebral vessels react in a manner similar to the peripheral vessels and vascular resistance is increased, which may result in reduced perfusion during orthostatic stress.

5.5.2 Synchronization technique

5.5.2.1 Theoretical background

Our Synchronization algorithm is based on the Hilbert Transform. The Hilbert Transform of any signal $f(x)$ is defined as the following:

$$F(y) = \frac{1}{\pi}(\text{Cauchy Principal Value}) \int_{-\infty}^{\infty} \frac{f(x)}{x-y} dx. \tag{5.1}$$

$F(y)$ has an apparent physical meaning in Fourier space: for any positive (negative) frequency ω, the Fourier component of $F(y)$ at ω is that of $f(x)$ at ω after a 90° clockwise (anti-clockwise) rotation in the complex number plane. For example, if the original signal is $\sin\alpha x$ ($\alpha > 0$), its Hilbert Transform will become $\cos\alpha y$.

Similar to the way we construct complex numbers, for any time series $s(t)$ we can always construct its "analytic signal" [175–179], which is defined as

$$s(t) + i\tilde{s}(t) = A(t)e^{i\phi(t)}, \tag{5.2}$$

where $\tilde{s}(t)$ is the Hilbert Transform of $s(t)$. $A(t)$ and $\phi(t)$ are the Hilbert amplitude and phase of $s(t)$, respectively. Both the Hilbert amplitude and phase provide instantaneous attributes of a time series $s(t)$.

For a pure sinusoid, the Hilbert amplitude is constant and the Hilbert phase is a straight line over time. For more complex signals, both the Hilbert amplitude and phase may display complicated forms. As shown in Fig. 5.4, the Hilbert amplitude of the left BFV for a healthy subject has a similar periodic behavior to that of the original signal, in all four experimental stages. The Hilbert phase of the left

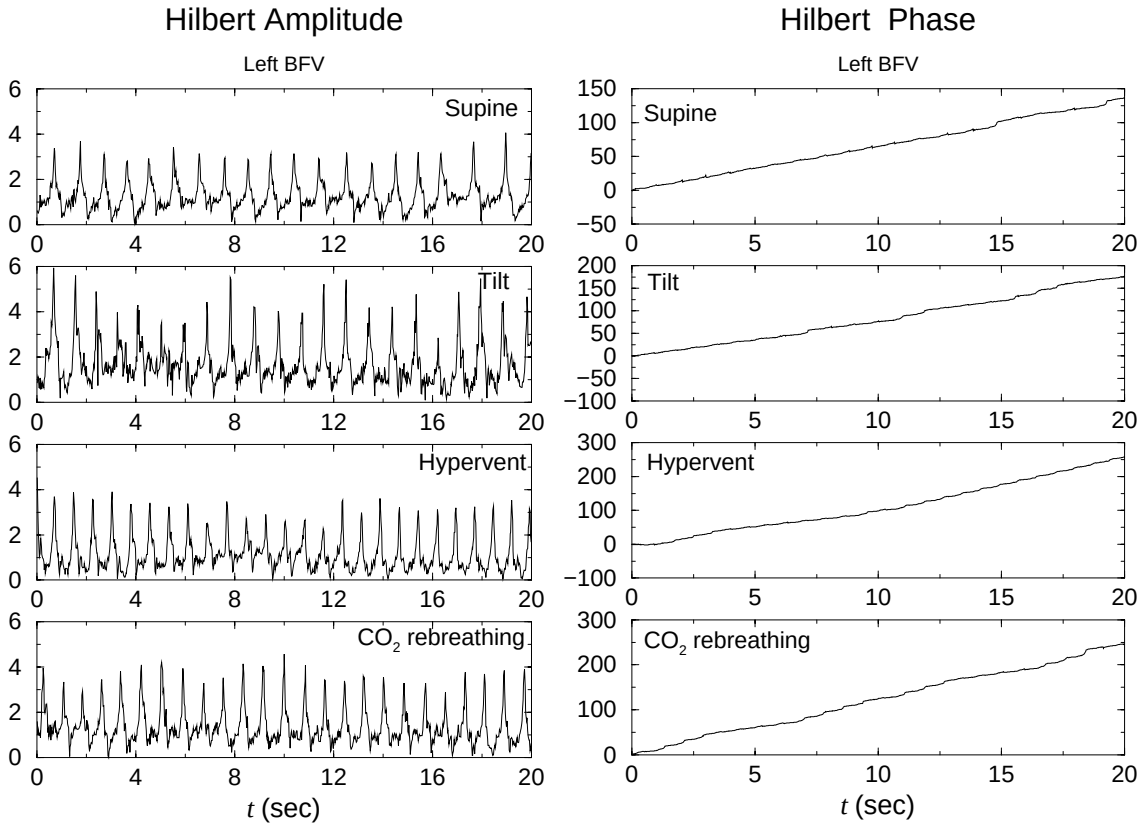

Fig. 5.4. Instantaneous Hilbert amplitude (left) and Hilbert phase (right) of a filtered BFV signal from the left brain hemisphere (the filter is described in section 5.5.2.2) for a healthy subject, during four experimental stages. The Hilbert phase exhibits complex fluctuations along strong linear trends. Simultaneous increase or decrease of the phase of the BFV and BP signals is an indication of synchronization behavior (see Fig. 5.4).

BFV of that subject during all four experimental stages can be looked upon as the superposition of a linear trend and additional fluctuations: the linear trend is trivial since it is caused by a periodic heart rate at a frequency of around 1 Hz; fluctuations are more important for us since they contain other useful information.

In practice, some filtering techniques are often needed before we calculate the Hilbert Transform of a time series. Actually, the value of analytic signals in Eqn. (5.2) can depend on the mean of $s(t)$, i.e., $s(t)$ and $s(t) + a$ (a is a constant) may have

different Hilbert amplitude and phase, though both original signals have almost identical statistical properties. A simple way that may eliminate this effect is to subtract the mean of a time series before we calculate the Hilbert amplitude and phase. Due to similar reasons, the application of our algorithm on nonstationary signals is also limited, since the mean of a nonstationary signal is changing over time. To analyze a nonstationary signal, we often need to apply a Fourier high frequency pass filter first to remove the effect of the mean and slow drift of local mean in the signal before we calculate the Hilbert amplitude and phase.

5.5.2.2 Procedure

Our synchronization technique includes the following steps:

- First, we filter out low frequency trends in signals (high f pass filter $f > 0.05$ Hz is applied) and then normalize signals (let the standard deviation of signals $\sigma = 1$);
- Next, we calculate the Hilbert amplitude and phase of filtered signals;
- Last, we calculate the cross-correlation between the BFV and BP signals for both Hilbert amplitude and phase. Note that cross-correlation method will fail if original signals contain linear trends (trends will contribute to the results, but we are not interested in the effect of trends). To eliminate the linear trend in the Hilbert phase (see Fig. 5.4), we instead calculate the cross-correlation of the Hilbert phase increment of the BFV and BP signals.

5.5.2.3 Results

The technique described in Section 5.5.2.2 has been applied to all 13 stroke patients and 11 healthy subjects. We find that, for the cross-correlation of both the Hilbert amplitude and the phase increment of BFV and BP signals, stroke patients display

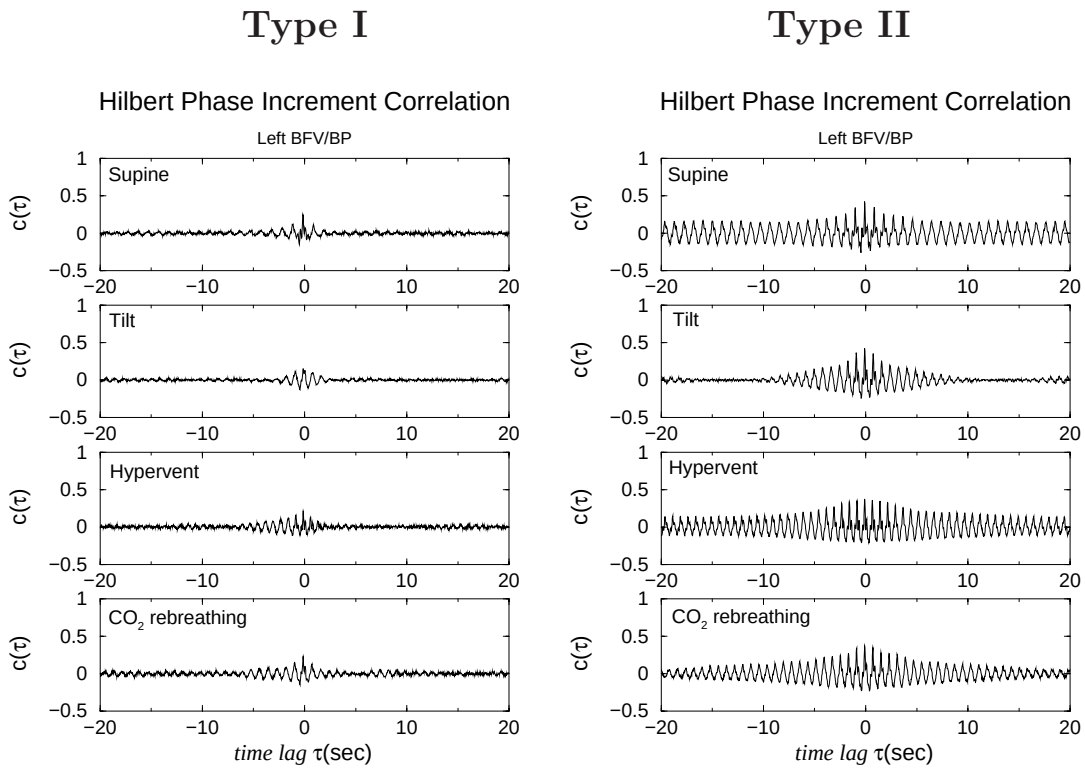

Fig. 5.5. Cross-correlation function of the Hilbert phase increment for the BFV and BP signals during four experimental stages. We find that all 24 subjects separate into two categories which exhibit two very distinct types of behavior. **Type I** (Left): low-amplitude cross-correlations which decay at lags $\approx$ 5sec., during all four stages. Most healthy subjects (eight out of eleven) belong to this type. **Type II** (Right): high-amplitude cross-correlations for lags up to 20 seconds, suggesting strong synchronization. Most stroke patients (eleven out of thirteen) belong to this type. We find that the stage where the best distinction from Type I correlations is given varies for different subjects.

different behavior from that of healthy subjects. Furthermore, cross-correlation of the Hilbert phase increment often gives better results. In general, the cross-correlation results have the following two types:

- **Type I**: As shown in the left figure of Fig. 5.5, the BFV and BP signals have shorter correlation (less than 10 seconds). Most healthy subjects (eight out of eleven) and a few stroke patients (two out of thirteen) belong to this type. The

stroke patients who belong to this type are both female;

- **Type II**: As shown in the right figure of Fig. 5.5, the BFV and BP signals have much longer sustained correlation (larger than 10 seconds). Most stroke patients (eleven out of thirteen) and a few healthy subjects (three out of eleven) belong to this type. The stage where the best distinction from **Type I** correlation is given varies for different subjects.

The short Type I correlations (less than 10 seconds) can usually be attributed to the effect of heart rate and/or respiration — i.e., it reflects the effect of other body regulations (similar to a kind of "background noise") on both BFV and BP signals and is beyond our interest. The longer Type II correlation, however, cannot be attributed to the effect of other regulations, instead, it may really reflect the functions of vascular tone. In other words, it may describe the true correlations between the BFV signals in MCA and peripheral BP signals. Therefore, the existence of such Type II correlations may indicate impaired cerebral autoregulation for those subjects.

5.6 Conclusions

In our study we investigate blood flow velocity (BFV) signals measured from the right and left middle cerebral arteries (MCA) and peripheral blood pressure signals, from 11 healthy subjects and 13 subjects with documented minor stroke. We compare the properties of BFV and BP signals as well as synchronizations between BFV and BP signals for both groups. Based on our special experimental protocol, we evaluate the effect of minor chronic stroke on cerebral autoregulation and the effect of orthostatic stress on the relations between BFV and BP signals in the healthy subject and the stroke patient.

In time domain, we find that the standard deviation of BFV and BP signals during different stages is similar for healthy subjects and stroke patients. However, we

find that healthy subjects and stroke patients have different responses to orthostatic stress, reflected by the mean BFV and BP values, as well as by the vascular resistance (mean BP/mean BFV ratio). We find that cerebral vascular resistance is increased in subjects with stroke, which suggests impaired autoregulation.

We also apply the synchronization method (based on the Hilbert transform) to quantify the possible phase relations between the BFV and BP signals. We find that the cross-correlations between the Hilbert phase increment of the BFV and BP signals provide reliable quantitative indices that clearly distinguish stroke patients from healthy subjects, even when the stroke is minor — a condition which is typically difficult to diagnose. These indices for stroke patients show a strong and sustained correlation between BFV and BP signals, which cannot be explained by heart rate and/or respiration. Such synchronization pattern is not apparent in healthy subjects and suggests impaired cerebral autoregulation for chronic stroke patients.

Using time domain analysis and the synchronization method, we are able to determine indices that can separate stroke patients from healthy subjects. These findings are clinically relevant and can be used to identify patients with impaired autoregulation who might be at risk of cerebral perfusion. They can be also used to distinguish patients with transient ischemic attacks who have reversible flow abnormalities from patients with permanent damage caused by the stroke.

Part VI

Appendix

.1 Detrened fluctuation analysis

In this section, we review the algorithm of the DFA method, and in Appendix .2 we compare the performance of the DFA with the classical scaling analysis —Hurst's analysis (R/S analysis)— and show that the DFA is a superior method to quantify the scaling behavior of noisy signals.

To illustrate the DFA method (Fig. 6), we consider a noisy time series, $u(i)$ ($i = 1, .., N_{max}$). We integrate the time series $u(i)$,

$$y(j) = \sum_{i=1}^{j} (u(i) - < u >), \tag{3}$$

where

$$< u >= \frac{1}{N_{max}} \sum_{j=1}^{N_{max}} u(i), \tag{4}$$

and is divided into boxes of equal size, n. In each box, we fit the integrated time series by using a polynomial function, $y_{fit}(i)$, which is called the local trend. For order-ℓ

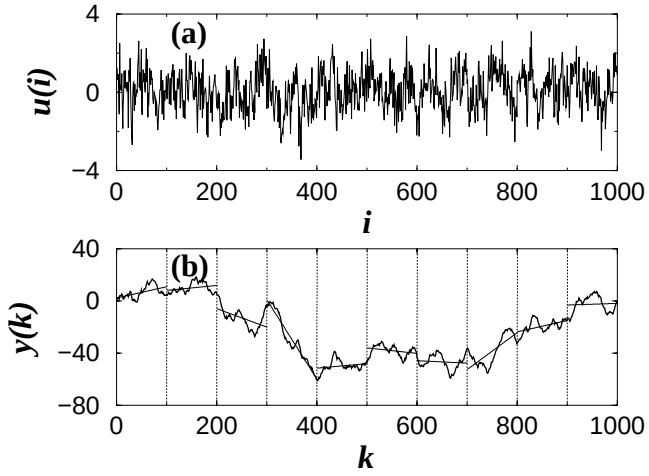

Fig. 6. Description of detrended fluctuation analysis (DFA) method. (a) The correlated signal $u(i)$. (b) The integrated signal: $y(k) = \sum_{i=1}^{k} [u(i) - \langle u \rangle]$. The vertical dotted lines indicate a box of size $n = 100$, the solid straight lines segments are the estimated linear "trend" in each box by least-squares fit.

DFA (DFA-1 if $\ell = 1$, DFA-2 if $\ell = 2$ etc.), ℓ order polynomial function should be applied for the fitting. We detrend The integrated time series, $y(i)$ by subtracting the local trend $y_{fit}(i)$ in each box, and we calculate the detrended fluctuation function

$$Y(i) = y(i) - y_{fit}(i). \tag{5}$$

For a given box size n, we calculate the root mean square (rms) fluctuation

$$F(n) = \sqrt{\frac{1}{N_{max}} \sum_{i=1}^{N_{max}} [Y(i)]^2} \tag{6}$$

The above computation is repeated for box sizes n (different scales) to provide a relationship between $F(n)$ and n. A power-law relation between $F(n)$ and the box size n indicates the presence of scaling: $F(n) \sim n^{\alpha}$. The parameter α, called the scaling exponent or correlation exponent, represents the correlation properties of the signal: if $\alpha = 0.5$, there is no correlation and the signal is an uncorrelated signal (white noise); if $\alpha < 0.5$, the signal is anticorrelated; if $\alpha > 0.5$, there are positive correlations in the signal.

.2 Noise

The standard signals we generate in our study are uncorrelated, correlated, and anticorrelated noise. First we must have a clear idea of the scaling behaviors of these standard signals before we use them to study the effects from other aspects. We generate noises by using a modified Fourier filtering method[67]. This method can efficiently generate noise, $u(i)$ $(i = 1, 2, 3, ..., N_{\max})$, with the desired power-law correlation function which asymptotically behaves as: $< |\sum_{j=i}^{i+t} u(j)|^2 > \sim t^{2\alpha}$. By default, a generated noise has standard deviation $\sigma = 1$. Then we can test DFA and R/S by applying it on generated noises since we know the expected scaling exponent α.

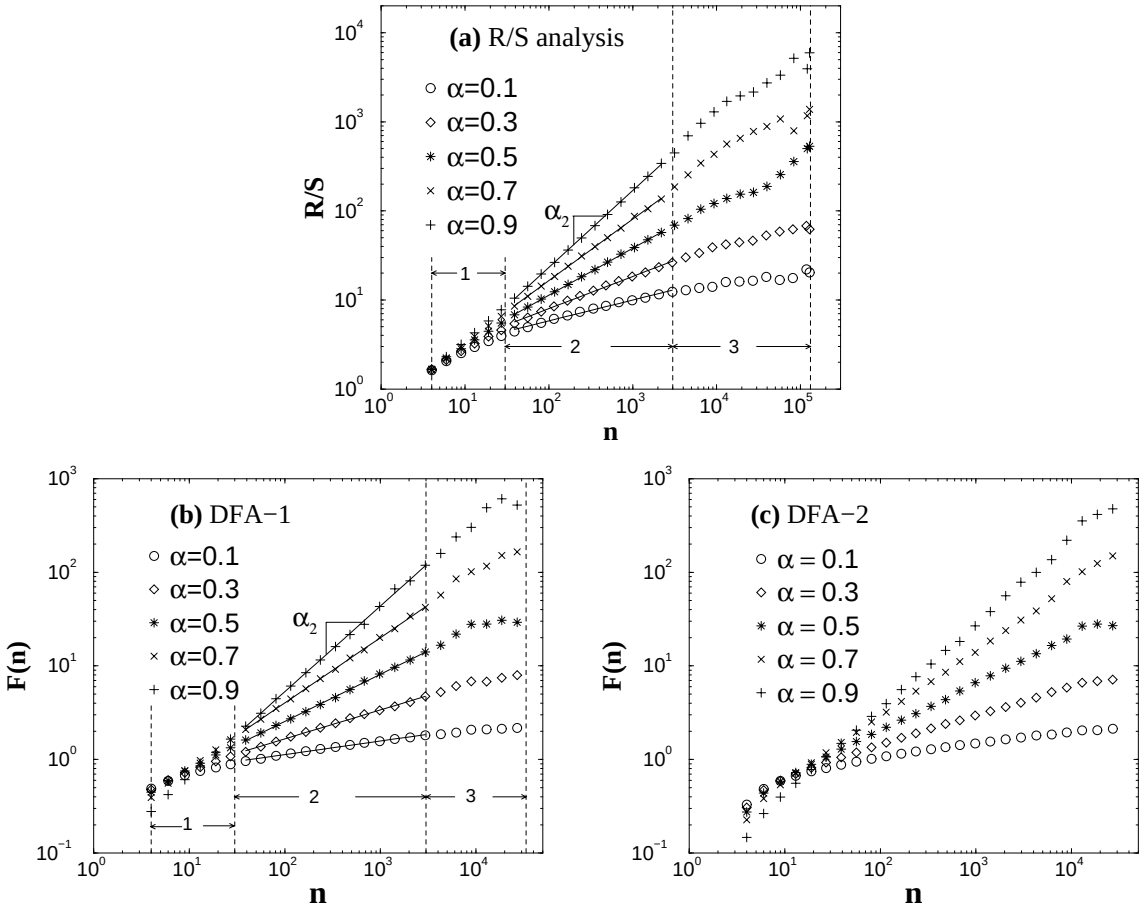

Fig. 7. Scaling behavior of noise with the scaling exponent α. The length of noise $N_{\max} = 2^{17}$. (a) Rescaled range analysis (R/S) (b) Order 1 detrended fluctuation analysis (DFA-1) (c) Order 2 detrended fluctuation analysis. We do the linear fitting for R/S analysis and DFA-1 in three regions as shown and get α_1, α_2 and α_3 for estimated α, which are listed in the Table.0.1 and Table.0.2. We find that the estimation of α is different in the different region.

Before doing that, we want to briefly review the algorithm of R/S analysis. For a signal $u(i)(i = 1, ..., N_{\max})$, it is divided into boxes of equal size n. In each box, the *cumulative departure*, X_i (for k-th box, $i = kn + 1, ..., kn + n$), is calculated

$$X_i = \sum_{j=kn+1}^{i} (u(j) - < u >) \tag{7}$$

where $< u >= n^{-1} \sum_{i=kn+1}^{(k+1)n} u(i)$, and the *rescaled range* R/S is defined by

$$R/S = S^{-1} \left[\max_{kn+1 \le i \le (k+1)n} X_i - \min_{kn+1 \le i \le (k+1)n} X_i \right], \tag{8}$$

where $S = \sqrt{n^{-1} \sum_{j=1}^{n} (u(j) - < u >)^2}$ is the standard deviation in each box. The average of rescaled range in all the boxes of equal size n, is obtained and denoted by $< R/S >$. Repeat the above computation over different box size n to provide a relationship between $< R/S >$ and n. According to Hurst's experimental study[68], a power-law relation between $< R/S >$ and the box size n indicates the presence of scaling: $< R/S > \sim n^{\alpha}$.

Figure 7 shows the results of R/S, DFA-1 and DFA-2 on the same generated noises. Loosely speaking, we can see that $F(n)$ (for DFA) and R/S (for R/S analysis) show power-law relation with n as expected: $F(n) \sim n^{\alpha}$ and $R/S \sim n^{\alpha}$. In addition, there is no significant difference between the results of different order DFA except for some vertical shift of the curves and the little bend-down for small box size n. The bent-down for very small box of $F(n)$ from higher order DFA is because there are more variables to fit those few points.

Ideally, when analyzing a standard noise, $F(n)$ (DFA) and R/S (R/S analysis) will be a power-law function with a given power: α, no matter which region of $F(n)$ and R/S is chosen for calculation. However, a careful study shows that the scaling exponent α depends on scale n. The estimated α is different for the different regions of $F(n)$ and R/S as illustrated by Figs. 7(a) and 7(b) and by Tables 0.1 and 0.2. It is very important to know the best fitting region of DFA and R/S analysis in the study of real signals. Otherwise, the wrong α will be obtained if an inappropriate region is selected.

In order to find the best region, we first determine the dependence of the locally estimated α, $\alpha_{\rm loc}$, on the scale n. First, generate a standard noise with given scaling exponent α; then calculate $F(n)$ (or R/S), and obtain $\alpha_{\rm loc}(n)$ by local fitting of

Table 0.1. Estimated α of correlation noise from R/S analysis in three regions as shown in Fig.7(a). α is the input value of the scaling exponent, α_1 is the estimated in the region 1 for $4 < n \leq 32$, α_2 in the region 2 for $32 < n \leq 3162$ and α_3 in the region 3 for $3126 < n \leq 2^{17}$. Noise are the same as used in Table.0.2.

α	α_1	α_2	α_3
0.1	0.44	0.23	0.12
0.3	0.52	0.37	0.23
0.5	0.62	0.52	0.47
0.7	0.72	0.70	0.45
0.9	0.81	0.87	0.63

Table 0.2. Estimated α of correlation noise from DFA-1 in three regions as shown in Fig.7(b). α is the input value of the scaling exponent, $\alpha 1$ is the estimated in the region 1 for $4 < n \leq 32$, $\alpha 2$ in the region 2 for $32 < n \leq 3162$ and $\alpha 3$ in the region 3 for $3126 < n \leq 2^{17}$.

α	α_1	α_2	α_3
0.1	0.28	0.15	0.08
0.3	0.40	0.31	0.22
0.5	0.55	0.50	0.35
0.7	0.72	0.69	0.55
0.9	0.91	0.91	0.69

$F(n)$ (or R/S). Same random simulation is repeated 50 times for both DFA and R/S analysis. The resultant average $\alpha_{\rm loc}(n)$, respectively, are illustrated in Fig.8 for DFA-1 and R/S analysis.

If a scaling analysis method is working properly, then the result $\alpha_{\rm loc}(n)$ from

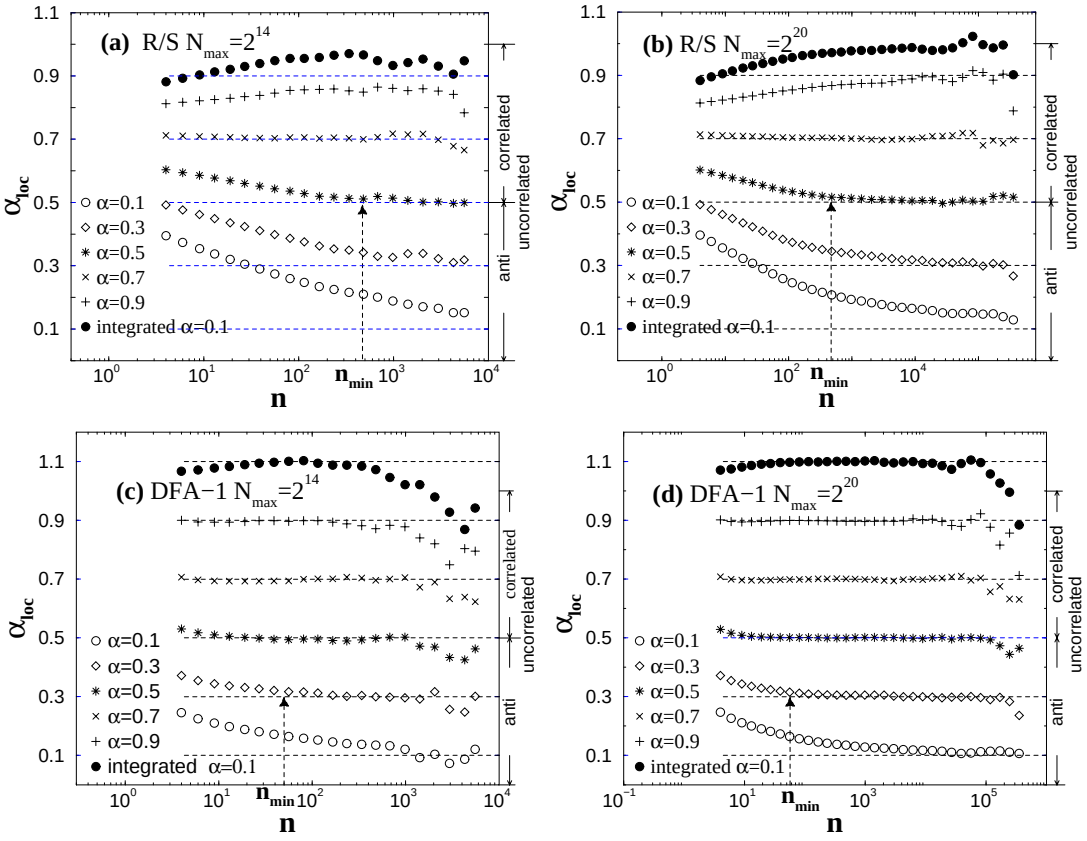

Fig. 8. The estimated α from local fit. (a) R/S analysis, the length of signal $N_{\max} = 2^{14}$. (b)R/S analysis, $N_{\max} = 2^{20}$. (c) DFA-1, $N_{\max} = 2^{14}$ (d) DFA-1, $N_{\max} = 2^{20}$. $\alpha_{\rm loc}$ come from the average of 50 simulations. If a technique is working, then the data for scaling exponent α should be a weakly fluctuating horizontal line centered about $\alpha_{\rm loc} = \alpha$. Note that such a horizontal behavior does not hold for all the scales. Generally, such a expected behavior begins from some scale $n_{\min}$, holds for a range and ends at a larger scale $n_{\max}$. For DFA-1, $n_{\min}$ is quite small $\alpha > 0.5$. For R/S analysis, $n_{\min}$ is small only when $\alpha \approx 0.7$.

simulation with α would be a horizontal line with slight fluctuation centered about $\alpha_{\rm loc}(n) = \alpha$. Note from Fig.8 that such a *horizontal behavior* does not hold for all the scales n but for a certain range from $n_{\min}$ to $n_{\max}$. In addition, at small scale, R/S analysis gives $\alpha_{\rm loc} > \alpha$ if $\alpha < 0.7$ and $\alpha_{\rm loc} < \alpha$ if $\alpha > 0.7$, which has been pointed out by Mandelbrot[69] while DFA gives $\alpha_{\rm loc} > \alpha$ if $\alpha < 1.0$ and $\alpha_{\rm loc} < \alpha$ if

$\alpha > 1.0$.

It is clear that the smaller the $n_{\min}$ and the larger the $n_{\max}$, the better the method. We also perceive that the expected *horizontal behavior* stops because the fluctuations become larger due to the under-sampling of $F(n)$ or R/S when n gets closer to the length of the signal $N_{\max}$. Furthermore, it can be seen from Fig.8 that $n_{\max} \approx \frac{1}{10} N_{\max}$ independent of α (if the best fit region exists), which is why one tenth of the signal length is the maximum box size when using DFA or R/S analysis.

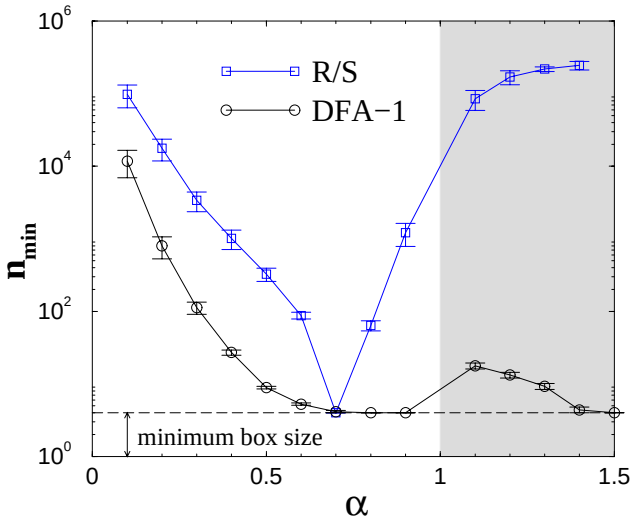

Fig. 9. The starting point of good fit region, $n_{\min}$, for DFA-1 and R/S analysis. The results are obtained from 50 simulations, in which the length of noise is $N_{\max} = 2^{20}$. The condition for a good fit is $\Delta\alpha = |\alpha_{\rm loc} - \alpha| < 0.01$. The data for $\alpha > 1.0$ shown in the shading area are obtained by applying analysis on the integrations of noises with $\alpha < 1.0$. It is clear that DFA-1 works better than R/S analysis because its $n_{\min}$ is always smaller than that of R/S analysis.

On the contrary, $n_{\min}$ does not depend on the $N_{\max}$ since $\alpha_{\rm loc}(n)$ at small n hardly changes as $N_{\max}$ varies but it does depend on α. Thus, we obtain $n_{\min}$ quantitatively as shown in Fig.9. For R/S analysis, only for $\alpha \approx 0.7$, $n_{\min}$ is small; for α a little away from 0.7 (for example, 0.5), $n_{\min}$ becomes very large and close to $n_{\max}$, indicating that the best fit region will vanish and R/S analysis does not work at all. Comparing

to R/S, DFA works better since $n_{\min}$ is quite small for $\alpha > 0.5$ correlated signals.

One problem remains for DFA, $n_{\min}$ for small α (≤ 0.5) is still too large comparing to those for large $\alpha(> 0.5)$. We can improve it by applying DFA on the integration of the noise with $\alpha < 0.5$. The resultant new expected $\alpha^{'}$ for the integrated signal would be $\alpha_0^{'} = \alpha + 1$, while the $n_{\min}$ for the integrated signal becomes much smaller as shown also in Fig.9(shading area $\alpha > 1$). Therefore, for a noise with $\alpha < 0.5$, it is best to estimate the scaling exponent $\alpha^{'}$ of the integrated signal first and then obtain α by $\alpha = \alpha^{'} - 1$. This is what we did in the following sections to those anticorrelated signals.

.3 Superposition law for DFA

For two uncorrelated signals $f(i)$ and $g(i)$, their root mean square fluctuation functions are $F_f(n)$ and $F_g(n)$ respectively. We want to prove that for the signal $f(i) + g(i)$, its rms fluctuation

$$F_{f+g}(n) = \sqrt{F_f(n)^2 + F_g(n)^2} \tag{9}$$

Consider three signals in the same box first. The integrated signals for f, g and $f + g$ are $y_f(i)$, $y_g(i)$ and $y_{f+g}(i)$ and their corresponding trends are y_f^{fit}, y_g^{fit},y_{f+g}^{fit} ($i = 1, 2, ..., n$, n is the box size). Since $y_{f+g}(i) = y_f(i) + y_g(i)$ and combine the definition of detrended fluctuation function Eq.5, we have that for all boxes

$$Y_{f+g}(i) = Y_f(i) + Y_g(i), \tag{10}$$

where Y_{f+g} is the detrended fluctuation function for the signal $f + g$, $Y_f(i)$ is for the signal f and $Y_g(i)$ for g. Furthermore, according to the definition of rms fluctuation, we can obtain

$$F_{f+g}(n) \quad = \sqrt{\frac{1}{N_{max}} \sum_{i=1}^{N_{max}} \left[Y_{f+g}(i)\right]^2} \tag{11}$$

$$= \sqrt{\frac{1}{N_{max}} \sum_{i=1}^{N_{max}} [Y_f(i) + Y_g(i)]^2},$$

where ℓ is the number of boxes and k means the kth box. If f and g are not correlated, neither are $Y_f(i)$ and $Y_g(i)$ and, thus,

$$\sum_{i=1}^{N_{max}} Y_f(i) Y_g(i) = 0. \tag{12}$$

From Eq.12 and Eq.12, we have

$$\begin{aligned} F_{f+g}(n) &= \sqrt{\frac{1}{N_{max}} \sum_{i=1}^{N_{max}} [Y_f(i)^2 + Y_g(i)^2]} \\ &= \sqrt{[F_f(n)]^2 + [F_g(n)]^2}. \end{aligned} \tag{13}$$

.4 DFA-1 on linear trend

Let us suppose a linear time series $u(i) = A_{\mathrm{L}} i$. The integrated signal $y_L(i)$ is

$$y_L(i) = \sum_{j=1}^{i} A_{\mathrm{L}} j = A_{\mathrm{L}} \frac{i^2 + i}{2} \tag{14}$$

Let as call N_{max} the size of the series and n the size of the box. The rms fluctuation $F_{\mathrm{L}}(n)$ as a function of n and N_{max} is

$$F_{\mathrm{L}}(n) = A_{\mathrm{L}} \sqrt{\frac{1}{N_{max}} \sum_{k=1}^{N_{max}/n} \sum_{i=(k-1)n+1}^{kn} \left(\frac{i^2 + i}{2} - (a_k + b_k i) \right)^2} \tag{15}$$

where a_k and b_k are the parameters of a least-squares fit of the k-th box of size n. a_k and b_k can be determined analytically, thus giving:

$$a_k = 1 - \frac{1}{12} n^2 + \frac{1}{2} n^2 k + \frac{1}{12} n - \frac{1}{2} k^2 n^2 \tag{16}$$

$$b_k = 1 - \frac{1}{2} n + kn + \frac{1}{2} \tag{17}$$

With these values, $F_{\rm L}(n)$ can be evaluated analytically:

$$F_{\rm L}(n) = A_{\rm L}\frac{1}{60}\sqrt{(5n^4 + 25n^3 + 25n^2 - 25n - 30)} \tag{18}$$

The dominating term inside the square root is $5n^4$ and then one obtains

$$F_{\rm L}(n) \approx \frac{\sqrt{5}}{60}A_{\rm L}n^2 \tag{19}$$

leading directly to an exponent of 2 in the DFA. An important consequence is that, as $F(n)$ does not depend on N_{max}, for linear trends with the same slope, the DFA must give exactly the same results for series of different sizes. This is not true for other trends, where the exponent is 2, but the factor multiplying n^2 can depend on N_{max}.

.5 DFA-1 on Quadratic trend

Let us suppose now a series of the type $u(i) = A_{\rm Q}i^2$. The integrated time series $y(i)$ is

$$y(i) = A_{\rm Q}\sum_{j=1}^{i} j^2 = A_{\rm Q}\frac{2i^3 + 3i^2 + i}{6} \tag{20}$$

As before, let us call N_{max} and n the sizes of the series and box, respectively. The rms fluctuation function $F_{\rm Q}(n)$ measuring the rms fluctuation is now defined as

$$F_{\rm Q}(n) = A_{\rm Q}\sqrt{\frac{1}{N_{max}}\sum_{k=1}^{N_{max}/n}\sum_{i=(k-1)n+1}^{kn}\left(\frac{2i^3 + 3i^2 + i}{6} - (a_k + b_k i)\right)^2} \tag{21}$$

where a_k and b_k are the parameters of a least-squares fit of the k-th box of size n. As before, a_k and b_k can be determined analytically, thus giving:

$$a_k = \frac{1}{15}n^3 + n^3k^2 - \frac{7}{15}n^3k + \frac{17}{30}n^2k - \frac{7}{60}n^2 + \frac{1}{20}n - \frac{2}{3}k^3n^3 - \frac{1}{2}n^2k^2 + \frac{1}{15}kn \tag{22}$$

$$b_k = \frac{3}{10}n^2 + n^2k^2 - n^2k + kn - \frac{2}{5}n + \frac{1}{10} \tag{23}$$

Once a_k and b_k are known, $F(n)$ can be evaluated, giving:

$$F_{\mathrm{Q}}(n) = A_{\mathrm{Q}}\frac{1}{1260}\sqrt{-21\left(n^4+5n^3+5n^2-5n-6\right)\left(32n^2-6n-81-210N_{max}-140N_{max}^2\right)} \tag{24}$$

As $N_{max} > n$, the dominant term inside the square root is given by $140N_{max}^2 \times 21n^4 = A_{\mathrm{Q}}2940n^4N_{max}^2$, and then one has approximately

$$F_{\mathrm{Q}}(n) \approx A_{\mathrm{Q}}\frac{1}{1260}\sqrt{2940n^4N_{max}^2} = A_{\mathrm{Q}}\frac{1}{90}\sqrt{15}N_{max}n^2 \tag{25}$$

leading directly to an exponent 2 in the DFA analysis. An interesting consequence derived from Eq. (25) is that, $F_{\mathrm{Q}}(n)$ depends on the length of signal N_{max}, and the DFA line ($\log F_{\mathrm{Q}}(n)$ vs $\log n$) for quadratic series $u(i) = A_{\mathrm{Q}}i^2$ of different N_{max} does not overlap (as is the case for linear trends).

.6 Protocol and Measurements

To date our B&W collaborators (Drs. Shea and Czeisler) have collected complete (i) forced desynchrony protocol data on 14 healthy subjects(19-32 years, mean 23 years) and 17 elderly subjects (56-78 years, mean 69 years), and (ii) constant routine data on 14 young subjects (19-44 years, mean 27 years) and 11 elderly subjects (65-76 years, mean 71 years). These data were collected under funded grants (R01 HL64815, HL62149 and AG0607212). Some subjects completed both protocols, such that there are a total of 31 individuals (see page 51). Based on our preliminary findings, and using the DFA exponent α as our primary variable that has the most intra-subject variability (S.D. = 0.10), we have calculated that to detect physiologically important difference between circadian phases or between groups (p value = 0.05: difference between heart failure and controls = 0.2), we need to study at least 10 subjects. Since we have between 11 and 17 subjects in each group and protocol, we are confident that the available data set is sufficiently large to answer our specific aims. The primary signals collected that we propose to include in our analysis are (1) EKG, (2) activity, and (3) blood pressure. Core body temperature (CBT) was collected continuously, and will be used to establish the circadian phase. Additionally, during each scheduled sleep period full polysomnography (PSG) was performed, which includes measurements of: (a) four-channel EEG, right and left EOG, submental EMG (used to establish sleep stage); (b) EKG. The PSG measurements will be used to establish sleep-wake and sleep stage effects (independent of the circadian rhythm) on cardiovascular variables.

.6.1 Establishing a Regular Sleep / Wake / Exercise Baseline Schedule

To ensure the initial stability of circadian rhythms and sleep patterns, subjects are required to maintain a regular sleep-wake schedule for 2 weeks prior to admission to

the laboratory. The bedtime are determined as the subjects' habitual bedtime with 8-h time in bed. To ensure compliance to this schedule, each subject is monitored with ambulatory actigraphy (Actiwatch AW-64, Minimitter Co. Inc., OR, US).

.6.2 Laboratory Environment for Forced Desynchrony and Constant Routine Protocols

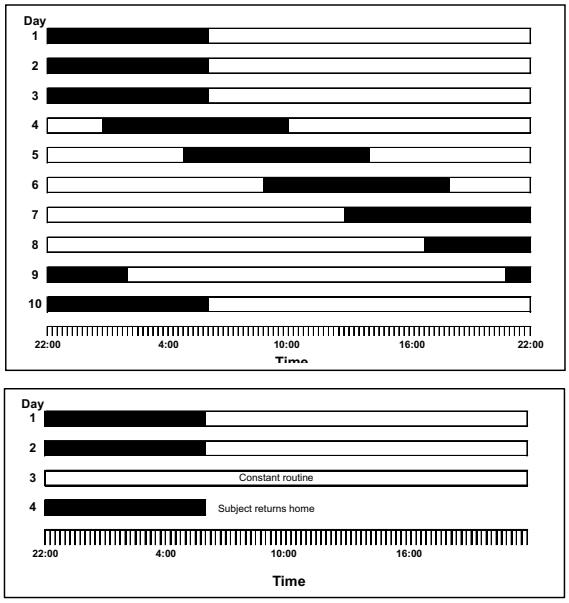

Fig. 10. Sleep/wake schedule

Subjects are isolated from external time cues, including clocks, radios, television, personal computers, visitors, and sunlight, but maintain contact with staff members . Room temperature is maintained at 23±1°C. The experimental suites are equipped with hand-held terminals for event recording, a porthole for 24 h blood sample collection without disturbing the subjects' sleep, and a video camera and a voice-activated microphone for subject monitoring. Technicians are present 24 h per day to monitor data acquisition, collect biologic specimens, perform tests, and record sleep episodes.

All staff are trained to avoid communicating either the time of day or the nature of the experimental conditions to the subjects. An extensive series of written protocols and checklists is used to ensure uniformity in the execution of standard procedures (e.g., at bedtime and waketime).

Baseline: During the baseline segments of recordings, subjects are on a 'normal routine' in which his/her bedtimes and wake-times are scheduled according to that of the screening period including eight hours of sleep per 24-hour period and they are restricted to light activity only. During the scheduled sleep times, the subjects are in darkness (< 0.2 lux) while during the scheduled wake episodes normal room lighting is used (150 lux). Three balanced meals are served during these normal routine days. The subject are asked not to take daytime naps.

Forced desynchrony: In this experiment we use a 28-h regime. A schematic representation of the disassociation of the sleep-wake schedule from the circadian rhythm is illustrated in Fig. 10 Top. The Forced Desynchrony protocol begins on the morning of Experimental Day 3 and continues for the next 7 days, ending on the evening of Experimental Day 9. Upon waking on Experimental Day 3, the subjects' sleep-wake cycle is scheduled to a period of 28 h. Bed rest / dark episodes are 9.33 h long and waking episodes are 18.67 h long. The subjects' daily activities are scheduled in this manner for six, 28-h 'days'. In this way the entire circadian cycle have occurred across all sleep-wake cycles, and vice versa. During this segment of the protocol, ambient light intensities during waking episodes are 3 lux (very dim room light) and < 0.02 lux during bed rest episodes. All testing procedures and blood sampling continues. Upon awakening from sleep on Experimental Day 10, subjects are discharged from the laboratory.

Constant routine: This begins upon awakening after baseline (Fig. 10 Bottom). The subjects spend 40 hours awake on a constant routine (missing one nights' sleep). S/he is asked to remain awake, sitting semi-recumbent on a bed (45° torso elevation), in dim (< 15 lux) indoor light. The subjects' diet during this segment consists of a

measured portion of food and drink every 2 hours containing approximately 100 mEq potassium and 150 mEq sodium per 24 hours, consisting of 25% fat, 25% protein and 50% carbohydrates. Fluid intake is constant at 3.5 L/day. Following the constant routine subjects are scheduled for an 8-hour recovery sleep opportunity. After this subjects are informed that the study is completed and that they may leave the laboratory.

.6.3 Data Collection, Storage and Transfer

EKG: A two channel (RA-V6, RA-V5) bipolar EKG was recorded continuously over the 12-day period at 512 Hz using the Vitaport recording system (TEMEC Instruments, Kerkrade, Netherlands). The raw EKG signals are downloaded in ASCII format and transferred via secure FTP to Physiobank (NIH/NCRR Grant No. P41RR13622) data storage system. The EKG is then automatically scored by Aristotle software (http://www.physionet.org/physiotools/ecgpuwave) where R-wave times and beat morphologies are annotated. Each individual R-wave time is assigned (1) a circadian phase (based on the CBT data), (2) time into study time, (3) a sleep-wake state and (4) a time into sleep or wakefulness. The data are available via a secure web or FTP link to the PI's group for analysis.

Temperature recording and analysis of circadian phase: Analysis of CBT rhythms from forced desynchrony protocols yields an accurate estimate of circadian phase [160]. A real-time, on-line data acquisition system is used to continuously record CBT every minute via a disposable rectal thermistor (Yellow Springs Instrument Company, Yellow Springs, OH). The thermistor is inserted 10cm into the rectum and remains there for the duration of the protocol. Using well-validated mathematical techniques the phase (ϕ), period (τ) and amplitude (ω) of the CBT rhythm can be established [160] (see also Appendix A). CBT is collected continuously across the entire 12-day protocol at a sampling frequency of 1-minute per sample.

This data is stored directly into an ASCII file residing on the Brigham and Women's Hospital, GCRC system.

Activity: Wrist activity levels are continuously measured in subjects for the 3-weeks before admission to the laboratory and for the entire 12-day protocol (Actiwatch-Light, Minimitter, OR, USA). Activity levels are quantified using digital integration of epochs of 30-second duration.

Blood pressure: Beat-to-beat blood pressure are measured using the Portapress (TPD Biomedical Instrumentation, Amsterdam, Netherlands). This is a reliable, non-invasive device which accurately measures blood pressure. Measurements are continuously recorded during sleep on each forced desynchrony sleep period and throughout the entire constant routine study. Arterial blood pressure are measured by means of a finger cuff (plethysmography) calibrated against an arm cuff. Blood pressure calibrations are then maintained for finger height with an in-built hydrostatic monometer. Recordings are stored directly to computer hard drive and are time synchronized with EKG and CBT measurements. Beat-to-beat blood pressure data are collected throughout each sleep episode and during four, 2-hour intervals each day.

Wake and sleep episodes: During scheduled wakefulness, subjects are free to move about the suite as desired, except that they are not permitted to lie down or nap. The subjects' activity is monitored by wrist worn actigraphy and behavioral activity is monitored. Sleep episodes are polysomnographically recorded. Subjects are instructed not to get out of bed, even if they should awaken before the end of the scheduled sleep episode. If requested, a technician will bring the subject a urinal or bedpan during scheduled sleep time. During scheduled sleep time, the ambient light intensity in the suite is less than 0.02 lux (complete darkness). Polysomnographic EEG recording is performed using surface electrodes (Beckman Instrument Company, Schiller Park, IL) applied to specific locations on the subjects' face and scalp prior to bedtime for the recording of central (C_3 and C_4) and occipital (O_1 and O_2)

electroencephalogram (EEG), electro-oculogram (EOG), and submental electromyogram (EMG). EKG was also recorded using a standard chest lead.

For the entire in-laboratory phase of the studies all EEG, EOG, EMG, and EKG channels are continuously monitored via at a sampling frequency of 512 Hz using a Vitaport system (TEMEC, Netherlands), and the data are stored onto an 200 Mbyte flash RAM card for downloading after wake time. All sleep recordings are scored visually in 30-second epochs according to the method of Rechtschaffen and Kales [161]. Sleep measures include latency to sleep onset, latency to REM sleep, wake after sleep onset (WASO), minutes and percentage of each stage of sleep [Stages I, II, III, IV, SWS (Stages III & IV combined) and REM], sleep efficiency, and amount of wake in the last 2-h of the sleep episode. Inter-beat interval is assessed from the EKG using standard validated software (http://www.physionet.org/physiotools/ecgpuwave).

All sleep recordings are scored visually in 30-second epochs according to the method of Rechtschaffen and Kales. Sleep measures include latency to sleep onset, latency to REM sleep, wake after sleep onset (WASO), minutes and percentage of each stage of sleep [Stages 1, 2, 3, 4,], sleep efficiency, and amount of wake in the sleep episode.

.7 Circadian Methods of Data Analysis

Each physiologic measurement is assigned a circadian phase (with minimum CBT equal to 0 circadian degrees, which translates to ≈5AM), and data are aligned to the CBT rhythm. Cosinor analysis [96, 162] is performed with the inclusion of a linear term (for estimation of the effect of duration of wakefulness), a fundamental cosine curve (at the period of the circadian clock 24.18-h) and a harmonic cosine term (period = 12.9-h). Any linear effects of sleep deprivation (homeostatic sleep drive) are removed by subtraction of the linear coefficients obtained from each the individual's cosinor analysis. Data are then normalized across subjects by expressing

variables as a percent deviation from the mean, minimizing inter-subject variability in absolute baseline levels. We then average across circadian "bins" of 60° within each subject. Group cosinor analysis (no linear term), was then performed on this normalized data. The results are double plotted for better visualization of underlying circadian rhythms.

Part VII

References

Bibliography

[1] Kantz H, Schreiber T. *Nonlinear Time Series Analysis*. Cambridge University Press, Cambridge, 1997.

[2] Bernaola-Galvan P, Grosse I, Carpena P, Oliver JL, Roman-Roldan R, Stanley HE, Finding borders between coding and noncoding DNA regions by an entropic segmentation method. *Phys Rev Lett* 2000;85:1342–1345.

[3] Viswanathan GM, Peng C-K, Stanley HE, Goldberger AL. Deviations from uniform power law scaling in nonstationary time series. *Phys Rev E* 1996;55:845–849.

[4] C.-K. Peng, S.V. Buldyrev, S. Havlin, M. Simons, H.E. Stanley, A.L. Goldberger, Phys. Rev. E **49**, 1685 (1994).

[5] S. V. Buldyrev, A. L. Goldberger, S. Havlin, C.-K. Peng, H.E. Stanley, and M. Simons, Biophys. J. **65**, 2673 (1993).

[6] S.M. Ossadnik, S.B. Buldyrev, A.L. Goldberger, S. Havlin, R.N. Mantegna, C.-K. Peng, M. Simons, and H.E. Stanley, Biophys. J. **67**, 64 (1994).

[7] M.S. Taqqu, V. Teverovsky, and W. Willinger, Fractals **3** 785 (1995).

[8] N. Iyengar, C.-K. Peng, R. Morin, A. L. Goldberger, and L.A. Lipsitz, A.M. J. Physiol-Reg. I **40**, R1078 (1996).

[9] P. Ch. Ivanov, M.G. Rosenblum, C.-K. Peng, J.E. Mietus, S. Havlin, H.E. Stanley, and A.L. Goldberger, Nature **383**, 323 (1996).

[10] K.K.L. Ho, G.B. Moody, C.-K. Peng, J.E. Mietus, M.G. Larson, D. Levy, A.L. Goldberger, Circulation **96** 842 (1997).

[11] P. Ch. Ivanov, M.G. Rosenblum, C.-K. Peng, J.E. Mietus, S. Havlin, H.E. Stanley, and A.L. Goldberger, Physica A **249**, 587 (1998).

[12] M. Barbi, S. Chillemi, A. Di Garbo, R. Balocchi, C. Carpeggiani, M. Emdin, C. Michelassi, E. Santarcangelo, Chaos Solitions & Fractals **9**, 507 (1998).

[13] Ivanov PCh, Bunde A, Amaral LAN, Havlin S, Fritsch-Yelle J, Baevsky RM, Stanley HE, Goldberger AL. Sleep-wake differences in scaling behavior of the human heartbeat: analysis of terrestrial and long-term space flight data. *Europhys Lett* 1999;48:594–600.

[14] S.M. Pikkujamsa, T.H. Makikallio, L.B. Sourander, I.J. Raiha, P. Puukka, J. Skytta, C.-K. Peng, A.L. Goldberger, H.V. Huikuri, Circulation **100**, 393 (1999).

[15] S. Havlin, S.V. Buldyrev, A. Bunde, A.L. Goldberger, P. Ch. Ivanov,C.-K. Peng, and H.E. Stanley, Physica A **273**, 46 (1999).

[16] H.E. Stanley, L. Amaral, A.L. Goldberger, S. Havlin, P.C. Ivanov, and C.-K. Peng, Physica A **270**, 309 (1999).

[17] Y. Ashkenazy, M. Lewkowicz, J. Levitan, S. Havlin, K. Saermark, H. Moelgaard, P.E.B. Thomsen, Fractals **7**, 85 (1999).

[18] T. H. Makikallio, J. Koistinen, L. Jordaens, M.P. Tulppo, N. Wood, B. Golosarsky, C.-K. Peng, A.L. Goldberger, H.V. Huikuri, Am. J. Cardiol. **83**, 880 (1999).

[19] Peng C-K, Havlin S, Stanley HE, Goldberger AL. Quantification of scaling exponents and crossover phenomena in nonstationary heartbeat time series. *Chaos* 1995;5:82–87.

[20] S. Havlin, S.V. Buldyrev, A.L. Goldberger, S.M. Ossadniksm, C.-K. Peng, M. Simons, and H.E. Stanley, Chaos Soliton Fract. **6**, 171 (1995).

[21] P.A. Absil, R. Sepulchre, A. Bilge, and P. Gerard, Physica A **272**, 235 (1999).

[22] S. Havlin, L.A. Nunes Amaral, A.L. Goldberger, P.Ch. Ivanov, C.-K. Peng, and H.E. Stanley, Physica A **274**, 99 (1999).

[23] D. Toweill, K. Sonnenthal, B. Kimberly, S. Lai, and B. Goldstein, Crit. Care Med. **28**, 2051 (2000).

[24] A. Bunde, S. Havlin, J.W. Kantelhardt, T. Penzel, J.H. Peter, and K. Voigt, Phys. Rev. Lett. **85**, 3736 (2000).

[25] T.T. Laitio, H.V. Huikuri, E.S.H. Kentala, T.H. Makikallio, J.R. Jalonen, H. Helenius, K. Sariola-Heinonen, S. Yli-Mayry, and H. Scheinin, Anesthesiology **93**, 69 (2000).

[26] Ashkenazy Y, Ivanov PCh, Havlin S, Peng C-K, Goldberger AL, Stanley HE. Magnitude and sign correlations in heartbeat fluctuations. *Phys Rev Lett* 2001;86(9):1900–1903.

[27] C.-K. Peng, S.V. Buldyrev, A.L. Goldberger, S. Havlin, M. Simons, and H.E. Stanley, Phys. Rev. E **47**, 3730 (1993).

[28] H.E. Stanley, S.V. Buldyrev, A.L. Goldberger, S. Havlin, R.N. Mantegna, C.-K. Peng, and M. Simons, Nuovo Cimento D **16**, 1339 (1994).

[29] R.N. Mantegna, S. V. Buldyrev, A.L. Goldberger, S. Havlin, C.-K. Peng, M. Simons, and H.E. Stanley, Phys. Rev. Lett. **73**, 3169 (1994).

[30] C.-K. Peng, S.V. Buldyrev, A.L. Goldberger, S. Havlin, R.N. Mantegna, M. Simons, and H.E. Stanley, Physica A **221**, 180 (1995).

[31] S. Havlin, S.V. Buldyrev, A.L. Goldberger, R.N. Mantegna, C.-K. Peng, M. Simons, and H.E. Stanley, Fractals **3**, 269 (1995).

[32] R.N. Mantegna, S. V. Buldyrev, A.L. Goldberger, S. Havlin, C.-K. Peng, M. Simons, and H.E. Stanley, Phys. Rev. Lett. **76**, 1979 (1996).

[33] S.V. Buldyrev, N.V. Dokholyan, A.L. Goldberger, S. Havlin, C.-K. Peng, H.E. Stanley, and G.M. Viswanathan, Physica A **249**, 430 (1998).

[34] S. Blesic, S. Milosevic, D. Stratimirovic, and M. Ljubisavljevic, Physica A **268**, 275 (1999).

[35] H. Yoshinaga, S. Miyazima, and S. Mitake, Physica A **280**, 582 (2000).

[36] C.A. Perazzo, E.A. Fernandez, D.R. Chialvo, and P.l. Willshaw, Fractal **8**, 279 (2000).

[37] Z. Siwy, S. Mercik, K. Ivanova and M. Ausloos, Physica A (in press).

[38] Y. Liu, P. Cizeau, M. Meyer, C.-K. Peng, and H.E. Stanley, Physica A **245**, 437 (1997).

[39] N. Vandewalle and M. Ausloos, Physica A **246**, 454 (1997).

[40] N. Vandewalle and M. Ausloos, Phy. Rev. E **58**, 6832 (1998).

[41] Y. Liu, P. Gopikrishnan, P. Cizeau, M. Meyer, C.-K. Peng, and H.E. Stanley, Phys. Rev. E **60**, 1390 (1999).

[42] I.M. Janosi, B. Janecsko, and I. Kondor, Physica A **269**, 111 (1999).

[43] M. Ausloos, N. Vandewalle, P. Boveroux, A. Minguet, and K. Ivanova, Physica A **274**, 229 (1999).

[44] M. Roberto, E. Scalas, G. Cuniberti, M. Riani, Physica A **269**, 148 (1999).

[45] N. Vandewalle, M. Ausloos, and P. Boveroux, Physica A **269**, 170 (1999).

[46] P. Grau-Carles, Physica A **287**, 396 (2000).

[47] M. Ausloos, Physica A **285**, 48 (2000).

[48] M. Ausloos and K. Ivanova, Physica A **286**, 353 (2000).

[49] M. Ausloos and K. Ivanova, Phys. Rev. E **63**, 047201 (2001).

[50] M. Ausloos and K. Ivanova, Int J Mod Phys C (to be published) (2001).

[51] K. Ivanova and M. Ausloos, Physica A **274**, 349 (1999).

[52] A. Montanari, R. Rosso, and M. S. Taqqu, Water Resour. Res. **36**, (5) 1249 (2000).

[53] C. Matsoukas, S. Islam, and I. Rodriguez-Iturbe, J. Geophys. Res-Atmos. **105**, 29165 (2000).

[54] J. W. Kantelhardt, R. Berkovits, S. Havlin, and A. Bunde, Physica A **266**, 461 (1999) B.D. Malamud and D.L. Turcotte, J. Stat. Plan. Infer. **80**, 173 (1999).

[55] C.L. Alados, M.A. Huffman, Ethology **106**, 105 (2000).

[56] Peng C-K, Mietus J, Hausdorff JM, Havlin S, Stanley HE, Goldberger AL. Long-range anti-correlations and non-Gaussian behavior of the heartbeat. *Phys Rev Lett* 1993;70:1343–1346.

[57] N. Makarenko, L.M. Karimova, B.I. Demchenko and M.M. Novak, Fractals **6**, 359 (1998).

[58] G. M. Viswanathan, S. V. Buldyrev, E. K. Garger, V. A. Kashpur, L. S. Lucena, A. Shlyakhter, H.E. Stanley, and J. Tschiersch, Phys. Rev. E **62**, 4389 (2000).

[59] E. Koscielny-Bunde, A. Bunde, S. Havlin, H. E. Roman, Y. Goldreich, H. J. Schellnhuber, Phys. Rev. E **81**, 729 (1998).

[60] E. Koscielny-Bunde, H. E. Roman, A. Bunde, S. Havlin, and H. J. Schellnhuber, Philo. Mag. B **77**, 1331 (1998).

[61] K. Ivanova, M. Ausloos, E. E. Clothiaux, and T. P. Ackerman, Europhys. Lett. **52**, 40 (2000).

[62] P. Talkner and R. O. Weber, Phys. Rev. E **62**, 150 (2000).

[63] Y. Ogata, K. Abe, Int. Stat. Rev. **59**, 139 (1991).

[64] Bernaola-Galvan P, Ivanov PCh, Amaral LAN, Stanley HE. Scale invariance in the nonstationarity of physiological signals. *Phys Rev Lett* 2001;87(16):168105(4).

[65] M.F. Shlesinger and G.H. Weiss, *The Wonderful world of stochastics : a tribute to Elliott W. Montroll*, (North-Holland, New York, 1985).

[66] D. Stauffer and H. E. Stanley, *From Newton to Mandelbrot*, Second edition, (Springer-Verlag, Berlin, 1996).

[67] H.A. Makse, S. Havlin, M. Schwartz, and H.E. Stanley, Phys. Rev. E **53**, 5445-5449 Part B (1996).

[68] H.E. Hurst, Trans. Am. Soc. Civ. Eng. **116**, 770 (1951).

[69] B.B. Mandelbrot and James R. Wallis, Water Resources Research **5 No.2**, (1969).

[70] J.W. Kantelhardt, E. Koscielny-Bunde, H.H.A. Rego, S. Havlin, and A. Bunde, Physica A **294**, 441 (2001).

[71] K. Hu, P.Ch. Ivanov, Z. Chen, P. Carpena and H.E. Stanley, Phys. Rev. E **64**, 011114 (2001).

[72] Z. Chen, P. Ch. Ivanov, K. Hu, H. E. Stanley, Phys. Rev. E 65 041107 (2002).

[73] R.L. Stratonovich, *Topics in the Theory of Random Noise Vol. 1* (Gordon & Breach, New York, 1981).

[74] A. Witt, J. Kurths, and A. Pikovsky, Phys. Rev. E **58**, 1800 (1998).

[75] C.-K. Peng, S.V. Buldyrev, A.L. Goldberger, S. Havlin, F. Sciortino, M. Simons, and H.E. Stanley, Nature (London) **356**, 168 (1992).

[76] H.E. Stanley, S.V. Buldyrev, A.L. Goldberger, S. Havlin, C.-K. Peng and M. Simons, Physica A **273**, 1 (1999).

[77] S. Bahar, J.W. Kantelhardt, A. Neiman, H.H.A. Rego, D.F. Russell, L. Wilkens, A. Bunde, and F. Moss, Europhys. Lett. **56**, 454 (2001).

[78] P.Ch. Ivanov, L.A. Nunes Amaral, A.L. Goldberger, and H.E. Stanley, Europhys. Lett. **43**, 363 (1998).

[79] J.W. Kantelhardt, E. Koscielny-Bunde, H.H.A. Rego, S. Havlin, and A. Bunde, Physica A **294**, 441 (2001).

[80] M.A. Carskadon and W.C. Dement, *Principle and Practice of Sleep Medicine* (WB Saunders Co., Philadelphia, 2000).

[81] P.Ch. Ivanov, L.A. Nunes Amaral, A.L. Goldberger, S. Havlin, M.G. Rosenblum, Z.R. Struzik, and H.E. Stanley, Nature (London) **399**, 461 (1999).

[82] Ashkenazy Y, Ivanov PCh, Havlin S, Peng C-K, Yamamoto Y, Goldberger AL, Stanley HE. Decomposition of heartbeat time series: scaling analysis of the sign sequence. *Computers in Cardiology* 2000;27:139–142.

[83] P.Ch. Ivanov, L.A. Nunes Amaral, A.L. Goldberger, M.G. Rosenblum, H.E. Stanley, and Z.R. Struzik, Chaos **11**, 641 (2001).

[84] J.M. Hausdorff, C.-K. Peng, Z. Ladin, J. Wei and A.L. Goldberger, J. Applied Physiol. **78**, 349 (1995).

[85] K. Hu, Plamen Ch. Ivanov, Z. Chen, M. F. Hilton, H. E. Stanley, S. A. Shea, "Novel multiscale regulation in human motor activity", *SPIE Proceedings* **5110**, 235-243 (2003).

[86] K. Hu, Plamen Ch. Ivanov, Z. Chen, M. F. Hilton, H. E. Stanley and S. A. Shea, "Non-Random Fluctuations and Multi-scale Dynamics Regulation of Human Activity", *Physica A* (2004).

[87] Dijk DJ, Czeisler CA. Paradoxical timing of the circadian rhythm of sleep propensity serves to consolidate sleep and wakefulness in humans. *Neurosci Lett* 1994;166:63–68.

[88] Czeisler CA, Duffy JF, Shanahan TL, Brown EN, Mitchell JF, Rimmer DW, Ronda JM, Silva EJ, Allan JS, Emens JS, Dijk DJ, Kronauer RE. Stability, precision, and near-24-hour period of the human circadian pacemaker. *Science* 1999;284:2177–2181.

[89] N. Kleitman, Sleep 5 (1982) 311.

[90] P. Lavie, Chronobiol. Int. 6 (1989) 21.

[91] S. M. Patterson, D. S. Krantz, L. C. Montgomery, P. A. Deuster, S. M. Hedges, L. E. Nebel, Psychophysiology 30 (1993) 296.

[92] N. Aoyagi, K. Ohashi, S. Tomono, Y. Yamamoto, Am. J. Physiol. Heart Circ. Physiol. 278 (2000) H1035.

[93] A. C. Leary, P. T. Donnan, T. M. MacDonald, M. B. Murphy, American Journal of Hypertension 13 (2000) 1067.

[94] G. Jean-Louis, M. V. Mendlowicz, J. C. Gillin, M. H. Rapaport, J. R. Kelsoe, F. Zizi, H. P. Landolt, H. Von Gizycki, Physiology & Behavior 70 (2000) 49.

[95] C. A. Czeisler, R. E. Kronauer, J. S. Allan, J. F. Duffy, M. E. Jewett, E. N. Brown, J. M. Ronda, Science 244 (1989) 1328.

[96] Brown EN, Czeisler CA. The statistical analysis of circadian phase and amplitude in constant- routine core-temperature data. *J Biol Rhythms* 1992;7:177–202.

[97] B. D. Lewis, D. F. Kripke, D. M. Bowden, Physiology & Behavior 18 (1977) 283.

[98] G. Nagels, P. Marion, B. A. Pickut, L. Timmermans, P. P. DeDeyn, Electromyography and Motor control-electroencephalography and Clinical Neurophysiology 101, (1996) 226.

[99] J. M. Winters, G. Loeb, Biomechanics and Neural Control of Posture and Movement, edited by J. M. Winters, P. E. Crago, Springer Verlag, New York, 2000.

[100] J. M. Haudsdorff, C. K. Peng, Z. Ladin, J. Y. Wei, A. L. Goldberger, J. Appl. Physiol. 78 (1995) 349.

[101] Y. Q. Chen, , M. Z. Ding, J. A. S. Kelso, Phys. Rev. Lett. 79 (1997) 4501.

[102] Muller JE, Stone PH, Turi ZG, Rutherford JD, Czeisler CA, Parker C, Poole WK, Passamani E, Roberts R, Robertson T, Sobel BE, Willerson JT, Braunwald E, and the MILIS Study Group. Circadian variation in the frequency of onset of acute myocardial infarction. *N Eng J Med* 1985;313:1315-1322.

[103] Anderson RN. Deaths:Leading causes for 2000. National vital statistics reports 50[16]. 2002. Hyattsville, Maryland, National Center for Health Statistics.

[104] GoldberG RJ, Brady P, Muller JE, Chen ZY, Degroot M, Zonneveld P, Dalen JE. Time of onset of symptoms of acute myocardial infarction. *Am J Cardiol* 1990;66:140–144.

[105] Ridker PM, Manson JE, Buring JE, Muller JE, Hennekens CH. Circadian variation of acute myocardial infarction and the effect of low-dose aspirin in a randomized trial of physicians. *Circulation* 1990;82:897-902.

[106] Tofler GH, Stone PH, Maclure M, Edelman E, Davis VG, Robertson T, Antman EM, Muller JE. Analysis of possible triggers of acute myocardial infarction (the MILIS study). *Am J Cardiol* 1990;66:22–27.

[107] Tofler GH, Muller JE, Stone PH, Forman S, Solomon RE, Knatterud GL, Braunwald E. Modifiers of timing and possible triggers of acute myocardial infarction in the Thrombolysis in Myocardial Infarction Phase II (TIMI II) Study Group. *J Am Coll Cardiol* 1992;20:1049–1055.

[108] Cannon CP, McCabe CH, Stone PH, Schactman M, Thompson B, Theroux P, Gibson RS, Feldman T, Kleiman NS, Tofler GH, Muller JE, Chaitman BR, Braunwald E. Circadian variation in the onset of unstable angina and non-Q-wave acute myocardial infarction (the TIMI III Registry and TIMI IIIB). *Am J Cardiol* 1997;79:253–258.

[109] Marler JR, Price TR, Clark GL, Muller JE, Robertson T, Mohr JP, Hier DB, Wolf PA, Caplan LR, Foulkes MA. Morning Increase in onset of ischemic stroke. *Stroke* 1989;20:473–476.

[110] Willich SN, Pohjola-Sintonen S, Bhatia SJS, Shook TL, Tofler GH, Muller JE, Curtis DG, Williams GH, Stone PH. Suppression of silent ischemia by metoprolol without alteration of morning increase of platelet aggregability in patients with stable coronary artery disease. *Circulation* 1989;79:557–565.

[111] Tofler GH, Gebara OC, Mittleman MA, Taylor P, Siegel W, Venditti FJ, Rasmussen CA, Muller JE. Morning peak in ventricular tachyarrhythmias detected by time of implantable cardioverter/defibrillator therapy. The CPI Investigators. *Circulation* 1995;92:1203–1208.

[112] Willich SN, Levy D, Rocco MB, Tofler GH, Stone PH, Muller JE. Circadian variation in the incidence of sudden cardiac death in the Framingham Heart Study population. *Am J Cardiol* 1987;60:801–806.

[113] Willich SN, Goldberg RJ, Maclure M, Perriello L, Muller JE. Increased onset of sudden cardiac death in the first three hours after awakening. *Am J Cardiol* 1992;70:65–68.

[114] Willich SN, Maclure M, Mittleman M, Arntz HR, Muller JE. Sudden cardiac death. Support for a role of triggering in causation. *Circulation* 1993;87:1442–1450.

[115] Muller JE, Ludmer PL, Wilich SN, Tofler GH, Aylmer G, Klangos I, Stone PH. Circadian variation in the frequency of sudden cardiac death. *Circulation* 1987;75:131-138.

[116] Willich SN, Linderer T, Wegscheider K, Leizorovicz A, Alamercery I, Schroder R. Increased morning incidence of myocardial infarction in the ISAM Study:

absence with prior beta-adrenergic blockade. ISAM Study Group. *Circulation* 1989;80:853–858.

[117] Lavery CE, Mittleman MA, Cohen MC, Muller JE, Verrier RL. Nonuniform nighttime distribution of acute cardiac events: a possible effect of sleep states. *Circulation* 1997;96:3321–3327.

[118] Brezinski DA, Tofler GH, Muller JE, Pohjolasintonen S, Willich SN, Schafer AI, Czeisler CA, Williams GH. Morning increase in platelet aggregability. Association with assumption of the upright posture. *Circulation* 1988;78:35–40.

[119] Winther K, Hillegass W, Tofler GH, Jimenez A, Brezinski DA, Schafer AI, Loscalzo J, Williams GH, Muller JE. Effects on platelet aggregation and fibrinolytic activity during upright posture and exercise in healthy men. *Am J Cardiol* 1992;70:1051–1055.

[120] Parker JD, Testa MA, Jimenez AH, Tofler GH, Muller JE, Parker JO, Stone PH. Morning increase in ambulatory ischemia in patients with stable coronary artery disease. Importance of physical activity and increased cardiac demand. *Circulation.*1994;89:604–614.

[121] Jimenez AH, Tofler GH, Chen XG, Stubbs ME, Solomon HS, Muller JE. Effects of nadolol on hemodynamic and hemostatic responses to potential mental and physical triggers of myocardial infarction in subjects with mild systemic hypertension. *Am J Cardiol* 1993;72:47–52.

[122] Muller JE, Tofler GH. Morning vs afternoon exertion. Both are safe, but which is safer? *Arch Intern Med* 1993;153:803–804.

[123] Mittleman MA, Maclure M, Tofler GH, Sherwood JB, Goldberg RJ, Muller JE. Triggering of acute myocardial infarction by heavy physical exertion. Pro-

tection against triggering by regular exertion. Determinants of Myocardial Infarction Onset Study Investigators. *N Engl J Med* 1993;329:1677–1683.

[124] Boulant JA, Dean JB. Temperature receptors in the central nervous system. *Annu Rev Physiol* 1986;48:639-654.

[125] Jones BE. Basic mechanisms of sleep-wake states. In: Kryger MH, Roth T, Dement WC, eds. Principles and practice of slep medicine. Philadelphia: W.B. Saunders, 2001;134–154.

[126] Sherin JE, Shiromani PJ, McCarley RW, Saper CB. Activation of ventrolateral preoptic neurons during sleep. *Science* 1996;271:216–219.

[127] Lin L, Faraco J, Li R, Kadotani H, Rogers W, Lin X, Qiu X, de J, Nishino S, Mignot E. The sleep disorder canine narcolepsy is caused by a mutation in the hypocretin (orexin) receptor 2 gene. *Cell* 1999;98:365–376.

[128] Sherin JE, Elmquist JK, Torrealba F, Saper CB. Innervation of histaminergic tuberomammillary neurons by GABAergic and galaninergic neurons in the ventrolateral preoptic nucleus of the rat. *J Neurosci* 1998;18:4705–4721.

[129] Lydic R, Moore-Ede MC. Three dimensional structure of the suprachiasmatic nuclei in the diurnal squirrel monkey (Saimiri sciureus). *Neurosci Lett* 1980;17:295–299.

[130] Ralph MR, Foster RG, Davis FC, Menaker M. Transplanted suprachiasmatic nucleus determines circadian period. *Science* 1990;247:975–978.

[131] Dijk DJ, Czeisler CA. Contribution of the circadian pacemaker and the sleep homeostat to sleep propensity, sleep structure, electroencephalographic slow waves, and sleep spindle activity in humans. J *Neurosci* 1995;15:3526–3538.

[132] Dijk DJ, Duffy JF, Czeisler CA. Circadian and sleep/wake dependent aspects of subjective alertness and cognitive performance. *J Sleep Res* 1992;1:112–117.

[133] Dijk DJ, Shanahan TL, Duffy JF, Ronda JM, Czeisler CA. Variation of electroencephalographic activity during non-rapid eye movement and rapid eye movement sleep with phase of circadian melatonin rhythm in humans. *J Physiol (Lond)* 1997;505:851–858.

[134] Dijk DJ, Duffy JF, Riel E, Shanahan TL, Czeisler CA. Ageing and the circadian and homeostatic regulation of human sleep during forced desynchrony of rest, melatonin and temperature rhythms. *J Physiol (Lond)* 1999;516:611–627.

[135] Johnson MP, Duffy JF, Dijk DJ, Ronda JM, Dyal CM, Czeisler CA. Short-term memory, alertness and performance: a reappraisal of their relationship to body temperature. *J Sleep Res* 1992;1:24–29.

[136] Klein T, Martens H, Dijk DJ, Kronauer RE, Seely EW, Czeisler CA. Circadian sleep regulation in the absence of light perception: chronic non-24-hour circadian rhythm sleep disorder in a blind man with a regular 24-hour sleep-wake schedule. *Sleep* 1993;16:333–343.

[137] Burgess HJ, Trindler J, Kim Y, Luke D. Sleep and circadian influences on cardiac autonomic nervous system activity. *Am J Physiol* 1997;273:H1761–H1768.

[138] Hilton MF, Umali MU, Czeisler CA, Wyatt JK, Shea SA. Endogenous circadian control of the human autonomic nervous system. *Comp in Cardiol* 2001;27:197–200.

[139] Hilton MF, Umali MU, Kres SP. Circadian variation of vagal and pulmonary function indices: a potential mechanism for nocturnal asthma. *Am J Respir Crit Care Med* 2000;161:A679(Abstract).

[140] Umali MU, Hilton MF, Kres SP, Czeisler CA, Wyatt JK, Shea SA. Circadian and sleep stage influences on cardiac autonomic tone. *Sleep* 2000;23:A26(Abstract).

[141] Hilton MF, Sugarbaker RJ, Sheils SA, Trinder J, Okruch AJ, Shea SA. Circadian control of the autonomic arousal response. *Actas de Fisiologia* 2001;7:133(Abstract).

[142] Buijs RM, La Fleur SE, Wortel J, Van Heyningen C, Zuiddam L, Mettenleiter TC, Kalsbeek A, Nagai K, Niijima A. The Suprachiasmatic nucleus balances sympathetic and parasympathetic output to peripheral organs through separate preautonomic neurons. *J COMP NEUROL* 2003;464:36–48.

[143] Cajochen C, Khalsa SBS, Wyatt JK, Czeisler CA, Dijk DJ. EEG and ocular correlates of circadian melatonin phase and human performance decrements during sleep loss. *Am J Physiol-reg* 1999;277:R640–R649.

[144] Duffy JF, Dijk DJ, Hall EF, Czeisler CA. Relationship of endogenous circadian melatonin and temperature rhythms to self-reported preference for morning or evening activity in young and older people. *J Investig Med* 1999;47:141–150.

[145] Jewett ME, Wyatt JK, Ritz-De Cecco A, Khalsa SB, Dijk DJ, Czeisler CA. Time course of sleep inertia dissipation in human performance and alertness. *J Sleep Res* 1999;8:1–8.

[146] Boivin DB, Czeisler CA, Dijk DJ, Duffy JF, Folkard S, Minors DS, Totterdell P, Waterhouse JM. Complex interaction of the sleep-wake cycle and circadian phase modulates mood in healthy subjects. *Arch Gen Psychiat* 1997;54:145–152.

[147] Czeisler CA, Weitzman Ed, Moore-Ede MC. Human sleep: its duration and organization depend on its circadian phase. *Science* 1980;210:1264–1267.

[148] Spengler CM, Czeisler CA, Shea SA. An endogenous circadian rhythm of respiratory control in humans. *J Physiol* 2000;526:683–694.

[149] Shea SA, Baldwin MR, Harvey EL. Circadian aspects of cardio-respiratory control in humans. *Physiologist* 1999;42:A-16(Abstract).

[150] Bernard, C. *Les Phénoménes de la Vie* (Paris, 1878).

[151] van der Pol B, van der Mark J. The heartbeat considered as a relaxation oscillation, and an electrical model of the heart. *Phil Mag* 1928;6:763–775.

[152] Cannon, WB. Organization for physiological homeostasis. *Physiol. Rev.* 1929;9:399–431.

[153] Hyndman, BW. The role of rhythms in homeostasis. *Kybernetik* 1974;15:227–236.

[154] Kobayashi M, Musha T. $1/f$ fluctuation of heartbeat period. *IEEE Trans Biomed Eng* 1982;29:456–457.

[155] Peng C-K, Buldyrev SV, Hausforff JH, Havlin S, Mietus JE, Simons M, Stanley HE, Goldberger AL. Nonequilibrium dynamics as an indispensable characteristic of a healthy biological system. *Integr Physiol Behavioral Sci* 1994;29:283–298.

[156] Bassingthwaighte JB, Liebovitch LS, West BJ. *Fractal Physiology*. Oxford University Press, New York, 1994.

[157] Malik M, Camm AJ, eds. *Heart Rate Variability*. Futura, Armonk NY, 1995.

[158] Muller JE. Circadian variation in cardiovascular events. *Am J Hypertens* 1999;12:35S–42S.

[159] Aronson D. Impaired modulation of circadian rhythms in patients with diabetes mellitus: a risk factor for cardiac thrombotic events? *Chronobiol Int* 2001;18:109–121.

[160] Khalsa SBS, Jewett ME, Duffy JF, Czeisler CA. The timing of the human circadian clock is accurately represented by the core body temperature rhythm following phase shifts to a three-cycle light stimulus near the critical zone. *J Biol Rhythm* 2000;15:524–530.

[161] Rechtschaffen A, Kales A. In: Rechtschaffen A, Kales A, editors. A manual of standardised terminology, techniques and scoring system for sleep stages of human subjects. Los Angeles: Brain Information service/Brain Research Institute, 1968.

[162] Nelson W, Tong YL, Lee JK. Methods for cosinor-rhythmometr y. *Chronobiologia* 1979;6:305–323.

[163] Ashkenazy Y, Ivanov PCh, Havlin S, Peng C-K, Goldberger AL, Stanley HE. Magnitude and sign correlations in heartbeat fluctuations. *Phys Rev Lett* 2001;86(9):1900–1903.

[164] Ashkenazy Y, Havlin S, Ivanov PCh, Peng C-K, Schulte-Frohlinde V, Stanley HE. Magnitude and sign scaling in power-law correlated time series. *Physica A* 2003;323:19–41.

[165] Sugihara G, Allan W, Sobel D, Allan KD. Nonlinear control of heart rate variability in human infants. *Proc Natl Acad Sci USA* 1996;93:2608–2613.

[166] Z. Chen, P. Ch. Ivanov, K. Hu, H. E. Stanley and V. Novak, "Synchronization patterns in cerebral blood flow and peripheral blood pressure under minor stroke", *SPIE Proceedings*, **5114**, 498-506 (2003).

[167] R. L. Sacco, B. Boden-Albala, R. Gan, X. Chen, D. E. Kargman, S. Shea, M. C. Paik, and W. A. Hauser, "Stroke incidence among white, black, and hispanic residents of an urban community: the northern manhattan stroke study," *Am. J. Epidemiol.* **147**, 259–268, 1998.

[168] S. Schwarz, D. Georgiadis, A. Aschoff, and S. Schwab, "Effects of body position on intracranial pressure and cerebral perfusion in patients with large hemispheric stroke," *Stroke* **33**, 497–501, 2002.

[169] P. J. Eames, M. J. Blake, S. L. Dawson, R. B. Panerai, and J. F. Potter, "Dynamic cerebral autoregulation and beat to beat blood pressure control are impaired in acute ischaemic stroke," *J. Neurol Neurosur. Ps.* **72**, 467–473, 2002.

[170] L. A. Lipsitz, S. Mukai, J. Hammer, M. Gagnon, and V. L. Babikian, "Dynamic regulation of middle cerebral artery blood flow velocity in aging and hypertension," *Stroke* **31**, 1897–1903, 2000.

[171] L. Cupini, M. Diomedi, F. Placidi, M. Silvestrini, and P. Giacomini, "Cerebrovascular reactivity and subcortical infarctions," *Arch. Neurol* **58**, 577–581, 2001.

[172] V. Novak, J. M. Spies, P. Novak, B. R. McPhee, and T. A. Rummans, "Hypocapnia and cerebral hypoperfusion in orthostatic intolerance," *Stroke* **29**, 1876–1881, 1998.

[173] J. M. Serrador, P. A. Picot, B. K. Rutt, J. K. Shoemaker, and R. L. Bondar, "Mri measures of middle cerebral artery diameter on conscious humans during simulated orthostasis," *Stroke* **31(7)**, 1672–1678, 2000.

[174] V. Novak, P. Novak, and R. Schondorf, "Accuracy of beat-to-beat noninvasive measurement of finger arterial pressure using the finapres: a spectral analysis approach," *J. Clin. Monitor. Comp.* **10**, 118–126, 1994.

[175] J. F. Claerbout, *Fundamentals of Geophysical Data Processing*, McGraw-Hill, New York, 1976.

[176] M. G. Rosenblum, A. S. Pikovsky, and J. Kurths, "Phase synchronization of chaotic oscillators," *Phys. Rev. Lett.* **76(11)**, 1804–1807, 1996.

[177] M. G. Rosenblum, A. S. Pikovsky, and J. Kurths, "From phase to lag synchronization in coupled chaotic oscillators," *Phys. Rev. Lett.* **78(22)**, 4193–4196, 1997.

[178] A. V. Oppenheim and R. W. Schafer, *Discrete-Time Signal Processing, 2nd ed.*, Prentice-Hall, Upper Saddle River, New Jersey, 1998.

[179] S. L. Marple, "Computing the discrete-time analytic signal via FFT," *IEEE T. Signal Proces.* **47(9)**, 2600–2603, 1999.

Part VIII

Curriculum Vitae

Curriculum Vitæ
Kun Hu

Boston University, Physics Department
Center For Polymer Studies
590 Commonwealth Avenue
Boston, Massachusetts 02215 USA

Telephone: 617/353-8936
Facsimile: 617/353-9393 or 617/353-3783
E-mail: khu@argento.bu.edu
WWW: http://polymer.bu.edu/~khu

EDUCATION

- Ph.D., 2004 - Physics; Boston University, Boston, MA
- M.A., 1999 - Physics; University of Rhode Island, Kingston, RI
- B.S. honors, 1995 - Physics; Zhongshan University, China

EMPLOYMENT

- Research Assistant, Physics Department, Boston University. Spring 2001 - present.
- Teaching Assistant, Physics Department, Boston University. Fall 1999 - Spring 2001.
- Teaching Assistant, Physics Department, University of Rhode Island. Fall 1997 - Spring 1999

HONORS, AWARDS

- 2003 American Physical Society travel awards for Annual Meeting.
- 1995: "Excellent Graduate", Zhongshan University, 1995

REFERENCES

- H. Eugene Stanley: University Professor of Physics, Professor of Physiology, Director of Center for Polymer Studies; Department of Physics, Boston University, 590 Commonwealth Avenue, Boston, MA 02215. **Tel:** (617) 353 2617, **FAX:** (617) 353 3783,

  Email: hes@bu.edu.

- Steven A. Shea: Associate Professor of Medicine; Division of Sleep Medicine, Brigham & Women's Hospital, Harvard Medical School, 330 Brookline Avenue, Boston, MA 02115. **Tel:** (617) 732 5013, **FAX:** (617) 278 0683,

  Email: sshea@hms.harvard.edu

- Plamen Ch. Ivanov:

PUBLICATIONS

I. CONDENSED MATTER PHYSICS:

[1] X. Sun, X. H. Xu, K. Hu and K. Yonemitsu, "Effect of electron correlation on competition between BOW and SDW in polymer", *Phys. Lett. A* **239(3)**, 191-195 (1998).

[2] X. H. Xu, R. T. Fu, K. Hu, X. Sun and K. Yonemitsu, "Off-diagonal interactions and spin-density waves in polymers", *Phys. Rev. B* **58(14)**, 9039-9046 (1998).

[3] M. Karbach, K. Hu, G. Muller and J. Tobochnik, "Computer simulations — Introduction to the Bethe ansatz II", *Computers in Phys.* **12 (6)**, 565-573 (1998).

II. PHYSIOLOGIC FLUCTUATIONS:

[4] K. Hu, Plamen Ch. Ivanov, Z. Chen, Pedro Carpena and H. Eugene Stanley, "Effect of trends on detrended fluctuation analysis", *Phys. Rev. E* **64**, 011114 (2001).

[5] Z. Chen, Plamen Ch. Ivanov, K. Hu, H. Eugene Stanley, "Effect of nonstationarities on detrended fluctuation analysis", *Phys. Rev. E* **65**, 041107 (2002).

[6] K. Hu, Plamen Ch. Ivanov, Z. Chen, M. F. Hilton, H. E. Stanley, S. A. Shea, "Novel multiscale regulation in human motor activity", *SPIE Proceedings* **5110**, 235-243 (2003).

[7] Z. Chen, P. Ch. Ivanov, K. Hu, H. E. Stanley and V. Novak, "Synchronization patterns in cerebral blood flow and peripheral blood pressure under minor stroke", *SPIE Proceedings*, **5114**, 498-506 (2003).

[8] K. Hu, Plamen Ch. Ivanov, Z. Chen, M. F. Hilton, H. E. Stanley and S. A. Shea, "Non-Random Fluctuations and Multi-scale Dynamics Regulation of Human Activity", *Physica A* (2004).